University of Alberta

DAM-BREAK FLOWS AS AGENTS OF SEDIMENT TRANSPORT

by

Matthew Emmett

A thesis submitted to the Faculty of Graduate Studies and Research
in partial fulfillment of the requirements for the degree of

Doctor of Philosophy

in

Applied Mathematics

Department of Mathematical and Statistical Sciences

© Matthew Emmett
Fall, 2010
Edmonton, Alberta

Examining Committee

Dr. T.B. Moodie, Mathematical and Statistical Sciences

Dr. G. Swaters, Mathematical and Statistical Sciences

Dr. B. Sutherland, Physics

Dr. A. Bush, Earth and Atmospheric Sciences

Dr. M. R. Flynn, Mechanical Engineering

Dr. J. Bush, Mathematics, Massachusetts Institute of Technology

Abstract

When a semi-infinite body of homogeneous fluid initially at rest behind a vertical retaining wall is suddenly released by the removal of the barrier the resulting flow over a horizontal or sloping bed is referred to as a dam-break flow. When resistance to the flow is neglected the exact solution, in the case of a stable horizontal bed with or without 'tail water', may be obtained on the basis of shallow-water theory via the method of characteristics and the results are well known. Discrepancies between these shallow-water based solutions and experiments have been partially accounted for by the introduction of flow resistance in the form of basal friction. This added friction significantly modifies the wave speed and flow profile near the head of the wave so that the simple exact solutions no longer apply and various asymptotic or numerical approaches must be implemented to solve these frictionally modified depth-averaged shallow-water equations. When the bed is no longer stable so that solid particles may be exchanged between the bed and the water column the dynamics of the flow becomes highly complex as the buoyancy forces vary in space and time according to the competing rates of erosion and deposition. Furthermore, when the Froude number of the flow is close to unity perturbations in the height and velocity profiles grow into N-waves and the bed below develops ripples which act to sustain the N-waves in the fluid above. It is our intention here to study dam-break flows over erodible sloping beds as agents of sediment transport taking into account basal friction as well as the effects of particle concentrations on flow dynamics including both erosion and deposition. We shall consider shallow flows over initially dry beds and investigate the effects of changes in the depositional and erosional models employed as well as in the nature of the drag acting on the flow and the slope of the bed. These models include effects hitherto neglected in such studies and offer insights into the transport of sediment in the worst case scenario of the complete and instantaneous collapse of a dam.

Preface

The work presented throughout this thesis has been published, or submitted for publication, in:

1. M. Emmett and T.B. Moodie, *Dam-break flows with resistance as agents of sediment transport*, Physics of Fluids vol. 20 no. 8 pp. 086603, 2008.

2. M. Emmett and T.B. Moodie, *Sediment transport via dam-break flows over sloping erodible beds*, Studies in Applied Mathematics vol. 123 no. 3 pp. 257–290, 2009.

3. M. Emmett and T.B. Moodie, *Sediment transport via dam-break flows over sloping erodible beds*, proceedings of the Multiphase Fluid Flow 2009 conference, Wessex Institute of Technology, New Forest, UK.

4. M. Emmett and T.B. Moodie, *Non-uniform WENO methods for dam-break flows with drag: locating the wet/dry interface directly*, submitted to the Journal of Computational Physics, March 2010.

5. M. Emmett and T.B. Moodie, *Formation of bed ripples in critical Froude number dam-break flows*, submitted to the Journal of Fluid Mechanics, July 2010.

Acknowledgements

Table of Contents

List of Figures

List of Symbols

Fluid model

Numerical method

Chapter 1

Introduction

Dam-break flows, which are represented by the sudden release of fluid contained in a semi-infinite reservoir behind a vertical barrier, are of both practical and fundamental importance in fluid mechanics, engineering, and geomorphology. They have played a crucial role in underpinning simple models for a number of natural and catastrophic events such as break-out floods from the failure of end moraine dams, glacial lake outburst floods, various sheet flow events as well as the formative stages of lahars or debris flows [10, 21, 42, 48]. Although in practice the release of water upon collapse of the retaining barrier will often be more gradual than that in the idealised mathematical models one can view these models as providing the worst case scenario for these events[53, 48].

Sediment transport plays in important role in various geological phenomena. For example, the propagation and resulting deposition patterns of turbidity currents, which are gravity currents driven by density gradients caused by the presence of sediment suspended in the flow by turbulence, are of particular interest to geologists and engineers. Turbidity surges in ancient seas have contributed to the formation some petroleum reservoirs, and modern turbidity currents may interfere with offshore structures designed to exploit these petroleum resources [13]. Relatively simple box models of suspension-driven turbidity surges suggest that the overall thickness of proximal deposits resulting from particle driven gravity surges should exhibit a maximum at a predictable distance downstream from the source. As a result, suspension driven turbidity currents running out on flat plains should result in lenticular deposition patterns with coarse-grain deposition layers exhibiting maximal thickness upstream relative to fine-grain deposition layers. These geometries have been observed in ancient, near-reef basins and abyssal plains [13].

The significance of the impact of sediment transport via dam-break flows is exemplified in the recent study of Clarke *et al* [11] which considers the flood that emerged from Lake Agassiz several thousand years ago due to the collapse of a glacial dam. It has been postulated that the flood waters from Lake Agassiz were voluminous enough to cap the Atlantic Ocean thereby disrupting the North Atlantic meridional overturning current (MOC) and triggering a significant climatic cold event 8200 calendar years BP. However, whether or not the flood waters were buoyant relative to the salt-water of the Atlantic Ocean so as to cap it would depend on their sediment load. That is, if the flood waters were sufficiently sediment-laden upon their arrival at the ocean, they would hug the bottom of the ocean leaving the MOC intact [11].

The earliest work on dam-break flows considered single phase, low aspect ratio, frictionless flows in rectangular geometry taking the shallow-water equations as the governing model equations. With the bed below the dam assumed horizontal and dry, the solution for the flow is a centred simple wave that was first developed by Ritter [45]. If the initial depth of water behind the dam is h_0, the front of the flow advances as a wave over the dry bed with constant speed $2\sqrt{gh_0}$, while the reduction of depth spreads back from the initial position of the dam with speed $\sqrt{gh_0}$, where g is the acceleration due to gravity. In the disturbed region between the two extremes of depth, the velocity u and the depth of the flow h are given by

$$u = \frac{2}{3}\left(\frac{x}{t} + \sqrt{gh_0}\right) \quad \text{and} \quad \sqrt{gh} = \frac{1}{3}\left(2\sqrt{gh_0} - \frac{x}{t}\right), \tag{1.1}$$

where x measures distance downstream of the original position of the dam and t the time elapsed since its collapse. The depth of the flow increases from zero at the front, whose position is given by $x = 2\sqrt{gh_0}\,t$, to the value h_0 at $x = -\sqrt{gh_0}\,t$. Over the same range, u falls in a linear fashion from $2\sqrt{gh_0}$ to zero in the undisturbed portion of the reservoir. Although these solutions do provide a reasonably good match to the experimental observations when the transients associated with the initial release have died down there are still important properties of the flow that are not captured by the classical shallow-water model used in the construction of the solutions displayed in (1.1). It has been observed in particular [15, 48] that for the dam-break flow experiments the water near the tip piles up and the front speed is appreciably less than that predicted by the simple theory.

In order to account for this blunting of the tip and the slowing down of the front several authors [16, 53, 54, 26] have postulated that near the tip, where the depth of flow drops to zero, frictional resistance and the resulting turbulence dominate the flow. To account for this basal friction a Chézy resistance term is added to

the momentum equation [53, 54]. Various asymptotic procedures were employed [16, 53, 26] to determine the influence of this resistance and it was found that its inclusion brought theory and experiment into closer accord. Since we are interested in developing and exploiting models for sediment transport that employ dam-break flows on down-sloping topography as paradigms for certain geological and engineering processes we shall extend the model beyond what is discussed in this paragraph while appreciating the significant gains achieved through the addition of the resistance term. In fact, basal friction with realistic parameterisations for geological applications appears to have a much greater influence on flow dynamics than does the presence of particles in suspension.

Two classes of sudden release flows have been considered as agents of sediment transport. These are fixed-volume releases and dam-break flows. Although we shall here concentrate on dam-break flows, with their infinite source of fluid, several of the assumptions from the earlier work on fixed-volume releases will be adopted and so we will give a brief overview of the fixed-volume work as it relates to the current study.

Fixed-volume releases of well-mixed particulate suspensions in the purely depositional regime and their subsequent depositional patterns have been studied both theoretically and experimentally employing lock-release flows by a multitude of authors [7, 6, 8, 39, 23, 38, 14]. For the theoretical work in [7, 6, 8, 39, 37] it was assumed that the particles are vertically well-mixed by the turbulence in the current, are advected by the mean flow without diffusion, and settle out through the viscous sub-layer at the bottom of the current with the Stokes settling velocity for an isolated particle in a fluid at rest with no re-entrainment of particles into the fluid column. It was further assumed that the pressure distribution was hydrostatic for these shallow inertial flows, that the horizontal velocity field was vertically uniform, and that the only resistance to the flow was due to the lighter ambient fluid which had to be displaced by the heavier particle-driven bottom hugging flow. The experimentally determined particle deposition patterns provided in [7, 6, 8, 14] would seem to confirm that these assumptions provide a very good first approximation to the output of a highly complex dynamical system. In particular, the more recent and accurate measurements of de Rooij and Dalziel [14] seem to confirm the theoretical predictions of [7, 8] for the distal depositional patterns. The discrepancies between the model predictions of [7, 8] and the measurements of [14] in the proximal depositional pattern would appear to be due to the fact that the model does not take into account the initial turbulence of mixing present in the release volume behind the dam rather than the assumptions inherent in the

model itself. When this initial turbulence is taken into account [38] the typical lenticular deposits seen in the experimentally determined depositional patterns [23] are reproduced under the well-mixed and hydrostatic assumptions. More recent high-resolution numerical simulations for particle-driven flows have been carried out by Necker *et al.* [40], and Blanchette *et al.* [5]. In Necker *et al.*[40], lock exchange flows involving dilute suspensions of small particles having negligible inertia are considered. By neglecting inertia the particle's velocity is then the sum of the local fluid velocity and the settling speed. This assumption requires that the aerodynamic response time for the particles is significantly lower than the characteristic time scale of the flow. A Boussinesq approximation for dilute suspensions was invoked [7, 6, 8, 39, 38, 37] and no re-entrainment of particles into the water column was included. Comparisons with the experimental results of de Rooij and Dalziel [14] were included and reasonable agreement was achieved. In Blanchette *et al.* [5], lock release models were again investigated for dilute suspension flows under a Boussinesq approximation neglecting particle-particle interactions, particle inertia and taking the particle velocity to be the sum of the local fluid velocity and the particle settling velocity. Both erosion and deposition were included in their model. The erosion or deposition depth was assumed small allowing them to keep the position of the bottom boundary fixed in the computations. Calculations of particle deposition patterns were compared with the experimental results of de Rooij and Dalziel [14] and reasonable agreement achieved.

Recent studies [10, 21, 42] have employed dam-break flows as agents of sediment transport. In [10, 21] flow over an erodible bed consisting of loose coarse sediment was investigated. The constitutive assumptions adopted in [10, 21] lead to the *en masse* mobilisation of the bed particles as bed-load by the flow to form a steep debris snout that leaves behind a uniform scour pit. On the other hand, the complimentary paper [42] deals with dam-break flow over a bed that consists of fine sediment that can be entrained into the water column and transported in suspension. In [42] the sediment transport was passive in that the suspended particles did not influence the flow dynamics which could then be completely specified by employing the simple exact solution of the shallow-water equations for both a dry bed [45] and a bed with 'tail water' [45, 49]. Hydraulic resistance and morphological evolution were excluded from their model and a Lagrangian formulation was used [44] for depth-averaged flow quantities.

In the present work we shall employ dam-break flows over sloping beds as agents of sediment transport. The inclusion of a velocity dependent basal friction as well as bottom topography and non-passive particle transport adds several important

mechanisms that were absent from the analysis in [42]. It is felt that the inclusion of these will shed light on those various phenomena that involve erosion and deposition of particles under flood conditions in the natural environment when topography is involved. We shall assume that our flows are shallow so that the pressure remains hydrostatic throughout the flow regime [42, 26, 7, 6, 8, 39, 19, 36] and also that the particle concentration in the flow remains sufficiently low that we may treat the particles as being isolated and employ a Boussinesq approximation whereby the particles appear in the momentum equations only in the buoyancy terms. This puts definite constraints on the range of particle volume fractions $\phi(x,t)$ in our well-mixed suspensions. It is known [2] that when the mean volume fraction of particles in suspension is ≈ 0.01 the mean free distance between grains is about four particle diameters and the probability of collisions is small. On the other hand, at a value of $\phi \approx 0.09$, the mean free distance is approximately equal to the grain diameter, and the probability of collisions becomes a certainty. When erosion exceeds deposition so that particle concentrations are increasing we shall assume that our model calculations are valid up until $\phi \approx 0.05$. Although the bottom boundary shear stress could be calculated from the full governing equations we shall adopt the common and much simpler approach of introducing a Chézy drag coefficient C_D which when viscous effects are small (large Reynolds number flows) gives the boundary shear stress as $\tau_b = C_D \rho_f u^2$, where ρ_f is the density of the fluid and u a depth averaged horizontal velocity [53, 26]. The Chézy drag coefficient is dimensionless and usually falls in the range 0.01-0.001 for most environmental flows [26]. With all of our additions to the model of Pritchard and Hogg [42] (basal drag, bottom topography, and particle modified flow dynamics) the simple shallow-water based solutions [45] will no longer apply and the approach adopted in [42] is not available so that an alternative approach will have to be adopted.

The model is developed in full detail in Chapter 2 where we shall also elaborate upon the validity of the assumptions that underlie its formulation. In Chapter 3 we will explore various asymptotic results to explore various limiting cases of the model. Chapter 4 is devoted to exploring the implications of our modeling assumptions. Chapter 5 details the numerical method used throughout the current study to solve the model equations. Finally, in Chapter 6 we will summarise and discuss the main results of this study and make some concluding remarks.

Chapter 2

Model development

We consider the two-dimensional flow resulting from the sudden release of water initially held at rest behind a plane vertical retaining wall of height h_0. The bed below the dam which is initially located at $x = 0$, is gently sloping and specified by the topography $z = b(x, t)$. It is assumed that there is no water below the dam and that the bed is comprised of fine or cohesive material which, once a threshold shear stress is exceeded, is entrained into the water column and transported in suspension to possibly be deposited downstream. Although in the early stages of such dam-break flows the aspect ratio, being the ratio of a typical vertical to horizontal scale of the flow, will not be small, there soon comes a post-release time when the assumption of a small aspect ratio has validity. The validity of this assumption, as a first approximation, is evident when one compares the theoretical results based on the solution of the shallow-water equations with the earlier experimental work of Dressler [16] and the more recent experiments of Stansby, Chegini, and Barnes [48]. There certainly are discrepancies between theory and experiment, especially in the early post-initiation stages of the flow, when the vertical and streamwise scales of the motion are of comparable order and non-hydraulic influences can be seen. However, there soon comes a time when transients arising from the initial release have died out and the streamwise scales dominate the vertical ones so that the flow may be considered a shallow flow with negligible vertical accelerations and a hydrostatic pressure distribution may be adopted [48, 45, 26, 54, 49]. Another discrepancy between the experimental observations and the Ritter solution of the shallow-water equations [45] can be seen in the frontal region of the flow field where the experimental front [48, 16] becomes blunted and the extent of the flow diminished from that derived on the basis of shallow-water theory. To account for these discrepancies several authors have introduced the notion of a basal drag
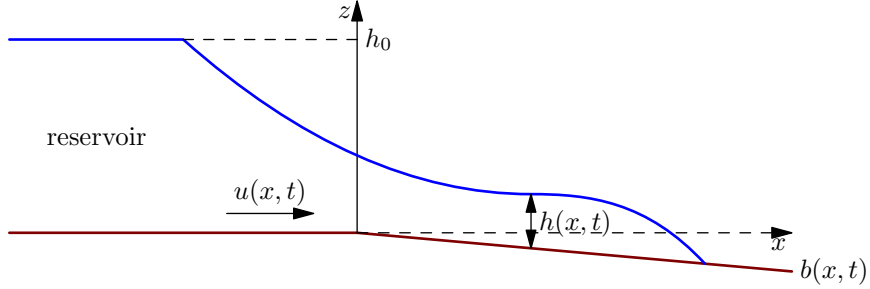
Figure 2.1: Schematic for the dam-break flow on a sloping dry erodible bed.

term into the horizontal momentum equation [53, 15, 26] and achieved a high degree of success in reconciling theory with experiment [26]. Our model will be based upon the assumption of a hydrostatic pressure distribution since vertical accelerations may be considered negligible for shallow flows. We will also include basal friction to account for the blunting and retarding of the flow front as seen in the experiments. The effect of suspended particles will enter the flow dynamics through the buoyancy terms and both erosion and deposition of these particles will be accounted for in the model so that these buoyancy effects will vary in both space and time. Figure 2.1 summarises the scenario described above.

Based upon the previous successful reconciliations between the theoretically determined depositional patterns obtained employing the vertically well-mixed assumption for lock release flows and the experimentally measured patterns [7, 6, 8] we shall adopt this assumption here. This same assumption which gives rise to a volume fraction ϕ of particles in suspension as a function of the streamwise coordinate x and time t only, has also been employed with success for other flow scenarios including dam-break flows [42, 26, 44]. The bulk density ρ of the suspension is then given by

$$\rho(\phi) = \rho_p\phi + (1 - \phi)\rho_f, \tag{2.1}$$

where ρ_p is the particle density. We shall also assume that the particles have the same velocity as the fluid so that the continuity equation for the flow is

$$\frac{\partial}{\partial t}\rho + \frac{\partial}{\partial x}(\rho u) + \frac{\partial}{\partial z}(\rho w) = \psi \tag{2.2}$$

where ψ describes the generation and removal of mass through the mechanisms of bed erosion and sediment deposition and w is the vertical velocity of the fluid. Since mass is entrained into, or deposited out of the fluid at the bed we set

$$\psi(x, z, t) = (q_e - q_d)\delta(z - b) \tag{2.3}$$

where q_e and q_d are the mass fluxes due to erosion and deposition respectively and δ is the Dirac delta function (the erosion and deposition fluxes q_e and q_d will be described in greater detail in Section 2.2).

Under the assumption that the particles have the same velocity as the fluid, the horizontal momentum equation for the flow is

$$\frac{\partial}{\partial t}(\rho u) + \frac{\partial}{\partial x}(\rho u u) + \frac{\partial}{\partial z}(\rho u w) = -\frac{\partial}{\partial x}p + \frac{\partial}{\partial z}\tau_{xz} \qquad (2.4)$$

where p is the pressure and τ_{xz} is the relevant stress component [30]. Again, we assume that the pressure field p is hydrostatic since the flow regimes that we are interested in are shallow. That is, at any point in the flow the pressure is given by

$$p = p_0 + \rho g(h + b - z) \qquad (2.5)$$

where p_0 is the pressure of the atmosphere and g is the acceleration due to gravity. The kinematic and dynamic boundary conditions for the system are

$$\left.\begin{array}{c} p = p_0 \\ w = \dfrac{\partial}{\partial t}(b + h) + u\dfrac{\partial}{\partial x}(b + h) \\ \tau_{xz} = 0 \end{array}\right\} \quad \text{at } z = b + h, \text{ and} \qquad (2.6)$$

$$\left.\begin{array}{c} \tau_{xz} = \tau_b \\ w = \dfrac{\partial}{\partial t}b + u\dfrac{\partial}{\partial x}b \end{array}\right\} \quad \text{at } z = b.$$

Finally, we shall assume that although the bed is erodible it is otherwise immobile. That is, the continuity equation for the bed material lacks any spatial flux and is therefore given by

$$\frac{\partial}{\partial t}(\rho_p b) = -\psi \quad (= q_d - q_e). \qquad (2.7)$$

2.1 Depth averaging

In order to obtain a set of equations that are relatively simple in structure we will average the model equations (2.2) and (2.4) over the depth of the flow. To do so, each equation is integrated over the depth of the fluid (ie, from b to $b + h$), the Leibniz result for differentiating integrals with variable limits is employed, and the various boundary conditions in (2.6) are applied.

8

In order to see how the various boundary conditions in (2.6) enter into the model, we will depth average the generic transport equation

$$\frac{\partial}{\partial t}\varphi + \nabla \cdot (\varphi \boldsymbol{u}) = \psi \qquad (2.8)$$

where $\boldsymbol{u} = (u, w)$ is the fluid velocity and ψ represents the sources and sinks of the quantity φ, which models the transport of a scalar quantity φ (ie, the bulk density ρ or horizontal momentum ρu). Integrating the transport equation (2.8) over depth gives

$$\int_b^{b+h} \frac{\partial}{\partial t}\varphi \, dz + \int_b^{b+h} \frac{\partial}{\partial x}(\varphi u) \, dz + \int_b^{b+h} \frac{\partial}{\partial z}(\varphi w) \, dz = \int_b^{b+h} \psi \, dz.$$

Simplifying each term on the left, we obtain

$$\int_b^{b+h} \frac{\partial}{\partial t}\varphi \, dz = \frac{\partial}{\partial t}\int_b^{b+h} \varphi \, dz - \varphi(z=b+h)\frac{\partial}{\partial t}(b+h) + \varphi(z=b)\frac{\partial}{\partial t}b$$

$$= \frac{\partial}{\partial t}(h\overline{\varphi}) - \varphi(z=b+h)\frac{\partial}{\partial t}(b+h) + \varphi(z=b)\frac{\partial}{\partial t}b,$$

$$\int_b^{b+h} \frac{\partial}{\partial x}(\varphi u) \, dz = \frac{\partial}{\partial x}\int_b^{b+h} \varphi u \, dz$$

$$- \varphi(z=b+h)u(z=b+h)\frac{\partial}{\partial x}(b+h)$$

$$+ \varphi(z=b)u(z=b)\frac{\partial}{\partial x}b, \qquad \text{and}$$

$$\int_b^{b+h} \frac{\partial}{\partial z}(\varphi w) \, dz = \varphi(z=b+h)w(z=b+h) - \varphi(z=b)w(z=b)$$

$$= \varphi(z=b+h)\frac{\partial}{\partial t}(b+h)$$

$$+ \varphi(z=b+h)u(z=b+h)\frac{\partial}{\partial x}(b+h)$$

$$- \varphi(z=b)\frac{\partial}{\partial t}b - \varphi(z=b)u(z=b)\frac{\partial}{\partial x}b.$$

Adding these together, we obtain

$$\int_b^{b+h} \frac{\partial}{\partial t}\varphi \, dz + \int_b^{b+h} \frac{\partial}{\partial x}(\varphi u) \, dz + \int_b^{b+h} \frac{\partial}{\partial z}(\varphi w) \, dz = \frac{\partial}{\partial t}(h\overline{\varphi}) + \frac{\partial}{\partial x}\int_b^{b+h} \varphi u \, dz$$

where

$$\overline{\varphi}(x,t) = \frac{1}{h}\int_b^{b+h} \varphi(x,z,t) \, dz$$

9

is the depth average of φ. Therefore, the depth averaged transport equation for a scalar quantity φ subject to the boundary conditions (2.6) is

$$\frac{\partial}{\partial t}(h\overline{\varphi}) + \frac{\partial}{\partial x}\int_b^{b+h} \varphi u \, dz = \int_b^{b+h} \psi \, dz. \tag{2.9}$$

Employing (2.9), the depth averaged continuity equation (2.2) is given by

$$\frac{\partial}{\partial t}(\rho h) + \frac{\partial}{\partial x}(\rho h\overline{u}) = q_e - q_d \tag{2.10}$$

and the depth averaged momentum equation (2.4) is given by

$$\frac{\partial}{\partial t}(\rho h\overline{u}) + \frac{\partial}{\partial x}\left(\rho h\beta\overline{u}^2 + \rho g\frac{h^2}{2}\right) = -\rho gh\frac{\partial b}{\partial x} - \tau_b \tag{2.11}$$

where we have introduced the shape factor (Boussinesq coefficient) β through the relations [26]

$$\beta h\overline{u}^2 = \int_b^{b+h} u^2 \, dz, \quad \beta = 1 + \frac{1}{h}\int_b^{b+h}\left(1 - \frac{u}{\overline{u}}\right)^2 dz. \tag{2.12}$$

The magnitude of $\beta \geq 1$ corresponds to the amount of shear present in the horizontal velocity field and may depend on such factors as the Reynolds number or the boundary roughness [26]. Earlier work in [39, 37, 35] has demonstrated that even in the absence of these mechanisms and with the assumption of a hydrostatic pressure field, velocity shear will always be present in particle-driven flows whenever the horizontal density gradients of the suspension are non-vanishing.

Thus far we have developed two depth averaged model equations for continuity (2.10) and momentum (2.11); and a model equation for the evolution of the bed (2.7). These equations contain the four unknowns ϕ (through ρ), h, u, and b; and therefore the system is under-determined. In order to close the system we will employ the Boussinesq approximation thereby simplifying the momentum equation and splitting the continuity equation into two equations for the conservation of (i) fluid mass and (ii) particle mass. We will do so by re-writing the density as $\rho = \rho_f + \phi\rho_\Delta$, where $\rho_\Delta = \rho_p - \rho_f$, in the mass and momentum equations.

Re-arranging the mass balance equation (2.10), we obtain

$$\rho_\Delta\left[\frac{\partial}{\partial t}(\phi h) + \frac{\partial}{\partial x}(\phi hu)\right] + \rho_f\left[\frac{\partial}{\partial t}h + \frac{\partial}{\partial x}(hu)\right] = q_e - q_d. \tag{2.13}$$

With regards to mass balance, the Boussinesq approximation is equivalent to re-

quiring that the velocity of the interstitial fluid remain divergence free, which implies that

$$\frac{\partial}{\partial t}h + \frac{\partial}{\partial x}(hu) = 0 \tag{2.14}$$

which is the canonical conservation of mass equation for shallow-water flows. Employing (2.14) in (2.13), we obtain

$$\frac{\partial}{\partial t}(\phi h) + \frac{\partial}{\partial x}(\phi h u) = \frac{1}{\rho_\Delta}\left(q_e - q_d\right) \tag{2.15}$$

which describes the conservation of particle mass through advection by the interstitial fluid and through the exchange of particles with the bed.

Re-arranging the horizontal momentum equation (2.11), we obtain

$$\rho_f\left[\frac{\partial}{\partial t}(hu) + \frac{\partial}{\partial x}\left(h\beta u^2 + \frac{\rho}{\rho_f}g\frac{h^2}{2}\right)\right]$$
$$+ \rho_\Delta\left[\frac{\partial}{\partial t}(\phi h u) + \frac{\partial}{\partial x}\left(\phi h \beta u^2\right)\right] = -\rho g h\frac{\partial b}{\partial x} - \tau_b. \tag{2.16}$$

With regards to momentum balance, employing the Boussinesq approximation means that we can ignore the $\rho_\Delta[\,\cdot\,]$ term on the left hand side of (2.16). However, instead of ignoring this term completely, we first re-write it according to

$$\begin{aligned}
\frac{\partial}{\partial t}(\phi h u) + \frac{\partial}{\partial x}\left(\phi h \beta u^2\right) &= u\frac{\partial}{\partial t}(\phi h) + \beta u\frac{\partial}{\partial x}(\phi h u)\\
&\quad + \phi h\frac{\partial u}{\partial t} + \phi h u\frac{\partial}{\partial x}(\beta u)\\
&= u\frac{\partial}{\partial t}(\phi h) + u\frac{\partial}{\partial x}(\phi h u) + (\beta - 1)u\frac{\partial}{\partial x}(\phi h u)\\
&\quad + \phi h\frac{\partial u}{\partial t} + \phi h u\frac{\partial}{\partial x}(\beta u)\\
&= u\left[\frac{\partial}{\partial t}(\phi h) + \frac{\partial}{\partial x}(\phi h u)\right]\\
&\quad + (\beta - 1)u\frac{\partial}{\partial x}(\phi h u) + \phi h\left[\frac{\partial}{\partial t}u + u\frac{\partial}{\partial x}(\beta u)\right].
\end{aligned} \tag{2.17}$$

Then, employing the particle mass balance equation (2.15), the first term on the right-hand-side becomes

$$u\frac{1}{\rho_\Delta}(q_e - q_d). \tag{2.18}$$

This represents the momentum exchanged between the fluid and bed due to the erosion and deposition of particles. When a particle at rest in the bed is entrained into the fluid it is accelerated by the fluid, thereby taking momentum away from the fluid. When a moving particle suspended in the fluid is deposited onto the

11

bed, it decelerates to rest, thereby giving its momentum to the fluid (in this model – a more physically reasonable interpretation would be that the particles would give their momentum to the bed or elsewhere). We will retain this term in the Boussinesq momentum equation as a source term and neglect the remaining terms.

In summary, the model equations for fluid mass balance, momentum balance, particle mass balance, and bed evolution are:

$$\frac{\partial}{\partial t}h + \frac{\partial}{\partial x}(hu) = 0, \tag{2.19a}$$

$$\frac{\partial}{\partial t}(\phi h) + \frac{\partial}{\partial x}(\phi h u) = \frac{1}{\rho_\Delta}(q_e - q_d), \tag{2.19b}$$

$$\frac{\partial}{\partial t}(hu) + \frac{\partial}{\partial x}\left(h\beta u^2 + \frac{\rho}{\rho_f}g\frac{h^2}{2}\right) = -\frac{1}{\rho_f}\left[\rho g h\frac{\partial b}{\partial x} + C_D\rho_f u^2 + u(q_e - q_d)\right], \tag{2.19c}$$

and

$$\frac{\partial}{\partial t}(\rho_p b) = q_d - q_e. \tag{2.19d}$$

where we have employed the Chézy drag law $\tau_b = C_D\rho_f u^2$ in the momentum equation.

At this stage we see some fundamental differences between our model for sediment transport under dam-break flow and that employed by Pritchard and Hogg [42]. In their analysis they assumed that the flow dynamics were not influenced by the particles suspended in the water column and that there was no friction acting on the flow. These two assumptions (as well as the well-mixed particulate load assumption) were essential for their Lagrangian approach to work in that it was based on the use of the known Ritter solution [45] of the shallow-water equations to provide the background flow. Given that basal friction was required in order to obtain agreement between experiment and theory for the dam-break problem involving clear water and given the influence that this term had on both the flow profile and the front speed and given that erosion is very dependent on fluid velocity this omission could be a major source of error in predicting the transport of particles in suspension. The fact that entrainment and deposition of particles is also dependent on the depth of the flow and given the influence of drag on the depth profile provides another possible source of error that can be attributed to the omission of such drag terms. The inverse dependence of the budget of particles in suspension on the depth of the flow regime has been observed experimentally in the case of purely depositional particle-driven lock-release flows in [7, 6, 8].

Most of our analysis will deal with the complex interactions between particles and flow when these relatively fine, inertia free [40] particles may be lifted into the

fluid column or deposited from it while being advected by the flow itself. This mass of suspended sediment will either increase or decrease depending upon the relative magnitudes of the mass erosion and deposition fluxes and these changes in the bulk density will, in turn, then feed back into the driving buoyancy forces which influence the rate of erosion in a nonlinear fashion through the velocity field. Since depth-averaged quantities are used throughout with the assumption of well-mixed suspensions [42, 7, 43] the model will apply to the situation in which the suspension is sufficiently dilute so that the potential energy associated with the particles is small compared to that associated with the suspending fluid.

When we examine the relatively simpler cases of particle-free dam-break flows the model equations in (2.19) will simplify to the pair of dimensional equations

$$\frac{\partial}{\partial t}h + \frac{\partial}{\partial x}(hu) = 0, \tag{2.20a}$$

$$\frac{\partial}{\partial t}(hu) + \frac{\partial}{\partial x}\left[\beta hu^2 + \frac{1}{2}gh^2\right] = -gh\frac{\partial b}{\partial x} - C_D u^2. \tag{2.20b}$$

We will solve the pure initial value problem consisting of equations (2.19) or (2.20) together with the initial conditions

$$u(x,0) = 0, \quad \phi(x,0) = 0, \quad \text{and} \quad h(x,0) = \begin{cases} h_0 & \text{if } x < 0 \\ 0 & \text{if } x > 0, \end{cases} \tag{2.21}$$

which corresponds to the complete and catastrophic collapse of a dam with clear water in its reservoir.

Finally, velocity shear can be accounted for in the model by choosing values of $\beta > 1$ [26]. However, it would seem preferable at this stage to have a more concrete reason behind our choice for the β values. This can be afforded through the approach adopted by Huang and Garcia [28], as well as others [26], in which it is assumed that the velocity profile is given by

$$u(x,z,t) = \bar{u}(x,t)\left(\frac{1+2k}{k+1}\right)\left[1 - \left(1 - \frac{z-b}{h}\right)^{\frac{k+1}{k}}\right]. \tag{2.22}$$

This velocity profile satisfies the no slip condition at the base $z = b(x)$ of the flow whereas it gives a vanishing shear stress at the free surface $z = h(x,t) + b(x)$. For this vertical structure of the flow field the shape factor β is given by

$$\beta = \frac{2(2k+1)}{3k+2}. \tag{2.23}$$

13
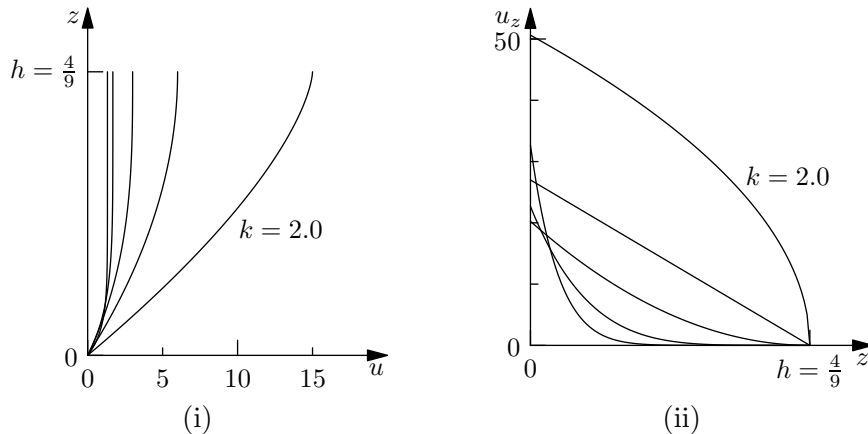
Figure 2.2: (i) Plot of depth *vs* horizontal velocity at the station $x = 0$ for the Ritter solution with $k = 0.1, 0.2, 0.5, 1.0, 2.0$. (ii) Plot of horizontal velocity shear *vs* depth at the station $x = 0$ for the Ritter solution with $k = 0.1, 0.2, 0.5, 1.0, 2.0$.

With $0 < k \leq 2$ [28] we have $1 < \beta \leq 5/4$. In Figure 2.2 we have plotted the velocity shear profile for dam-break flow over a horizontal bed at two different times and for various values of the index k at the station $x = 0$ corresponding to the initial location of the dam.

2.2 Deposition and erosion

Observations have shown that q_e and q_d are functions of both the fluid velocity u and the volume fraction of particles in suspension ϕ [50]. A wide range of empirical and semi-empirical expressions have been proposed and used to describe the entrainment and deposition of sediment yet none have, as yet, gained universal acceptance [5, 44]. We shall adopt the usual [42, 7, 6, 8, 39, 44] expression for the mass deposition rate which is appropriate for dilute suspensions where interactions amoung the particles such as those that lead to hindered settling [40] may be neglected, that is,

$$q_d = \rho_p \phi v_s \tag{2.24}$$

where v_s is the Stokes settling velocity. In the absence of entrainment, this relation results in the exponential decrease of the particle concentration (volume fraction) with time. Martin and Nokes demonstrate that the concentration of crystals settling in a vigorously convecting magma chamber also decreases exponentially, on a time scale given by the ratio of the layer depth and the settling speed, regardless of the turbulence of the ambient [34]. The Stokes settling velocity for an isolated

spherical particle in a fluid of kinematic viscosity υ is given by

$$v_s = \frac{\gamma g a^2}{18 \upsilon},$$ (2.25)

where a is the diameter of the particle [7, 39]. When there are no particles in suspension behind the dam we need only consider deposition when $u > u_c$, where u_c is some critical velocity (corresponding to a critical bed shear) below which particles are not entrained into the fluid column [42, 5, 44, 50, 22]. When models for purely depositional flows have been considered in the context of fixed volume releases corresponding to the particle-laden lock release flow experiments of [7, 6, 8, 23] the turbulence of initial mixing behind the lock has been accounted for in [38, 40]. This initial turbulence was shown to influence the deposition rates in the zone near the initial position of the lock with the most complete study of this effect being given in the recent work of Necker *et al.* [40]. Here with our infinite source of fluid this effect is not taken into account.

In this study, we consider erosion rates of the form [42, 44, 43]

$$q_e(u) = \begin{cases} \rho_p v_e \left(\frac{u^2}{u_c^2} - 1 \right)^n & \text{for } |u| \geq u_c, \\ 0 & \text{for } |u| < u_c \end{cases}$$ (2.26)

where v_e is a sediment entrainment rate and u_c is the critical velocity for entrainment of sediment referred to above which may be obtained from a Shields criterion [17] together with the Chézy closure for bottom drag [44], and n is a dimensionless exponent. Many of the models employed in the literature have a more complicated structure than that represented in (2.26) and an excellent review of these is presented in Garcia and Parker [22]. However, this model does share the principal features of all such models in that there is a critical shear stress for the entrainment of sediment and the asymptotic form $q_e \sim (\text{bed stress})^n$ [22] applies. Pritchard and Hogg [44] considered a range of values for n showing that the results obtained were robust to the functional form of the erosional relation. The sediment entrainment rate v_e has units of velocity and will be taken to be proportional to the settling velocity v_s [44].

A further justification of (2.26) is obtained by considering a particle of diameter a at rest on the bed. The particle is acted on by a gravitational force F_g equal to

$$F_g = \frac{\pi}{6} (\rho_p - \rho_f) g a^3$$ (2.27)

15

and by a dynamic pressure force F_d equal to

$$F_d = \frac{1}{8}C_D\,\rho_f\,u^2\,a^2 \tag{2.28}$$

for high particle Reynolds number where C_D here is a form drag coefficient for the particle [11]. A simple criteria for particle entrainment is that the dynamic pressure force overcomes gravity. Therefore, particles are entrained into the fluid when $F_d > F_g$ at a rate proportional to the square of the fluid velocity above some threshold, and for a given velocity u the largest particle size that can be entrained is given by

$$a_{\max} = \frac{3\,C_D\,\rho_f\,u^2}{4(\rho_p - \rho_f)g} \tag{2.29}$$

for high particle Reynolds number [11].

As mentioned in the introduction, the range of particle volume fractions $\phi(x,t)$ to which our theory, involving unhindered settling of particles, applies is constrained. At a value of $\phi \approx 0.09$ the mean free distance between particles is approximately equal to the grain diameter and the probability of collisions becomes a certainty [2]. Models for particle-laden currents in the purely depositional regime have been presented [7, 6, 8] wherein particles were allowed to be $\lesssim 5\%$ by volume of the current. More recent studies [5, 9] have limited the volume fractions to $\phi = O(10^{-2})$ and there are compelling reasons to adopt this range for the validity of the model [1].

2.3   Non-dimensional equations

We will make all equations non-dimensional using the non-dimensionalisation and scaling scheme

$$
\begin{aligned}
t = \frac{h_0}{U}\widetilde{t}, \quad x = h_0\widetilde{x}, \quad h = h_0\widetilde{h}, \quad \phi = \phi_0\widetilde{\phi}, \quad b = h_0\widetilde{b}, \\
\widehat{g} = (\gamma\phi_0 + 1)g, \quad U = \sqrt{\widehat{g}h_0}, \quad u = U\widetilde{u}, \\
q_e = U\rho_p\phi_0\widetilde{q}_e, \quad \text{and} \quad q_d = U\rho_p\phi_0\widetilde{q}_d,
\end{aligned}
\tag{2.30}
$$

where non-dimensional quantities are indicated by a tilde henceforth to be dropped from non-dimensional quantities, $\widehat{g}$ is a 'modified gravity' which for our parameter values lies in the range $1.15g \leq \widehat{g} \leq 1.25g$, the dimensionless parameter $\gamma = (\rho_p - \rho_f)/\rho_f$, and the typical velocity scale U is the buoyancy velocity.

16
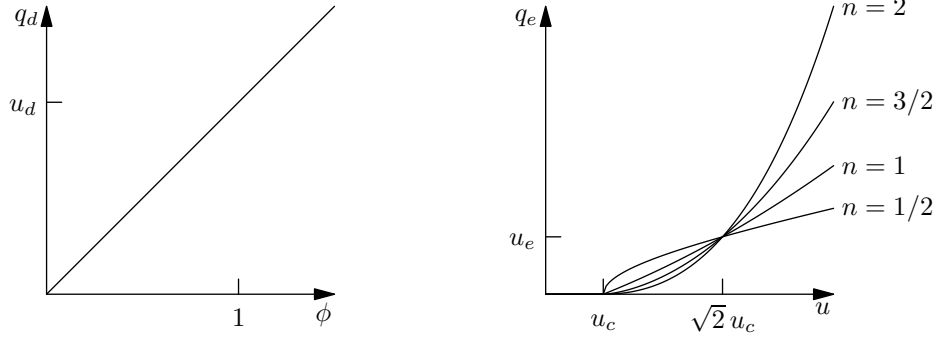
Figure 2.3: Dimensionless deposition and erosion terms.

Rendering equations (2.19), (2.24), and (2.26), non-dimensional gives

$$\frac{\partial}{\partial t}h + \frac{\partial}{\partial x}(hu) = 0, \tag{2.31a}$$

$$\frac{\partial}{\partial t}(hu) + \frac{\partial}{\partial x}\left[\beta hu^2 + \frac{1}{2}\Gamma(\phi)h^2\right] = -h\Gamma(\phi)b_x - C_D u^2 - \phi_0(\gamma+1)u(q_e - q_d), \tag{2.31b}$$

$$\frac{\partial}{\partial t}(\phi h) + \frac{\partial}{\partial x}(\phi hu) = q_e - q_d, \tag{2.31c}$$

$$q_d = u_d\phi, \tag{2.31d}$$

$$q_e(u) = \begin{cases} u_e\left(\frac{u^2}{u_c^2} - 1\right)^n & \text{for } |u| \geq u_c, \\ 0 & \text{for } |u| < u_c \end{cases} \tag{2.31e}$$

and

$$\frac{\partial}{\partial t}b = -\phi_0(q_e - q_d) \tag{2.31f}$$

where we have introduced the non-dimensional function $\Gamma(\phi) = (\phi\,\phi_0\gamma + 1)/(1 + \gamma\phi_0)$ for convenience as well as $u_d = v_s/U$ and $u_e = v_e/U\phi_0$ for the dimensionless deposition and erosion terms, respectively.

The dimensionless deposition and erosion terms (2.31d) and (2.31e) are plotted in Figure 2.3. In this figure we see that the mass erosion rate is much more sensitive to changes in the value of the exponent n when the horizontal fluid velocity exceeds $\sqrt{2}\,u_c$. We also note that the curves $q_e(u)$ are concave up when $(2n-1)u^2/u_c^2 - 1 > 0$ and concave down when $(2n-1)u^2/u_c^2 - 1 < 0$ so that they are always concave up for $n \geq 1$ which is the typical range for this exponent [42, 44].

In the case of particle-free dam-break flows, the model equations (2.20) reduce to the non-dimensional form

$$\frac{\partial}{\partial t}h + \frac{\partial}{\partial x}(hu) = 0, \tag{2.32a}$$

17

$$\frac{\partial}{\partial t}(hu) + \frac{\partial}{\partial x}\left[hu^2 + \frac{1}{2}h^2\right] = -h\frac{\partial b}{\partial x} - C_D u^2. \tag{2.32b}$$

The non-dimensionalised initial conditions for the complete and catastrophic failure of a dam are

$$u(x,0) = 0, \quad \phi(x,0) = 0, \quad \text{and} \quad h(x,0) = \begin{cases} 1 & \text{if } x < 0 \\ 0 & \text{otherwise .} \end{cases} \tag{2.33}$$

2.4 Front position

The front position x_f of the flow is the position of the point at which the height field vanishes. It is an important property of the flow field especially for hazard management, as it describes how fast the front of the flow travels. For a particle-free dam-break flow in the absence of drag, we can determine x_f by solving equation (1.1) with $h = 0$ for x to obtain

$$x_f = 2t\sqrt{gh_0}, \tag{2.34}$$

which, in terms of our non-dimensional variables, is $x_f = 2t$. This will act as an important benchmark to which other flow configurations will be compared.

In most of the literature on compositionally-driven gravity currents [46, 47] the usual scenario involves the deployment of a two-layer shallow-water theory (very often with a rigid lid approximation) as the mathematical model for the study of fixed-volume lock-release flows that are compositionally-driven [46]. These flows in their post-release phase involve a dense (usually saline) bottom-hugging current that displaces a lighter ambient fluid (usually fresh water) as it moves under gravitational collapse along a rectangular channel. These gravity currents have a distinctive shape with a rather thick head or front and a rather thinner tail whose thickness varies slowly in both space and time. The usual practise, in order to achieve better agreement between the shallow-water theory based solutions and the lock-release experiments, is to introduce an empirical front condition of the general form [46, 47, 41]

$$u_f^2 = \frac{\beta^2}{2} \frac{2 - h_f/H}{1 + h_f/H} \left(1 - h_f/H\right) g' h_f, \tag{2.35}$$

where $u_f(t)$ is the front speed, $h_f(t)$ is the front depth, H is the total depth of the two fluid system, g' the usual reduced gravity, and β is a dimensionless parameter

18

that is determined experimentally. A full discussion of the various front conditions that are employed in this approach to lock-release flows to bring observation and theory into closer accord is contained in [41]. Essentially, the use of conditions like (2.35) mean that the current front is being treated similarly to a hydraulic jump. On the other hand in the case of dam-break flows the underlying flow derived from the shallow-water equations has zero depth at the front since there is no fluid to be displaced by the bottom-hugging current and so the necessary modifications to bring the model solutions into closer agreement with the experimental observations do not involve imposing a depth-dependent front condition but rather a drag term of the Chézy type [53, 15, 26, 4]. Since this drag appears as a source (sink) term in the shallow-water equations we avoid the mathematical difficulties inherent in the introduction of a traveling discontinuity that may violate the Rankine-Hugoniot conditions.

2.5 Conservative variables

In order to emphasise the mathematical differences that exist between our model approach and that of Pritchard and Hogg [42] as well as to set up our system of equations in the form that the numerical scheme will most easily handle we write the equations (2.31) in the form of a hyperbolic balance law

$$\frac{\partial}{\partial t} \boldsymbol{q} + \frac{\partial}{\partial x} \boldsymbol{f}(\boldsymbol{q}) = \boldsymbol{\psi}(\boldsymbol{q}) \tag{2.36}$$

where we have introduced the quantities $\boldsymbol{q} = (q_1, q_2, q_3, q_4)^T = (h, uh, \phi h, b)^T$,

$$\boldsymbol{f}(\boldsymbol{q}) = \begin{pmatrix} q_2 \\ q_2^2/q_1 + \nicefrac{1}{2}\,\Gamma(q_3/q_1)\,q_1^2 \\ q_2 q_3/q_1 \\ 0 \end{pmatrix} = \begin{pmatrix} uh \\ hu^2 + \nicefrac{1}{2}\,\Gamma(\phi)h^2 \\ uh\phi \\ 0 \end{pmatrix}, \tag{2.37}$$

and

$$
\boldsymbol{\psi}(\boldsymbol{q}) = \begin{pmatrix} 0 \\ -q_1\Gamma(q_3/q_1)\frac{\partial q_4}{\partial x} - C_D(q_2/q_1)^2 - (\gamma+1)\,q_2/q_1\,(q_e - q_d) \\ q_e - q_d \\ -\phi_0(q_e - q_d) \end{pmatrix}
$$

$$
= \begin{pmatrix} 0 \\ -h\Gamma(\phi)\frac{\partial b}{\partial x} - C_D u^2 - (\gamma+1)\,u\,(q_e - q_d) \\ q_e - q_d \\ -\phi_0(q_e - q_d) \end{pmatrix}.
$$
(2.38)

The function $\boldsymbol{f}(\boldsymbol{q})$ is called the flux vector and $\boldsymbol{q}$ the vector of field variables. The Jacobian $\boldsymbol{f}'$ of the flux vector (excluding the bed equation) is

$$
\boldsymbol{f}' = \begin{pmatrix} 0 & 1 & 0 \\ -u^2 + \frac{\phi h}{2}\left(1 - \frac{1}{\gamma\phi_0+1}\right) + \frac{h}{\gamma\phi_0+1} & 2u & \frac{h}{2}\left(1 - \frac{1}{\gamma\phi_0+1}\right) \\ -\phi u & \phi & u \end{pmatrix}
$$
(2.39)

and the characteristic wave speeds (ie, the eigenvalues of $\boldsymbol{f}'$) are

$$
u \quad \text{and} \quad u \pm \sqrt{\phi h\left(1 - \frac{1}{\gamma\phi_0+1}\right) + \frac{h}{\gamma\phi_0+1}}.
$$
(2.40)

From the above results we see that our system is strictly hyperbolic and that with the eigenvalues denoted $\lambda_1 = u$ and $\lambda_{2,3} = u \pm \sqrt{\phi h(1 - 1/(\gamma\phi_0+1)) + h/(\gamma\phi_0+1)}$ the characteristic field associated with λ_1 is linearly degenerate (ie, $\boldsymbol{\nabla_q}\,\lambda_1 \cdot \boldsymbol{r}_1 \equiv 0$ where r_1 is the associated right eigenvector) whereas the characteristic fields associated with $\lambda_{2,3}$ are genuinely nonlinear (ie, $\boldsymbol{\nabla_q}\,\lambda_{2,3} \cdot \boldsymbol{r}_{2,3} \neq 0$). For future reference we include the (non-normalised) right eigenvectors associated with our strictly hyperbolic system. They are

$$
\boldsymbol{r}_1 = \begin{pmatrix} 1 \\ u \\ -\phi - 2/(\gamma\phi_0) \end{pmatrix}, \quad \text{and}
$$

$$
\boldsymbol{r}_{2,3} = \begin{pmatrix} 1 \\ u \pm \sqrt{\phi h\left(1 - \frac{1}{\gamma\phi_0+1}\right) + \frac{h}{\gamma\phi_0+1}} \\ \phi \end{pmatrix}.
$$
(2.41)

We note that as $\gamma \to 0$ in (2.41) we obtain the two characteristic wave speeds

20

$u \pm \sqrt{h}$ that underly the particle-free equations that were employed by Pritchard and Hogg [42].

In our formulation of particle entrainment and transport for fine cohesive sediment we are assuming that the advective transport of particles dominates diffusive transport [43] and that the mass exchange fluxes may be expressed in terms of the vertically averaged volume fraction of particles $\phi(x,t)$, and the vertically averaged velocity $u(x,t)$. This depth-averaged approach is appropriate when the characteristic vertical length scale of the flow is very much smaller than the horizontal length scale [43]. This assumption of small aspect ratio flows is at the heart of most of the theories developed for particle-driven flows whether with or without re-entrainment of particles [42, 7, 6, 8, 39, 38, 37, 44, 43] and certainly underlies all of the theoretical treatments of dam-break flows [53, 45, 16, 15, 26, 54] and we have adopted this approach throughout our analysis. We believe that the model presented here provides a leading-order description of the phenomena under discussion in the present study.

Chapter 3

Asymptotic results

In this chapter we consider two limiting cases of the particle-free model (2.20): (i) small drag and (ii) gently sloping linear beds. The small drag case is a brief review of the results of Hogg and Pritchard [26]. The gently sloping linear bed case is original work.

3.1 Drag

For simple particle- and drag-free dam-break flows over flat beds ($C_D \equiv 0$, $\beta \equiv 1$, and $b(x,t) \equiv 0$), the exact solution to the model equations (2.20) together with the initial conditions (2.21) is the well-known Ritter solution (1.1) for $-1 < x/t < 2$. From this solution various asymptotic methods have been employed [15, 53, 54, 26] to isolate and determine the influence of drag ($0 < C_D \ll 1$). The most complete analysis was carried out by Hogg and Pritchard [26] using more precise asymptotic techniques than were available to earlier authors. The result of their analysis is summarised in Figure 3.1 where we have plotted the first order correction (in C_D for $C_D \ll 1$) to the height profile and front position of the Ritter solution (1.1). This result affords us the opportunity to compare our numerical solver to a theoretical result.

In Figure 3.2 we have plotted the height profile of a simple dam-break flow with drag obtained by our numerical solver. Qualitatively the numerical solution matches the corrected solutions quite well, although the front position of the numerical solution is slightly more retarded than the first order correction. However, as can also be seen in Figure 3.2, the numerical solution is also deeper in the bulk of the fluid behind the front due to higher order effects. As such, since mass is conserved,
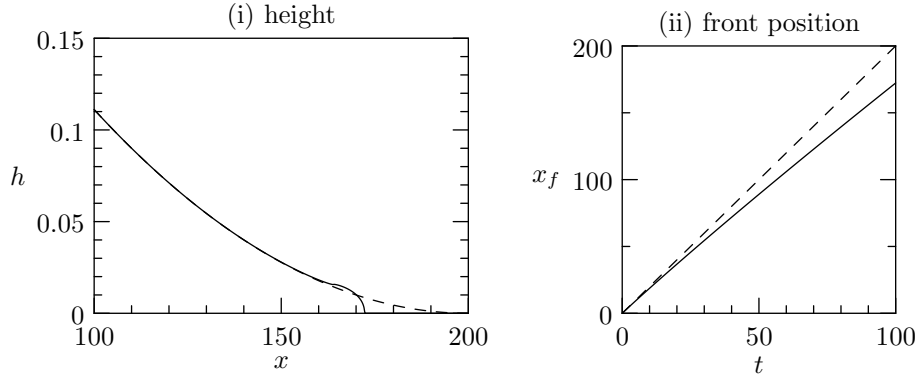
Figure 3.1: (i) Height profile of the Ritter solution (dashed) and first order correction (solid) for a simple dam-break flow with drag at $t = 100$. (ii) Front position of the Ritter solution (dashed) and first order correction (solid) for a simple dam-break flow with drag. Parameter value used was $C_D = 0.00001$.
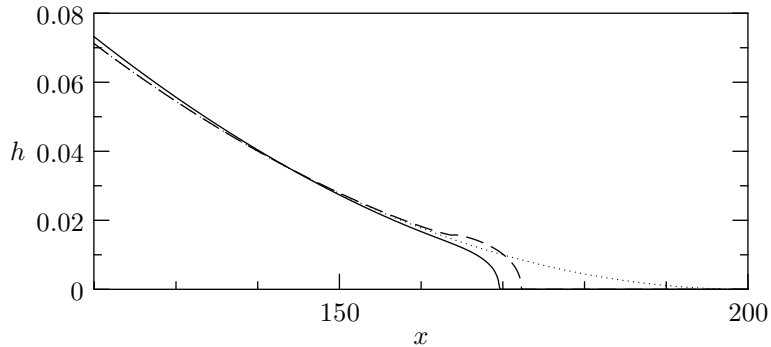
Figure 3.2: Height profile of the Ritter solution (dotted), first order correction (dashed), and numerical solution (solid) for a simple dam-break flow with drag at $t = 100$. Parameter value used is $C_D = 0.00001$.

the front will contain less fluid and travel slightly slower than the first order correction. In each case, the height profile decreases quadratically in the bulk of the fluid and forms a blunt snout at the front that is significantly retarded compared to the Ritter solution. Quantitatively, at $t = 100.0$ the front positions of the corrected and numerical solutions only differ by 2%.

In Figure 3.3 we have plotted the front position x_f at $t = 100.0$ versus the drag coefficient C_D obtained by our numerical solver. The discrepancy between the numerical and theoretical results decreases as the drag coefficient C_D is taken smaller until $C_D \approx 2 \times 10^{-5}$. This is expected as the theoretical result is a first order correction for $C_D \ll 1$ to the Ritter solution and becomes more accurate as C_D is taken smaller. For $C_D \leq 2 \times 10^{-5}$ the discrepancy appears to increase as C_D decreases, although the relative error is still quite small. In any case, the

23
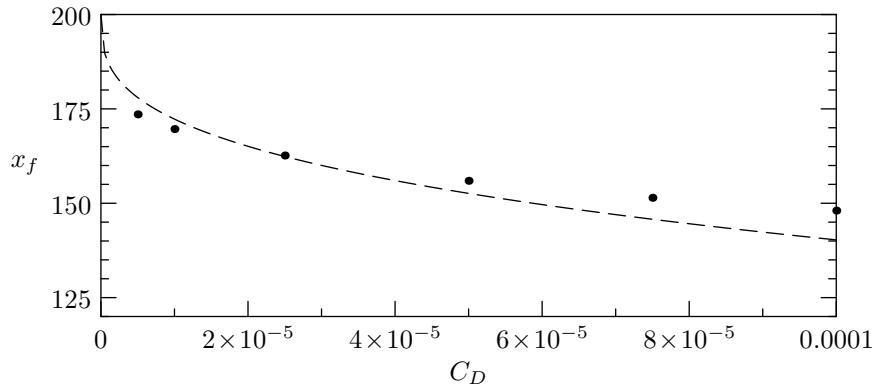
Figure 3.3: Front position x_f at $t = 100.0$ of the first order correction (dashed line) and numerical solution (dots) for various values of the drag coefficient C_D. The grid spacing used in all of the simulations is $\Delta x = 0.1$.
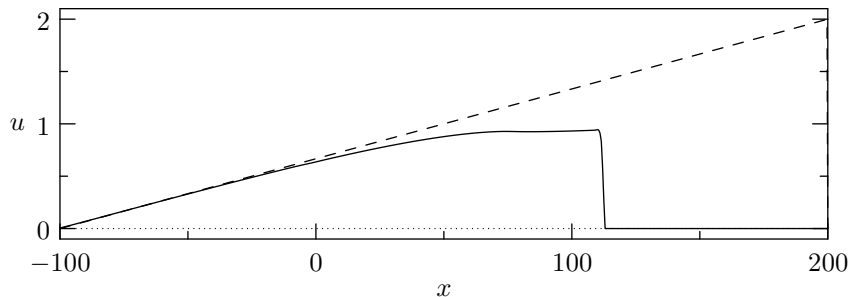
Figure 3.4: Velocity of a particle-free dam-break flow over a flat bottom with basal drag at $t = 100$. Solid lines indicate numerical solutions and dashed lines show the Ritter solutions. Parameter values used are $C_D = 0.001$ and $\beta = 1.0$.

solver performs well and the numerical results are consistent with the theoretical corrections of Hogg and Pritchard[26].

Finally, in Figure 3.4 we have plotted the velocity profile of a particle-free dam-break flow with drag. In agreement with the experimental results [16] and the theoretical approach adopted in [53], we note that the velocity is nearly uniform in the blunt snout. That is, in the deformed tip basal drag retards the flow so that the velocity profile is approximately horizontal there. The assumption that the velocity in the tip depends only on time was crucial to the theoretical development in [53] and appears to be confirmed by our numerical work.

3.2 Linear bed slope

In a similar manner to the previous section, we look for a solution close to the Ritter solution for slightly sloping linear beds. This involves solving the initial value problem consisting of equations (2.32) with $C_D \equiv 0$ and $\beta \equiv 1$ together with the initial conditions of equation (2.21). We shall take the bottom topography to be specified by

$$b(x) = -sx\Theta(x) \tag{3.1}$$

where s is a small non-dimensional parameter and Θ is the Heaviside step function. Employing this simple linear form for the bottom topography allows us to explore the effects of sloping bed topography and appeal to our intuition while interpreting both theoretical and numerical results. Furthermore, the streamwise gradient of a linear slope is constant, affording us the opportunity to perform an asymptotic expansion over the bed slope s.

We begin by performing an asymptotic analysis of the initial value problem by looking for solutions of the form

$$
\begin{aligned}
h(x,t) &= h^{(0)}(x,t) + sh^{(1)}(x,t) + O(s^2) \\
u(x,t) &= u^{(0)}(x,t) + su^{(1)}(x,t) + O(s^2)
\end{aligned}
\tag{3.2}
$$

with $s \ll 1$. The conservation of momentum equation can be re-written as

$$\frac{\partial}{\partial t} u + \frac{\partial}{\partial x}\left[h + \frac{1}{2}u^2\right] = s\Theta(x) \tag{3.3}$$

by evaluating the partial derivatives in the momentum equation and employing the mass conservation equation in (2.20) and also employing (3.1). The leading order system is

$$
\begin{aligned}
\frac{\partial}{\partial t} h^{(0)} + \frac{\partial}{\partial x}\left[h^{(0)}u^{(0)}\right] &= 0 \\
\frac{\partial}{\partial t} u^{(0)} + \frac{\partial}{\partial x}\left[h^{(0)} + \frac{1}{2}(u^{(0)})^2\right] &= 0
\end{aligned}
\tag{3.4}
$$

of which the solution is the Ritter solution

$$h^{(0)}(x,t) = \frac{1}{9}\left(2 - \frac{x}{t}\right)^2 \quad \text{and} \quad u^{(0)}(x,t) = \frac{2}{3}\left(1 + \frac{x}{t}\right). \tag{3.5}$$

The first order system is

$$\frac{\partial}{\partial t}h^{(1)} + \frac{\partial}{\partial x}\left[h^{(0)}u^{(1)} + h^{(1)}u^{(0)}\right] = 0$$
$$\frac{\partial}{\partial t}u^{(1)} + \frac{\partial}{\partial x}\left[h^{(1)} + u^{(0)}u^{(1)}\right] = \Theta(x) \tag{3.6}$$

which is written in matrix form as

$$\boldsymbol{q}_t + \boldsymbol{A}\boldsymbol{q}_x = \boldsymbol{B}\boldsymbol{q} + \boldsymbol{d} \tag{3.7}$$

where (dropping the '(1)' super-scripts)

$$\boldsymbol{q} = \begin{pmatrix} h \\ u \end{pmatrix}, \quad \boldsymbol{A} = \begin{pmatrix} u^{(0)} & h^{(0)} \\ 1 & u^{(0)} \end{pmatrix} = \begin{pmatrix} 2/3(1 + x/t) & 1/9(2 - x/t)^2 \\ 1 & 2/3(1 + x/t) \end{pmatrix},$$
$$\boldsymbol{B} = -\begin{pmatrix} u^{(0)} & h^{(0)} \\ 1 & u^{(0)} \end{pmatrix}_x = \begin{pmatrix} -2/3t & 2/9t(2 - x/t) \\ 0 & -2/3t \end{pmatrix}, \quad \text{and} \quad \boldsymbol{d} = \begin{pmatrix} 0 \\ \Theta(x) \end{pmatrix}. \tag{3.8}$$

The eigenvalues of $\boldsymbol{A}$ are

$$\lambda_1 = x/t \quad \text{and} \quad \lambda_2 = 1/3(4 + x/t), \tag{3.9}$$

and the eigenvectors are

$$\boldsymbol{v}_1 = \begin{pmatrix} -1/3(2 - x/t) \\ 1 \end{pmatrix} \quad \text{and} \quad \boldsymbol{v}_2 = \begin{pmatrix} 1/3(2 - x/t) \\ 1 \end{pmatrix}. \tag{3.10}$$

Diagonalising the system using $\boldsymbol{w} = \boldsymbol{R}^{-1}\boldsymbol{q}$, we obtain

$$\boldsymbol{w}_t + \begin{pmatrix} x/t & 0 \\ 0 & 1/3(4 + x/t) \end{pmatrix}\boldsymbol{w}_x = \begin{pmatrix} -1/t & -1/3t \\ 0 & 0 \end{pmatrix}\boldsymbol{w} + \begin{pmatrix} \Theta(x)/2 \\ \Theta(x)/2 \end{pmatrix} \tag{3.11}$$

with zero initial conditions. The w_2 equation is decoupled from the w_1 equation, and is

$$\frac{\partial}{\partial t}w_2 + \frac{4 + x/t}{3}\frac{\partial}{\partial x}w_2 = \frac{\Theta(x)}{2}. \tag{3.12}$$

Characteristics, parameterised by σ, for the above are solutions to

$$\frac{dx}{d\sigma} = \frac{4 + x/t}{3}, \quad \frac{dt}{d\sigma} = 1, \quad \text{and} \quad \frac{dw_2}{d\sigma} = \frac{\Theta(x)}{2}. \tag{3.13}$$

Solving the x and t equations, we obtain the characteristic ground curve

$$2\sigma^{2/3} - x\sigma^{-1/3} = C_2 \quad \text{and} \quad t = \sigma. \tag{3.14}$$

26
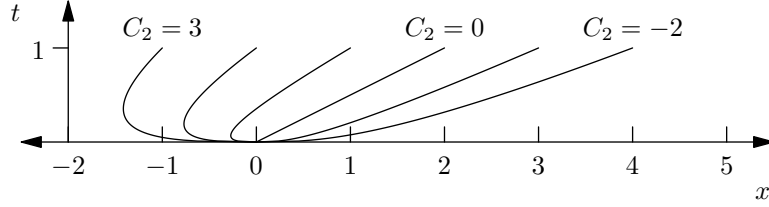
Figure 3.5: Characteristic ground curves (3.14). The constant $C_2 = -2, -1, 0, 1, 2, 3$ from right to left.

Several of these characteristic ground curves are plotted in Figure 3.5. We note that all of the curves pass through the origin in the x-t plane and eventually satisfy $x > 0$.

Along the characteristic ground curves (3.14), the w_2 equation becomes

$$\frac{dw_2}{dt} = \frac{\Theta(x)}{2} = \begin{cases} 1/2 & \text{if } x > 0 \\ 0 & \text{if } x < 0. \end{cases} \tag{3.15}$$

That is, w_2 remains constant and equal to zero when $x < 0$, and grows linearly with time when $x > 0$. Therefore

$$w_2 = \frac{t - t^*}{2} \tag{3.16}$$

where t^* is the time at which the characteristic ground curve (3.14) crosses $x = 0$. To determine t^* we first note that C_2 is determined by

$$C_2 = 2t^{2/3} - xt^{-1/3}. \tag{3.17}$$

Furthermore, at t^* we have $x = 0$ and hence

$$t^* = \left(C_2/2\right)^{3/2}. \tag{3.18}$$

The above is summarised by

$$w_2(x, t) = \begin{cases} \frac{t - t^*}{2} & \text{if } x > 0 \text{ and } t > t^* \\ 0 & \text{otherwise} \end{cases} \tag{3.19}$$

where

$$t^* = \max\left[0, \left(\frac{2t^{2/3} - xt^{-1/3}}{2}\right)^{3/2}\right]. \tag{3.20}$$

Note that $x = 2t$ implies $C_2 = 0$, and that $t^* = 0$ for $x \geq 2t$.

27

Employing the solution for w_2 (3.19) in the diagonal system for $\boldsymbol{w}$ (3.11) we obtain two cases: $t < t^*$ and $t > t^*$.

CASE 1: $t < t^*$

In this case, along the characteristic ground curve the equation for w_1 becomes

$$\frac{dw_1}{d\sigma} = -\frac{1}{t}w_1 + \frac{\Theta(x)}{2}. \tag{3.21}$$

Solving the above, we obtain

$$w_1(x, t) = \begin{cases} 0 & \text{if } x < 0 \\ t/4 & \text{if } x > 0. \end{cases} \tag{3.22}$$

CASE 2: $t > t^*$

In this case, along the characteristic ground curve the equation for w_1 becomes

$$\frac{dw_1}{d\sigma} = -\frac{1}{t}w_1 - \left(\frac{1}{3t}\frac{t - t^*}{2} + \frac{1}{2}\right)\Theta(x) \tag{3.23}$$

subject to $w_1(t^*) = t^*/4$ if $C_1 > 0$. Solving the above, we obtain

$$w_1(x, t) = \begin{cases} 0 & \text{if } x < 0 \\ -\frac{(t-t^*)^2}{12t} + \frac{t}{4} & \text{if } x > 0. \end{cases} \tag{3.24}$$

The height and velocity fields are reconstructed from the solutions for w_1 and w_2 through $\boldsymbol{q} = \boldsymbol{R}\boldsymbol{w}$.

In Figure 3.6 we have plotted the first order height and velocity corrections for a particle-free dam-break flow over a sloping bottom according to (3.1) at $t = 300$. The height correction in (i) shows an abrupt decrease in the height profile at $x = 0$ where the bed begins to slope downward, and a slight bulking up of the fluid in the body of the flow closer to the front. The height correction is parabolic with its maximum occurring over the sloping bed and behind the front. The height correction falls to zero at $x = 2t$ so that, to first order, the sloping bed does not affect the front position. The velocity correction in (ii) shows that the fluid moves faster everywhere over the sloping region of the bed, and it attains its maximum at the front.

In Figure 3.7 we have plotted the height profiles of both the asymptotic and numerical solutions for particle free dam-breaks flows over sloping beds according

28
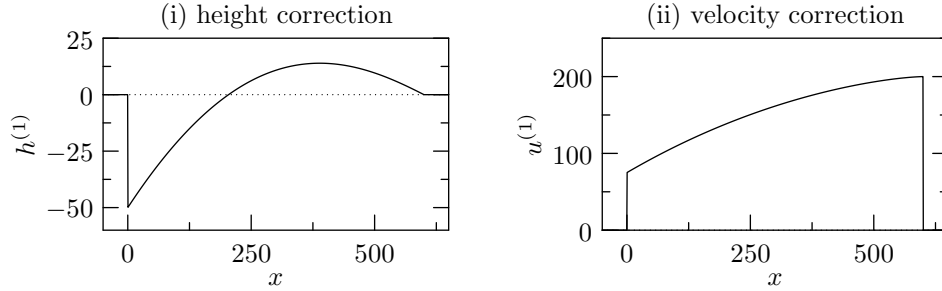
Figure 3.6: First order (i) height and (ii) velocity (ie, $h^{(1)}$ and $u^{(1)}$) corrections of the particle-free dam-break flow over a sloping bed at $t = 300$.
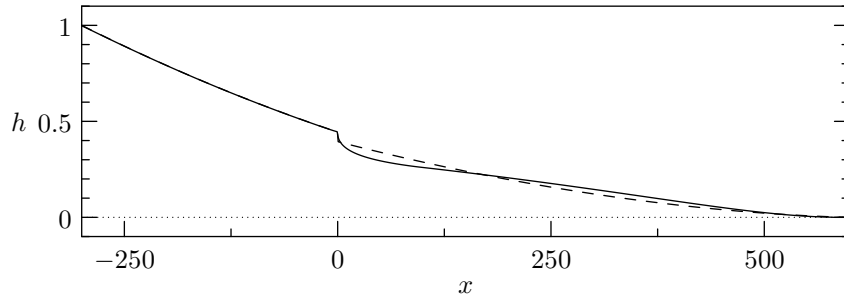
Figure 3.7: Height profile of a particle-free dam-break flow over a sloping bed at $t = 300$. Solid line shows numerical solutions. Dashed line shows first-order asymptotic solutions. Parameter values used are $C_D = 0$, $\beta = 1.0$ and $s = 0.001$.

to (3.1) at $t = 300$. The numerical solutions are consistent with the first-order asymptotic solutions. The abrupt decrease in the height profile directly downstream of the dam and the bulking up of the fluid in the body of flow behind the front present in the asymptotic solution, as exhibited in the asymptotic height correction in Figure 3.6, are also present in the numerical solution. However, both the slumping directly downstream of the dam and the bulking up in the body of the flow behind the front are more pronounced in the numerical solution.

Chapter 4

Numerical results

In this chapter we present numerical results for various configurations. We begin with the simplest case of simple ($\beta \equiv 1$) particle-free ($\phi \equiv 0$) dam-break flows over flat beds, and subsequently make the configurations more complex by the addition of drag and more complicated bottom topography.

4.1   Simple ($\beta \equiv 1$) dam-break flows

4.1.1   Particle free, without drag, flat bed

We solve the particle-free model equations (2.20) without basal friction (ie, $C_D \equiv 0$) over a flat bed ($b \equiv 0$). This is the classic dam-break flow for which the solution (1.1) is well known. It is representative of flows with sufficiently low aspect ratio and negligible basal drag whose dynamics are governed by the balance between the fluid's inertia and the horizontal pressure gradient. We consider it here as a test case for our numerical scheme, and to establish the scales used in our non-dimensionalisation scheme (2.30).

In Figure 4.1 we have plotted the height profiles of both the exact, well known Ritter solution, and the numerical solution at two times. We note that the exact and numerical profiles are almost indistinguishable. The excellent agreement between the solutions gives us confidence that our numerical scheme is producing the correct solution. Finally, we note that the front speed here is constant and equal to $2\sqrt{gh_0}$, and that, at $t = 100$ the flow extends to $x = 2t = 200$ non-dimensional spatial units.
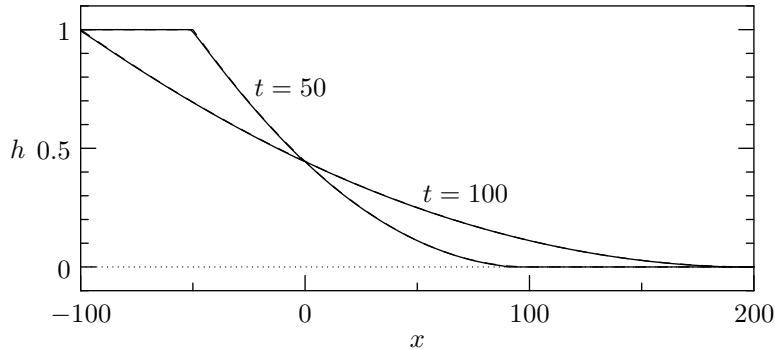
Figure 4.1: Height profile for a simple dam-break flow. Two plots at $t = 50$ and $t = 100$. Solid lines show numerical solutions, dashed lines show exact solutions.

These height profiles demonstrate the simple wave structure of the Ritter solution, which connects the constant states of $h = 1$ and $h = 0$ with a rarefaction wave that is a function of the similarity variable $\xi = x/t$. Adding hydraulic resistance through the mechanism of basal drag will destroy this structure as the conservation of momentum law becomes non-homogeneous.

4.1.2 Particle-free, with drag, flat bed

We solve the particle-free model equations (2.20) with drag included (ie, $C_D \neq 0$) over a flat bed ($b \equiv 0$). That is, following the approaches of Dressler [15], Whitham [53, 54], and Hogg and Pritchard [26], we introduce a basal drag term into the horizontal momentum equation in order to bring our model calculations into closer accord with the experimental results of Dressler [15]. These flows are representative of flows with sufficiently low aspect ratios whose dynamics are governed by the balance among the fluid's inertia, the horizontal pressure gradient, and basal drag. Our results can be directly compared with the asymptotic analysis of Hogg and Pritchard [26], and establish the effects of hydraulic resistance through the mechanism of basal drag.

Basal drag acts over the full length of the flow but its effects are most prominent in the vicinity of the tip where the unimpeded flow has a depth that falls to zero in a continuous fashion. We do not impose any dynamic conditions at the front as in [46, 47]; the front position emerges as part of the solution and corresponds to where the height field vanishes. Thus, denoting the front position by $x_f(t)$ it satisfies

$$h(x_f, t) = 0 \quad \text{and} \quad \frac{dx_f}{dt} = u(x_f, t). \tag{4.1}$$

31
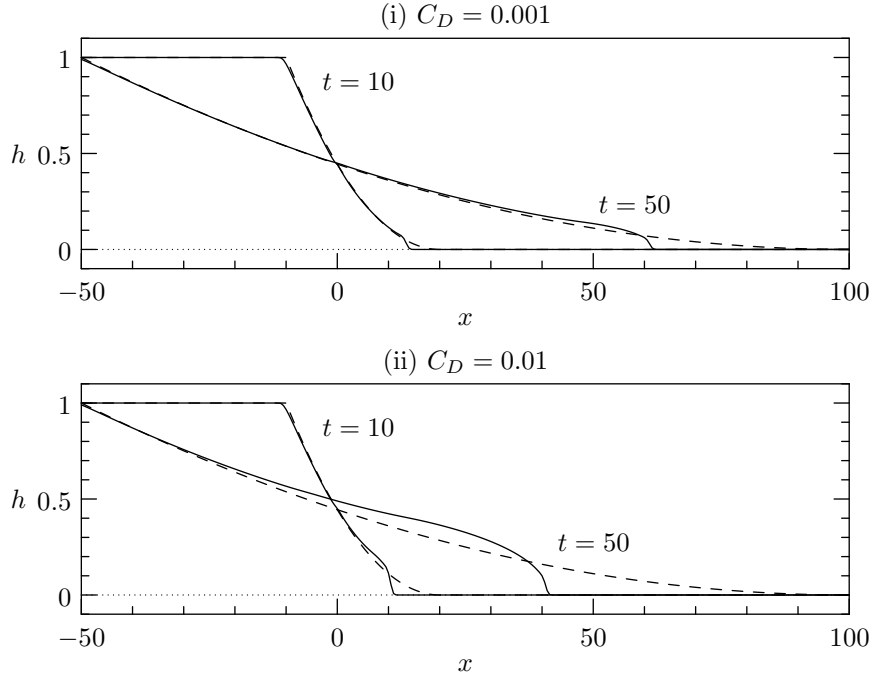
Figure 4.2: Height profile of a particle-free dam-break flow with basal drag. Two plots at $t = 10$ and $t = 50$. Solid lines show numerical solutions, dashed lines show Ritter solutions. Parameter values used are (i) $C_D = 0.001$ and (ii) $C_D = 0.01$.

All of the dynamic front conditions [41] are essentially of the form shown in (2.35) and so would lead to a zero front speed when the depth field falls to zero.

In Figure 4.2 and Figure 4.3 we have plotted the height and velocity profiles, respectively, for both the classic Ritter solution [45] and the numerical solution of (2.20) including basal drag for two distinct times. We note immediately that the presence of drag has significantly altered the shape of the depth profile in the vicinity of the leading edge as well as the velocity structure of the flow near the front. However, in agreement with the results of Hogg and Pritchard [26], and in accord with the experimental results of Dressler [15], the bulk of the flow is unaffected by the addition of this basal drag. The shape of the tip is significantly altered compared to the Ritter solution such that rather than decreasing smoothly to zero with a parabolic profile the depth of the flow decreases abruptly to form a blunt snout at the leading edge. This increased role of the drag at the front reflects the fact that because the depth of the flow there is small and since momentum is the product of depth and velocity this reduced momentum enables the effect of the drag to be accentuated at the front.

There are several further observations that can be made regarding Figs. 4.2 and 4.3 where the detailed profiles of both the depth of flow and the horizontal velocity are
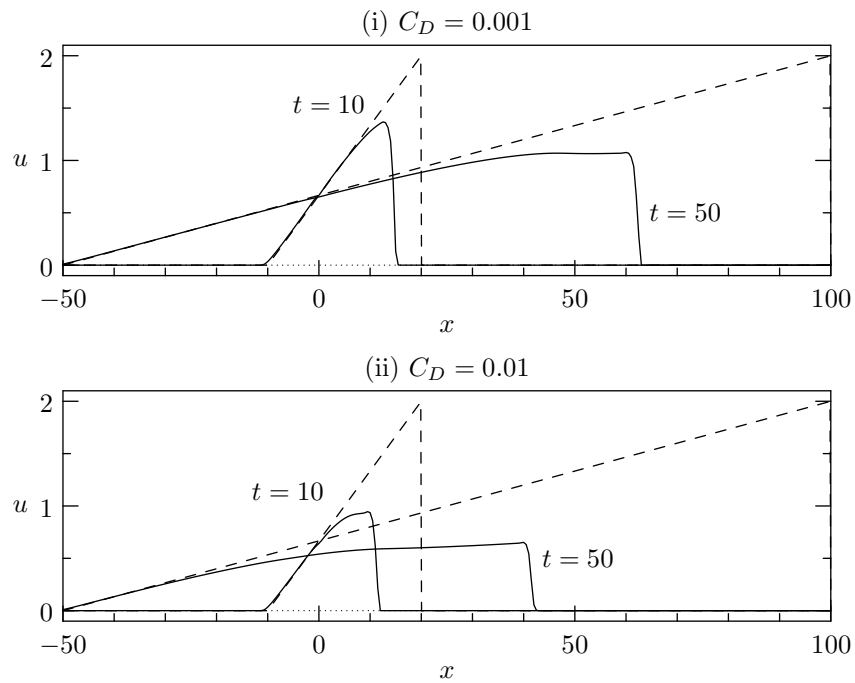
Figure 4.3: Horizontal velocity of a particle-free dam-break flow with basal drag. Two plots at $t = 10$ and $t = 50$. Solid lines show numerical solutions, dashed lines show Ritter solutions. Parameter values used are (i) $C_D = 0.001$ and (ii) $C_D = 0.01$.
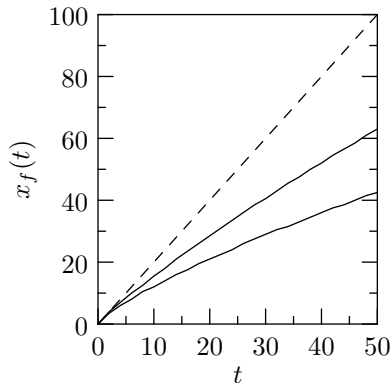
Figure 4.4: Front position of a particle-free dam-break flow with basal drag. Solid lines show the numerical solutions, dashed line shows the Ritter solution. Parameter values used are $C_D = 0.001$ (middle profile) and $C_D = 0.01$ (bottommost profile).

displayed. First, given that the particle conservation equation has a source term that is inversely proportional to the depth of the flow field means that changes in this depth brought about by the inclusion of basal friction will have an influence on how the volume fraction of particles in suspension evolves in space and time. Also the fact that this basal friction impedes the flow by differing amounts according to the values taken for the Chézy drag coefficient C_D will be reflected in the rate of erosion in a nonlinear fashion through the erosion model of equation (2.26). These influences were not included in the model for sediment transport under dam-break flow presented by Pritchard and Hogg [42]. Furthermore, in agreement with the experimental results of Dressler [15] and the theoretical approach adopted by Whitham [53], we note from the detailed profiles of the velocity field presented in Figure 4.3 that the velocity is nearly uniform in the blunt snout. That is, in the deformed tip basal drag retards the flow so that the velocity profile is approximately horizontal there. This observation that the velocity in the tip depends only on time was the basis of Whitham's asymptotic approach [53] to including basal drag in the dam-break problem and serves to justify why studying the full depth and velocity profiles is of importance.

In Figure 4.4 we have plotted the front position of both the classic Ritter solution and the numerical solution with basal drag. We note that the flow with basal drag is significantly retarded compared to the flow without basal drag. The front speed of the Ritter solution is constant and equal to 2, while the front speed of the numerical solution with drag is non-constant and decreases with time until the effect of drag balances the fluid's inertia.

34

4.1.3 Particle laden, with drag, flat bed

In this subsection we shall explore the complex interactions between particles and flow when basal drag, erosion, and sedimentation are taken into account. We will demonstrate the role played by the critical bed velocity u_c in the long term competition between erosion and deposition and display the strong effect of basal drag on the ultimate outcome of this competition. Inclusion of this frictional term in models for suspended sediment transport via dam-break flows appears to be a new addition to the literature [42] and the effect of its inclusion is often dominant over other mechanisms in determining the efficacy of this mode for sediment transport.

We solve the model equations (2.19) with particles and basal drag. That is, we consider particle laden dam-break flows with basal drag. These flows are representative of flows with sufficiently low aspect ratio whose dynamics are governed by the balance between the fluid's inertia, the horizontal pressure gradient, basal drag, and the presence of a changing particle volume fraction or concentration through the mechanisms of particle advection, deposition, and entrainment through bed erosion.

Firstly, we consider particle laden dam-break flows with drag, an initial sediment load, particle deposition, and particle entrainment through the mechanism of bed erosion. We explore various parameter configurations to demonstrate the effect of the relative balance between deposition and erosion. Secondly, we consider particle laden dam-break flows with drag, particle deposition and particle entrainment through bed erosion but no initial sediment load.

Throughout our study we noted that the presence of a dilute suspension did not have a significant effect on the height or velocity profiles of the flows and the overall shape of these profiles for flows with particles were essentially the same as the analogous particle-free profiles. Generally, flows with particles where slightly faster compared to analogous particle-free flows, but only by a few percent at most. As such we have refrained from including plots of the height and velocity profiles for brevity, and have instead focused on the dynamics of the volume fraction of particles.

Initially laden, active sediment flows

In Figure 4.5 we have plotted volume fraction profiles of the numerical solutions to the full model equations (2.19) with basal drag, an initial sediment load, particle
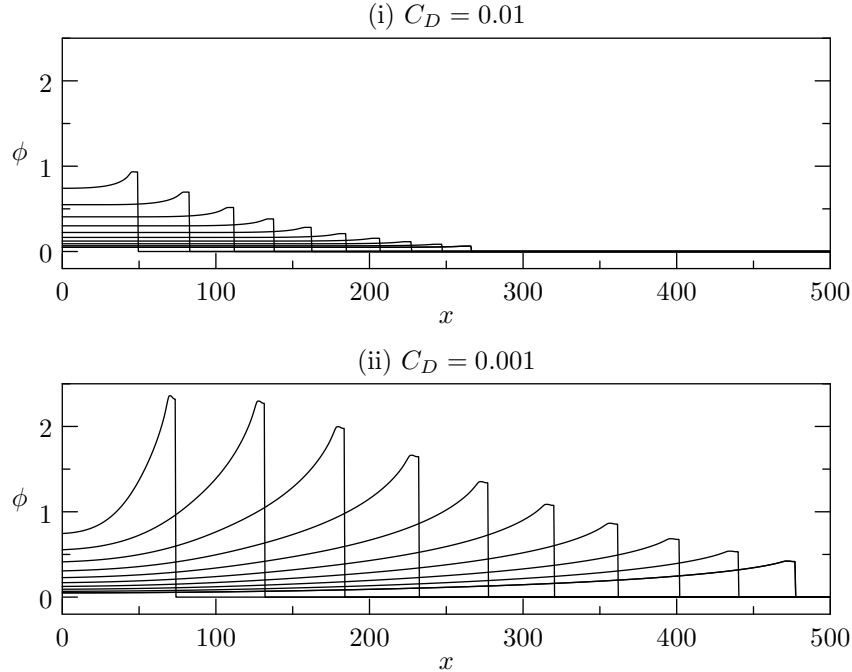
Figure 4.5: Volume fraction of a dam-break flow with basal drag, an initial sediment load ($\phi(x,0) = 1$), particle deposition, and bed erosion. Profiles show volume fraction at various times $t = 60, 120, \ldots, 540, 600$ with (i) $C_D = 0.01$ and (ii) $C_D = 0.001$. Other parameter values used are $\phi_0 = 0.01$, $\gamma = 2.5$, $u_d = 0.005$, $u_e = 0.0015$, $u_c = 0.5$, and $n = 2.0$.

deposition, and particle entrainment through bed erosion for two different values of the drag parameter C_D. In plot (i) the drag parameter $C_D = 0.01$ which is greater than in plot (ii), where $C_D = 0.001$. These plots highlight the importance of the drag parameter in determining the dynamics of the volume fraction of particles.

As demonstrated in Section 4.1.2, where we studied particle-free dam-break flows with basal drag, the presence of drag significantly retards the flow. The front speed of the numerical solution with drag is non-constant and decreases with time until the effect of drag balances the fluid's inertia. The maximum horizontal velocity occurs at the front, and the velocity is nearly uniform within the snout.

As the rate q_e at which bed sediment is entrained into the flow is an increasing function of the velocity u, the maximum rate of sediment entrainment occurs at the front and is nearly uniform within the snout. However, as the height of the fluid is non-constant within the snout and decreases sharply to zero at the front, the volume of fluid into which the sediment is entrained is non-constant within the snout, and decreases sharply to zero at the front. This results in the observed peaks of the volume fraction of sediment, as seen in both (i) and (ii).

Furthermore, increasing basal drag has the effect of slowing down the flow and hence reducing the rate of particle entrainment as the entrainment rate is an increasing function of the horizontal velocity. This can be seen by comparing plots (i) and (ii), in which we note that the volume fraction of sediment in the snout is higher in plot (ii) which has a smaller drag parameter than in (i).

Finally, we note that the peak particle entrainment is highest for short post-release times since the velocity is also highest for short post-release times, and decreases with time. As time increases the front speed decreases and hence the rate of entrainment also decreases, resulting in a decreasing volume fraction of sediment in the snout as particles settle out of suspension.

In Figure 4.6 we have plotted volume fraction profiles of the numerical solutions to the full model equations (2.19) with basal drag, an initial sediment load, particle deposition, and particle entrainment through bed erosion for two different values of the drag parameter C_D. In plot (i) the drag parameter $C_D = 0.01$ which is greater than in plot (ii), where $C_D = 0.001$. In Figure 4.6 the critical bed velocity u_c above which the bed is eroded and particles are entrained into the fluid is higher than in Figure 4.5. The profiles in Figure 4.6, when compared to the profiles in Figure 4.5, highlight the importance of the critical bed velocity in determining the dynamics of the volume fraction.

By increasing the critical bed velocity u_c above which the bed erodes and particles are entrained into the fluid we increase the cohesiveness of the bed and thereby decrease the ability with which the flow can erode the bed. As such, a higher bed shear, and hence velocity, is needed in order to erode the bed and entrain particles. If the basal drag is strong enough so that the flow is kept from reaching this critical bed velocity, then no particles will be entrained by the flow.

This interplay between the basal drag C_D and the critical bed velocity u_c is demonstrated by comparing plots (i) and (ii) in Figure 4.6. In plot (i) the drag parameter C_D is high enough so that the flow does not reach speeds much higher than the critical bed velocity, and hence the dynamics of the volume fraction are dominated by deposition, and the volume fraction remains nearly horizontal throughout the flow and decreases with time.

In Figure 4.7 we have plotted volume fraction profiles of the numerical solutions to the full model equations (2.19) with basal drag, an initial sediment load, particle deposition, and particle entrainment through bed erosion for $n = 1/2$, $n = 1$, and $n = 2$.
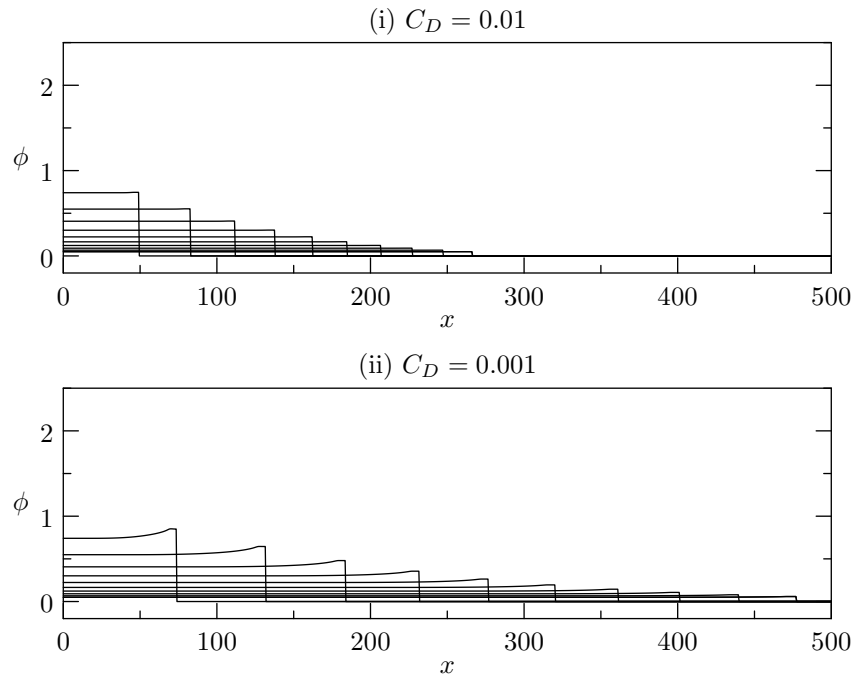
Figure 4.6: Volume fraction of a dam-break flow with basal drag, an initial sediment load ($\phi(x, 0) = 1$), particle deposition, and bed erosion. Profiles show volume fraction at various times $t = 60, 120, \ldots, 540, 600$ with (i) $C_D = 0.01$ and (ii) $C_D = 0.001$. Other parameter values used are $\phi_0 = 0.01$, $\gamma = 2.5$, $u_d = 0.005$, $u_e = 0.0015$, $u_c = 0.8$, and $n = 2.0$.
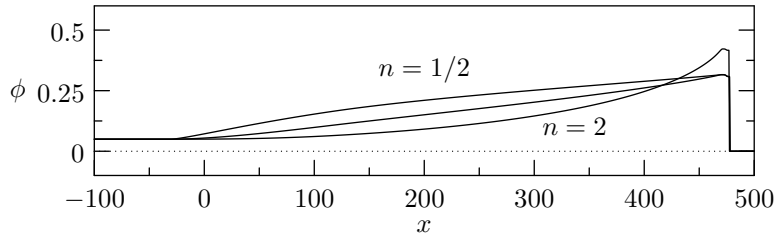
Figure 4.7: Volume fraction of a dam-break flow with basal drag, an initial sediment load, particle deposition, and bed erosion at $t = 600$. Above $x = 200$, the power $n = 1/2$ for the bottommost profile, $n = 1$ for the middle profile, and $n = 2$ for the topmost profile. Other parameter values used are $C_D = 0.001$, $\phi_0 = 0.01$, $\gamma = 2.5$, $\phi(x, 0) = 1$, $u_d = 0.005$, $u_e = 0.0015$, and $u_c = 0.5$.

We recall that the mass entrainment flux q_e is an increasing function of u, that the dimensionless exponent n determines the concavity of the $q_e(u)$ curves (which are concave up when $(2n-1)u^2/u_c^2 - 1 > 0$ and concave down when $(2n-1)u^2/u_c^2 - 1 < 0$ so that they are always concave up for $n \geq 1$) and that the $q_e(u)$ curves, for different n, intersect at $u = \sqrt{2}\,u_c$.

For $n < 1$ we note that the volume fraction of particles ϕ in Figure 4.7 is increasing and concave down, with relatively more particles per unit volume in suspension in the bulk of the flow than the snout. For $n > 1$ we note that the volume fraction of particles is increasing and concave up, with a peak at the front and relatively more particles per unit volume in suspension in the snout than in the bulk of the flow.

The dimensionless exponent n serves to differentiate between two types of flows; the first where the volume fraction in the bulk is relatively high and the volume fraction profiles do not have a peak at the front, and the second where the volume fraction in the snout is relatively high, and the volume fraction profiles have a peak at the front.

In Figure 4.8 we have plotted the particle flux $q_e - q_d$ at the station $x = 10$ for the numerical solution to the full model equations (2.19) with basal drag, particle deposition, and bed erosion for two different values of the drag parameter C_D. In plot (i) the drag parameter $C_D = 0.01$ which is greater than in plot (ii), where $C_D = 0.001$. In each plot, two curves are plotted for $u_c = 8/10$ ($> 2/3$) and $u_c = 5/10$ ($< 2/3$).

For $u_c = 0.5$ (topmost profile in both plots) the bed is eroded for short post-release times and particles are entrained into the snout. In (i), once the front has passed the flow does not continue to erode particles as the drag has slowed the

39

flow appreciably so that the velocity in the bulk of the fluid is less than the critical bed velocity u_c and the particle flux is dominated by deposition. In (ii), once the front has passed the flow continues to erode the bed and advect the entrained particles downstream. As time progresses, the horizontal velocity u at the station approaches its Ritter solution and q_e approaches a steady value. However, as q_d is linearly proportional to the volume fraction of particles, the flux $q_e - q_d$ decreases with time as ϕ increases.

For $u_c = 0.8$ (bottommost profile in both plots), once the front has passed, the net particle flux remains negative since the flow is not flowing fast enough to overcome the critical bed velocity u_c.

In all cases, eventually the net particle flux $q_e - q_d$ approaches zero, and two scenarios result depending on the speed of the flow which is influenced by the drag C_D, and the critical bed velocity u_c. For flows that are dominated by erosion, when the net particle flux reaches zero the flow will continue to erode the bed and entrain particles at the same rate that particles are deposited and the flow will remain laden with sediment. For flows that are dominated by deposition, when the net particle flux reaches zero the flow will no longer be laden with sediment as all particles will have been deposited since the flow is not strong enough to erode the bed as a result of either high bed cohesion, high basal drag, or both.

In Figure 4.9 we have plotted the net particle flux $q_e - q_d$ and horizontal velocity u at the station $x = 10$ for the numerical solution to the full model equations (2.19) with basal drag, particle deposition, and bed erosion. These plots elucidate the relationship between the horizontal velocity and the particle flux, and also show the velocity approaching its long term Ritter solution $u = 2/3$.

In (ii), the critical bed velocity $u_c = 0.5$ for the topmost profile which is less than the long term Ritter solution $u = 2/3$, and hence the particle flux is dominated by erosion and the flow will remain laden with sediment. The critical bed velocity $u_c = 0.8$ for the bottommost profile which is greater than the long term Ritter solution $u = 2/3$, and hence the resulting particle flux is eventually dominated by deposition so that all particles will eventually settle out of suspension.

Note that the time at which the particle flux profile corresponding to $u_c = 0.8$ in (ii) becomes dominated by deposition ($q_e - q_d \leq 0$) occurs before the velocity reaches the critical bed velocity u_c. That is, the bed continues to be eroded until u reaches u_c, but the particle entrainment rate q_e becomes less than the particle deposition rate q_d before the bed ceases to be eroded.

(i) $C_D = 0.01$

(ii) $C_D = 0.001$
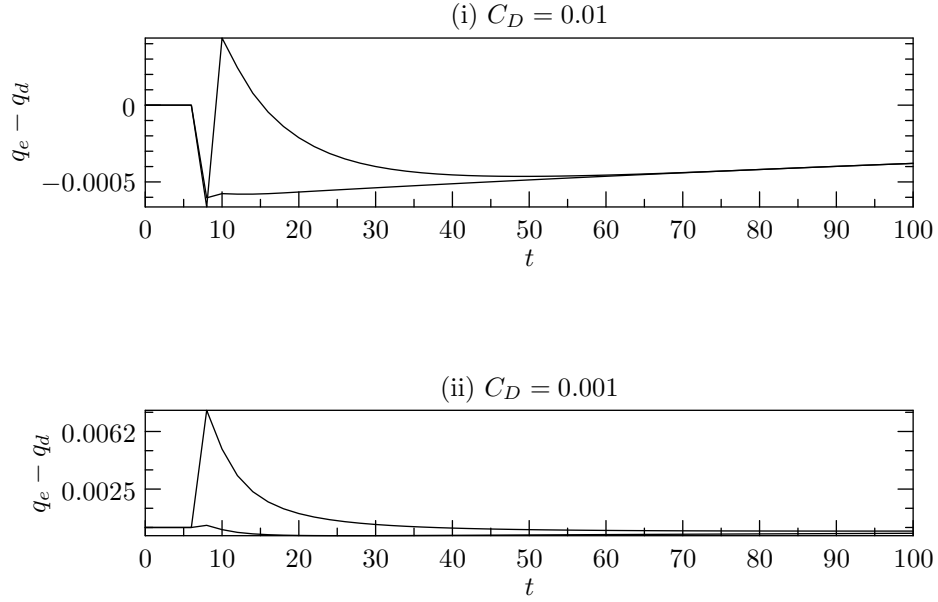
Figure 4.8: Source $(q_e - q_d)$ at $x = 10$ of the numerical solution with basal drag, an initial sediment load, particle deposition, and bed erosion. In each plot the critical bed velocity u_c is $= 0.8$ for the bottommost profile and 0.5 for the topmost profile. The drag parameter is (i) $C_D = 0.01$ and (ii) $C_D = 0.001$. Other parameter values used are $\phi_0 = 0.01$, $\gamma = 2.5$, $\phi(x, 0) = 1$, $u_d = 0.005$, $u_e = 0.0015$, and $n = 2$.

(i) u

(ii) $q_e - q_d$
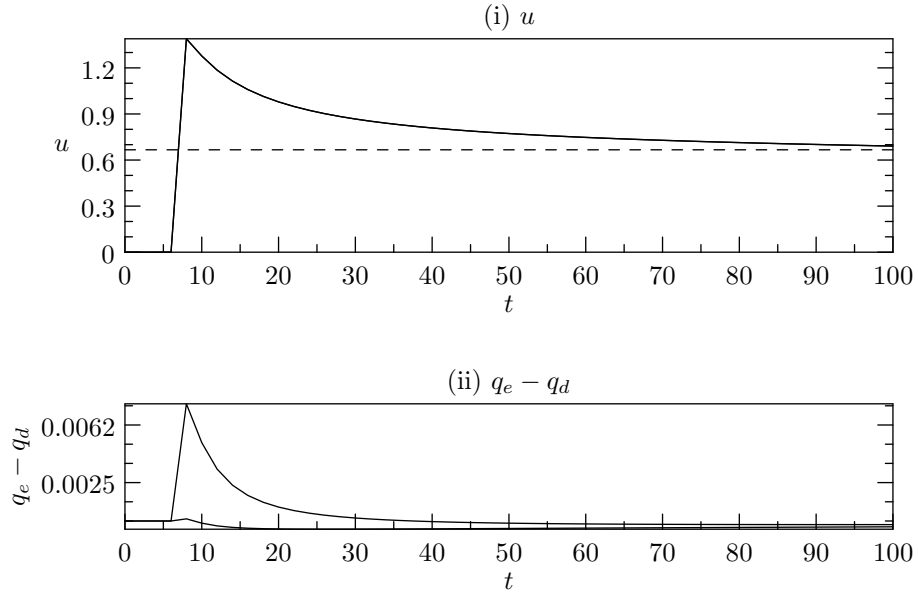
Figure 4.9: (i) Horizontal velocity u and (ii) net particle flux $q_e - q_d$ of the numerical solution with basal drag, an initial sediment load, particle deposition, and bed erosion. In (i), the dashed line shows the long term Ritter solution $u = 2/3$. In (i) the critical bed velocity u_c is $= 0.8$ for the bottommost profile and 0.5 for the topmost profile. Other parameter values used are $C_D = 0.001$, $\gamma = 2.5$, $\phi(x, 0) = 1$, $u_d = 0.005$, $u_e = 0.0015$, and $n = 2$.

41
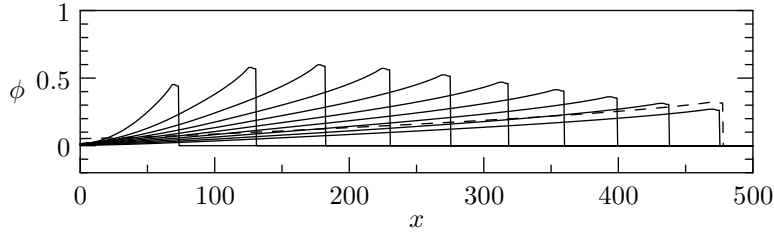
Figure 4.10: Volume fraction of a dam-break flow with basal drag, particle deposition, and bed erosion. Dashed line shows initially laden flow with $n = 1.2$ at $t = 600$, solid lines show initially clear flow with $n = 1.2$ at various times $t = 60, 120, \ldots, 540, 600$. Other parameter values used are $C_D = 0.001$, $\phi_0 = 0.01$, $\gamma = 2.5$, $u_d = 0.005$, $u_e = 0.0015$, and $u_c = 0.5$.

Initially clear, active sediment flows

In Figure 4.10 we have plotted the volume fraction profile of the numerical solution to the full model equations (2.19) with drag, particle deposition, bed erosion, but without an initial sediment load. Again, the volume fraction is highest in the snout of the flow where the height is small and entrainment is strongest. In contrast to Pritchard and Hogg [42] where the concentration in the snout grew until it reached its maximum and subsequently remained constant, we note that the volume fraction in the snout here grows until it attains a maximum and then decreases slowly. In the absence of drag the front speed is constant and particles are entrained into the snout until the effects of bed erosion and particle deposition reach an equilibrium. In the presence of drag the front speed is no longer constant – the velocity of the front is fastest initially when the effect of gravity is stronger than the effect of drag, resulting in strong erosion of the bed and an increasing volume fraction profile in the snout. When the effects of gravity and drag reach an equilibrium and the front speed becomes constant (and slower than the drag free case), the particle entrainment rate due to bed erosion is slower than the drag free case, and hence the balance between bed erosion and particle deposition occurs at a lower volume fraction.

In Figure 4.11 we have plotted the horizontal velocity u and volume fraction of sediment ϕ for the numerical solution to the full model equations (2.19) with basal drag, particle deposition, bed erosion, but without an initial sediment load. These plots elucidate the relationship between the velocity and volume fraction of sediment entrained by the flow.

The volume fraction is highest in the snout of the flow where the height is small and entrainment is strongest due to the high velocity of the flow there. The velocity

42
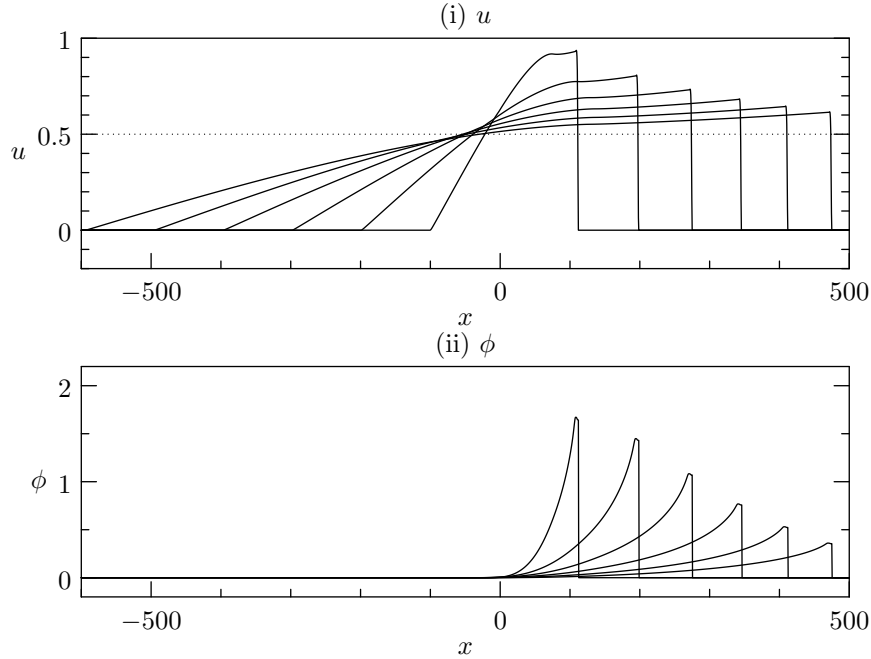
Figure 4.11: (i) Horizontal velocity u *vs* x and (ii) ϕ *vs* x at various times $t = 100, 200, 300, 400, 500, 600$ with no initial sediment load ($\phi(x, 0) = 0$). Dotted line in (i) shows the critical bed velocity u_c. Parameter values used are $C_D = 0.001$, $u_c = 0.5$, $\phi_0 = 0.01$, $\gamma = 2.5$, $u_d = 0.005$, $u_e = 0.0015$, and $n = 2$.

in the snout is highest for short post-release times and decreases with time as the effect of drag begins to balance the effect of gravity slowing the flow. As such, particle entrainment is highest for short post-release times and decreases with time. As the entrained particles settled out of suspension through the mechanism of deposition the volume fraction of sediment will decrease until an equilibrium between the rates of entrainment and deposition is reached. These result in the high volume fraction for short post-release times that decreases with time.

In Figure 4.12 we have plotted the particle flux $q_e - q_d$ at the station $x = 10$ for the numerical solution with drag, particle deposition, and bed erosion for $u_c = 8/10$, $u_c = 5/10$, and $u_c = 3/10$. We note that the long term behaviour of the particle flux is the same as the initially laden case, which is consistent with our analysis done to determine the critical bed velocity below which the flow will continue to erode the bed. At the onset the particle flux remains positive, in contrast to the initially laden case, since the deposition term q_d depends on the volume fraction ϕ which is zero initially, and will remain small until enough particles are entrained and a balance between particle entrainment and deposition is reached (if the critical bed velocity is low enough).

43
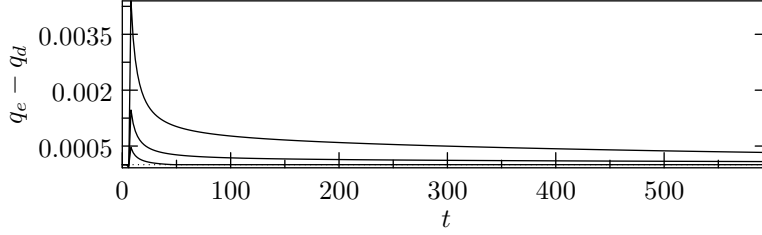
Figure 4.12: Source ($q_e - q_d$) of the numerical solution with basal drag, particle deposition, bed erosion, but no initial sediment load. The critical bed velocity is $u_c = 0.8$ for the bottommost profile, $u_c = 0.5$ for the middle profile, and $u_c = 0.3$ for the topmost profile. Other parameter values used are $C_D = 0.001$, $\phi_0 = 0.01$, $\gamma = 2.5$, $\phi(x,0) = 1$, $u_d = 0.005$, $u_e = 0.0015$, and $n = 1$.

4.1.4 Sustained erosion

In all of our numerical simulations we have observed that, away from the tip of the flow, the solutions for the height h and the horizontal velocity u of the particle laden current are quite similar to those provided by the Ritter solutions [45] for the particle-free model (with the gravity g replaced by the modified gravity $\widehat{g}$). In other words, after the front has passed, the height and horizontal velocity fields of a dilute particle laden flow are well approximated by

$$u = \frac{2}{3}\left(\frac{x}{t} + \sqrt{\widehat{g}h_0}\right) \quad \text{and} \quad \widehat{g}h = \frac{1}{9}\left(2\sqrt{\widehat{g}h_0} - \frac{x}{t}\right)^2. \qquad (4.2)$$

This observation is confirmed in Figure 4.13, in which we have plotted the depth and velocity profiles of both the Ritter solution and a typical numerical solution of equations (2.19) corresponding to the initial value problem for the dam-break flow. We note that the numerical solutions with drag and active sediment are well approximated by the Ritter solution for $\xi = x/t < 0.1$.

Focusing our attention on a fixed station at $x = a$ for some a, we note that after a sufficiently long time the front of the flow will have passed the station and the height and horizontal velocity fields will approach their Ritter solutions given in (4.2) provided the drag coefficient is small enough so that the bulk is not significantly retarded by the drag. That is, as $t \to \infty$,

$$u \to \frac{2}{3}\sqrt{\widehat{g}h_0} \quad \text{and} \quad \widehat{g}h \to \frac{4}{9}\widehat{g}h_0. \qquad (4.3)$$

Employing the long-term Ritter solutions (4.3) in the deposition and erosion mod-
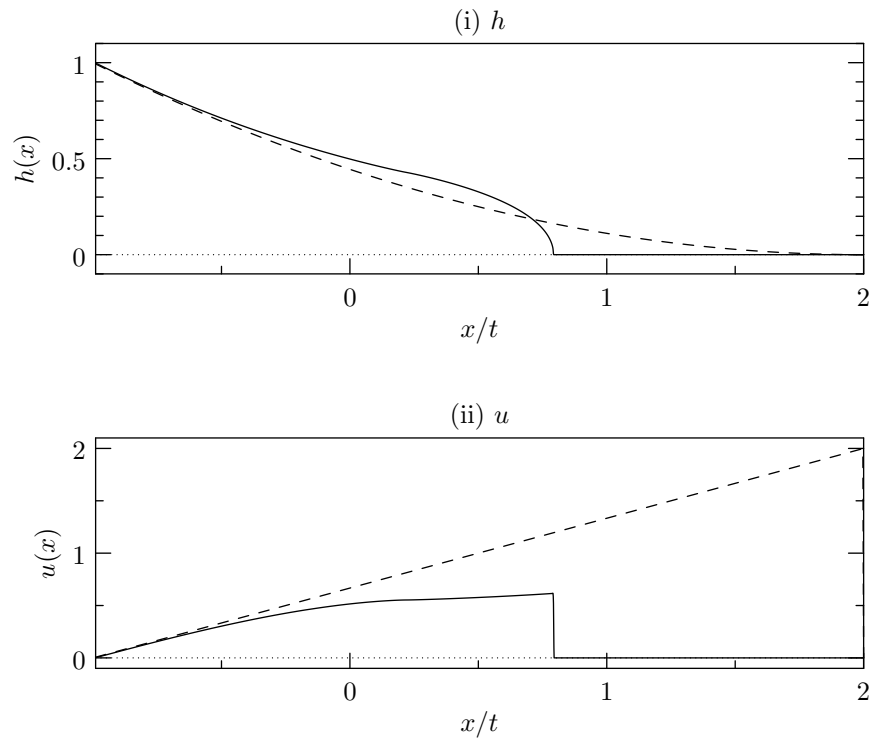
Figure 4.13: (i) Height and (ii) horizontal velocity *vs* x/t at $t = 600$. Solid lines are numerical solutions, dashed lines are Ritter solutions. Parameter values used are $C_D = 0.001$, $\phi_0 = 0.01$, $\gamma = 2.5$, $\phi(x, 0) = 1$, $u_d = 0.005$, $u_e = 0.0015$, $u_c = 1.0$, and $n = 1$.

els (2.24) and (2.26), we obtain two cases. If

$$\frac{2}{3}\sqrt{\widehat{g}h_0} < u_c \qquad (4.4)$$

then the flow is not sufficiently strong enough to erode the bed at the station $x = a$, and eventually all particles will settle out of suspension. On the other hand, if the critical bed velocity u_c is small enough so that the flow continues to erode the bed at the station, then the deposition and erosion fluxes will balance when $q_e = q_d$, that is

$$\rho_p v_e \left(\frac{4}{9} \frac{\widehat{g}h_0}{u_c^2} - 1 \right)^n = \rho_p v_s \phi. \qquad (4.5)$$

This determines a critical volume fraction ϕ_c, below which erosion is stronger than deposition so that the volume fraction increases, and above which deposition is stronger than erosion so that the volume fraction decreases. Isolating ϕ_c, we obtain

$$\phi_c = \frac{v_e}{v_s} \left(\frac{4}{9} \frac{\widehat{g}h_0}{u_c^2} - 1 \right)^n \qquad (4.6)$$

which, in terms of our non-dimensional variables, becomes

$$\phi_c = \frac{u_e}{u_d} \left(\frac{4}{9} \frac{1}{u_c^2} - 1 \right)^n. \qquad (4.7)$$

The non-dimensional critical bed velocity below which the flow will continue to erode the bed is $u_c \leq \frac{2}{3}$.

4.2   Modified ($\beta > 1$) dam-break flows

4.2.1   Particle-free, without drag, flat bed

We consider particle-free dam-break flows for which there is shear in the vertical profiles of the velocity so that the shape factor $\beta > 1$. In general the shape factor β is a function of the height and velocity of the flow so that $\beta \equiv \beta(u, h)$.

For modified dam-break flows without basal drag ($\beta > 1$, $C_D \equiv 0$) it is no longer possible to locate the front of the flow unless $\beta \to 1$ at the front [26]. This can be seen by considering the characteristic form of the governing equations (2.20) without basal friction ($C_D \equiv 0$) or bottom slope ($b \equiv 0$). Following Hogg and Pritchard [26] we consider a linear combination of (2.20) , with $C_D \equiv b \equiv 0$, which

results in the characteristic equation

$$\frac{\mathrm{d}h}{\mathrm{d}t} + \gamma_\pm \frac{\mathrm{d}u}{\mathrm{d}t} = 0 \quad \text{on} \quad \frac{\mathrm{d}x}{\mathrm{d}t} = c_\pm \tag{4.8}$$

to obtain

$$c_\pm = \beta u + \frac{u^2}{2}\frac{\partial \beta}{\partial u} \pm \sqrt{u^2 \beta(\beta - 1) + h + u^3 \frac{\partial \beta}{\partial u}\left(\beta - 1 + \frac{u}{4}\frac{\partial \beta}{\partial u}\right) + u^2 h \frac{\partial \beta}{\partial h}} \tag{4.9}$$

and

$$\gamma_\pm = \frac{h(c_\pm - u)}{u^2(\beta - 1) + h + u^2 h \frac{\partial \beta}{\partial h}}. \tag{4.10}$$

Since β remains bounded as $h \to 0$ we note that the expression under the square-root in (4.9) is greater in magnitude than $\frac{u^4}{4}(\frac{\partial \beta}{\partial u})^2$ so that $c_+ \geq \beta u > u$ for $\beta > 1$. That is, if β exceeds unity at the front, then the characteristic velocity exceeds the front velocity and it is no longer possible to impose a kinematic condition there.

To illustrate, we consider the case where β is constant. Following Hogg and Pritchard [26], equation (4.8) is rewritten as

$$\frac{\mathrm{d}h}{\mathrm{d}u} = -\frac{h\left((\beta - 1)u + \sqrt{u^2 \beta(\beta - 1) + h}\right)}{u^2(\beta - 1) + h}. \tag{4.11}$$

and subsequently integrated to obtain an implicit solution for the height and velocity fields

$$1 = h^{3(\beta-1)}\left[\sqrt{h + \beta(\beta - 1)u^2} + \frac{(3 - 2\beta)}{2}u\right]^{2\beta-3}$$
$$\cdot \left[\frac{\sqrt{h + \beta(\beta - 1)u^2} + u\sqrt{\beta(\beta - 1)}}{\sqrt{h + \beta(\beta - 1)u^2} - u\sqrt{\beta(\beta - 1)}}\right]^{\sqrt{\beta(\beta-1)}} \tag{4.12}$$

for $\beta > 1$ and $\beta \neq 9/8$; and

$$1 = \frac{1}{8}\exp\left(\frac{2u}{\sqrt{64h + 9u^2} + 3u}\right)$$
$$\cdot \left(\sqrt{64h + 9u^2} + 3u\right)^{5/6}\left(\sqrt{64h + 9u^2} - 3u\right)^{1/6} \tag{4.13}$$

for $\beta = 9/8$; together with the expansion fan originating at $x = 0$ and $t = 0$ such that

$$\frac{x}{t} = \beta u - \sqrt{h + \beta(\beta - 1)u^2}. \tag{4.14}$$

From (4.12) we note that $h \to 0$ only as $u \to \infty$, which is a manifestation of

47
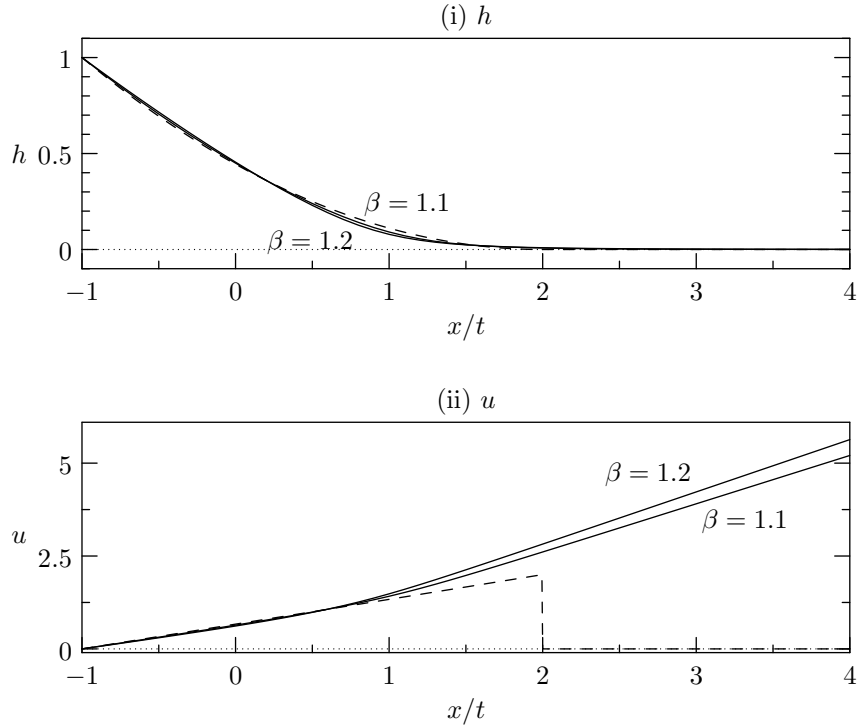
Figure 4.14: (i) Height and (ii) velocity profiles for a modified dam-break flow over a level stable bed without basal drag and with $\beta = 1.0, 1.1$, and 1.2. Solid lines indicate solutions with $\beta \neq 1$, dashed line indicates solution with $\beta = 1.0$.

the observation above that the characteristic velocity at the front is greater than the front velocity. That is, in the absence of drag, it is not possible to locate the position of the front for $\beta > 1$.

From (4.14) we note that when $u = 0$ and $h = 1$, $x/t = -1$, so the speed at which the expansion fan propagates into the reservoir is constant and independent of β, which is to be expected as the reservoir is at rest and has no momentum.

In Figure 4.14 we have plotted the solution for the height and velocity profiles for various values of the shape parameter β. From plot (ii) we see that $u \to \infty$ as $x/t \to \infty$ while $h \to 0$ in (i) as expected. We also note that for $\beta > 1$ the most significant departures from the Ritter solutions occur in regions where h is small and u is greater than unity.

In Figure 4.15 we have plotted the height and velocity profiles for both the classic solution [45] and the numerical solution of the pure initial value problem based on (2.20) including basal drag with $\beta > 1$. We note that the effect of vertical shear ($\beta > 1$) in the horizontal velocity profile is most dramatic in the immediate vicinity of the leading edge where the depth, and hence momentum, of the flow is small
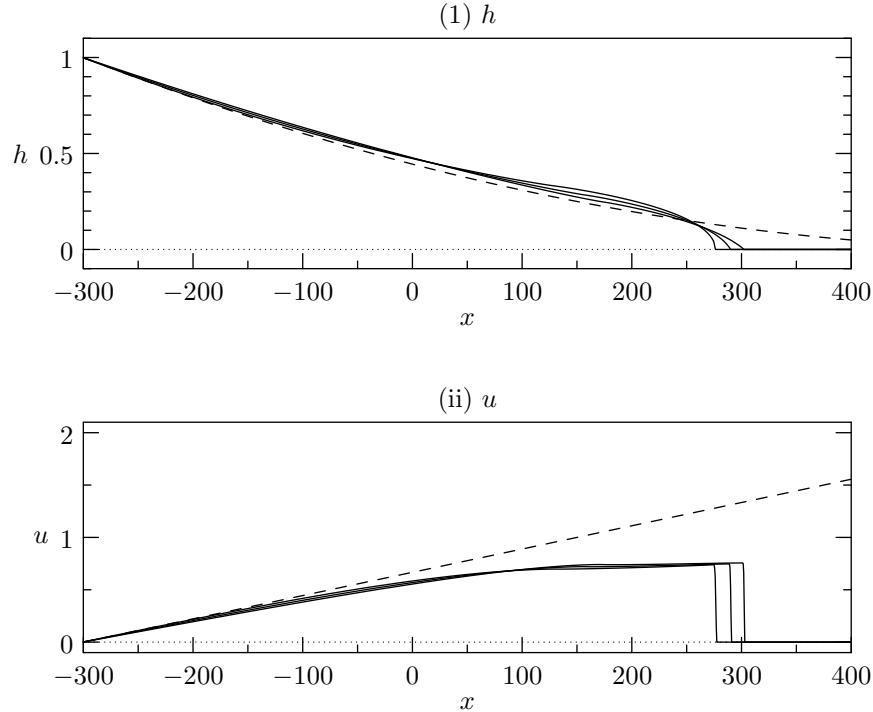
Figure 4.15: (i) Height and (ii) velocity profiles of the particle-free modified dam-break flow over a flat bottom with basal drag at $t = 300$. Solid lines show numerical solutions with $\beta = 1.0, 1.1,$ and 1.2 from left to right. Dashed line shows the Ritter solution. Parameter value used is $C_D = 0.001$.

allowing the effect of vertical shear in the horizontal velocity to be accentuated. The shape of the tip in the absence of shear is blunt and falls to zero abruptly at the front so that the surface of the flow intersects the bed perpendicularly. The introduction of vertical shear alters this profile so that the surface of the flow no longer intersects the bed at an oblique angle. Furthermore, the front position for $\beta > 1$ is greater than in the case where $\beta = 1$ due to the reduced angle of intersection between the surface of the flow and the bed, and the incompressibility of the fluid.

4.2.2 Particle-free, with drag, sloping bed

In this subsection we will examine modified dam-break flows over sloping beds in order to isolate the effects of the interplay between the bottom slope and basal drag. This involves solving the initial value problem consisting of (2.20) together with the initial conditions of equation (2.21). We shall take the bottom topography to be specified by (3.1).

49
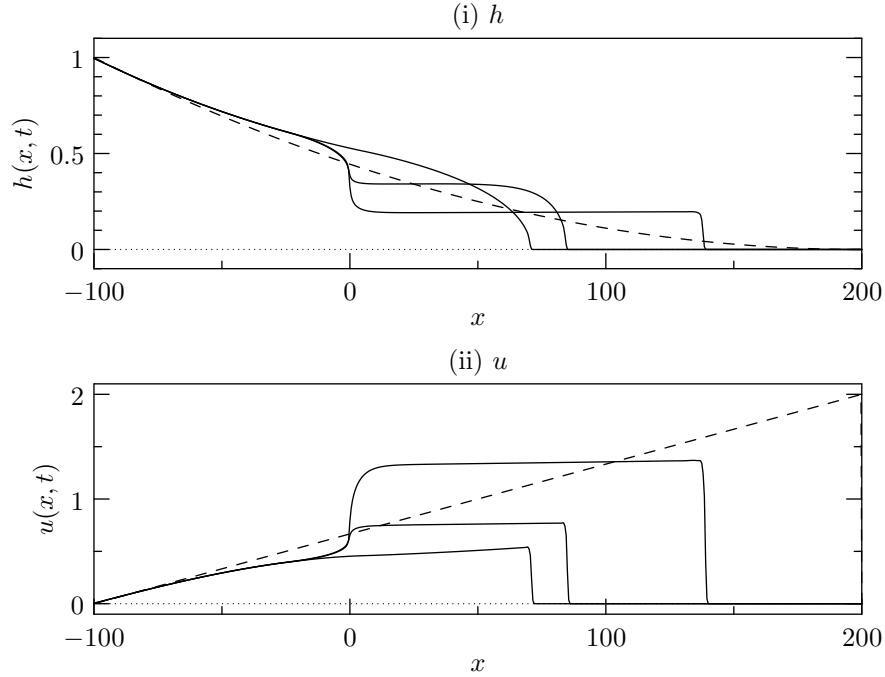
Figure 4.16: (i) Height and (ii) horizontal velocity for a particle-free dam-break flow over a linear slope with drag. Solid lines show numerical solutions with slope $s = 0, 0.001$, and 0.01 from left to right. Dashed lines show the Ritter solutions. Parameter values used are $C_D = 0.01$ and $\beta = 1$.

In Figure 4.16 we have plotted the numerical solutions for both the height and velocity profiles of a particle-free dam-break flow over a sloping bottom with drag for $\beta = 1$. We note that both the height and velocity profiles are nearly horizontal in the bulk of the flow over the linearly sloping bed. Furthermore, in the presence of a sloping bottom the blunt snout in the height profile has become more abrupt and falls steeply to zero at the front. As demonstrated in previous sections, the effect of drag is to retard the front and create a blunt snout, while the effect of a sloping bottom is to draw out the fluid, reducing its height in the bulk of the flow over the sloping bed, and slightly increasing its height directly behind the front. The interplay between these two effects results in the profiles shown in Figure 4.16.

We also note that, in contrast to the drag-free case, the presence of a sloping bottom has a significant effect on the front position of the flow. As one may expect, the front position is greater for flows over steeper beds.

In Figure 4.17 we have plotted the numerical solutions for both the height and velocity profiles of a particle-free dam-break flow over a sloping bottom with drag for $\beta > 1$. The effect of vertical shear in the horizontal velocity here is similar to its effect in the absence of a sloping bottom. The angle at which the surface of

50
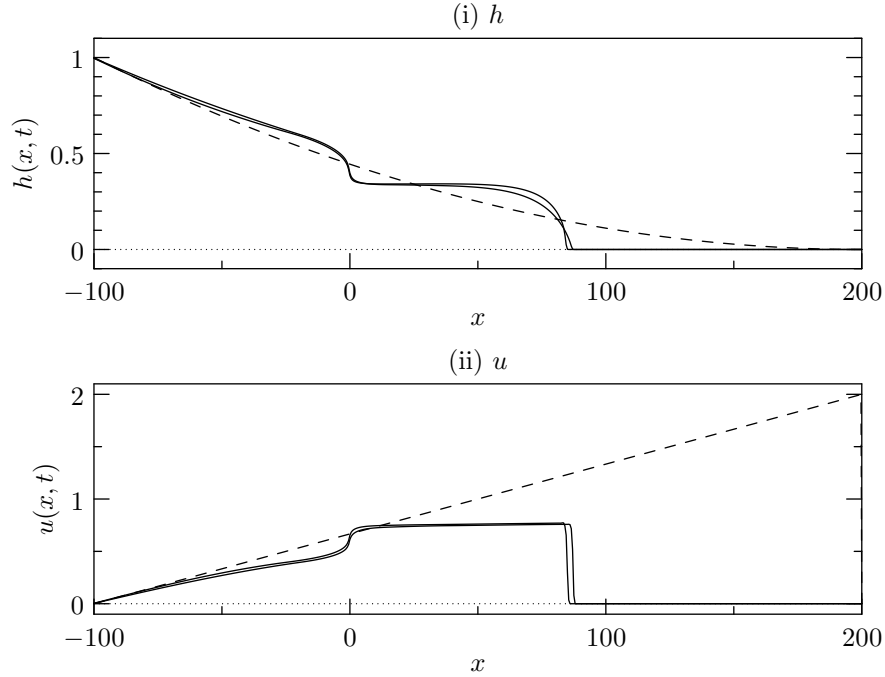
Figure 4.17: (i) Height and (ii) horizontal velocity for a particle-free dam-break flow over a linear slope with drag. Solid lines show numerical solutions with $\beta = 1.0, 1.1$ and 1.2 from left to right. Dashed lines show the Ritter solutions. Parameter values used are $C_D = 0.01$ and $s = 0.001$.

the flow intersects the bed is no longer oblique, and the front position for $\beta > 1$ is slightly greater than for $\beta = 1$.

4.2.3 Particle-laden, with drag, linear slope

In this subsection we will explore the complex interactions between particles and flow when basal drag, bottom topography, erosion, and sedimentation are taken into account. We will solve the full particle-laden model equations in the presence of drag and a sloping bed. These flows are representative of flows with sufficiently low aspect ratio whose dynamics are governed by the balance between the fluid's inertia, the horizontal pressure gradient, basal drag, bottom topography, and the presence of a changing particle volume fraction or concentration through the mechanisms of particle advection, deposition, and entrainment through bed erosion.

In Figure 4.18 we have plotted the horizontal velocity u and volume fraction of sediment ϕ for the numerical solution to the full model equations with basal drag, particle deposition, bed erosion, and bed slope. These plots elucidate the relationship between the velocity and volume fraction of sediment entrained by the
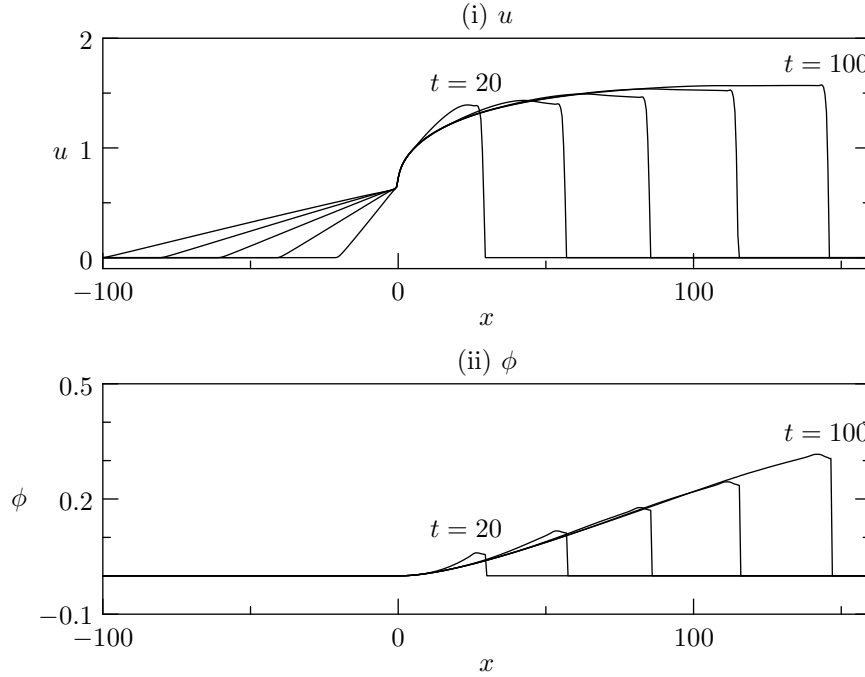
Figure 4.18: Volume fraction of a dam-break flow with basal drag, particle deposition, and bed erosion at various times $t = 20, 40, \ldots, 80, 100$. Parameter values used are $C_D = 0.001$, $\phi_0 = 0.01$, $\gamma = 2.5$, $u_d = 0.005$, $u_e = 0.0015$, $n = 1.2$, $u_c = 0.5$, $\beta = 1$, and $s = 0.001$.

flow.

Since the velocity over the sloping region is nearly horizontal and particles are advected downstream with the same velocity as the flow, particles entrained into the flow maintain their relative position within the flow. As such, particles entrained into the flow directly behind the front are advected downstream with the flow and remain in a position directly behind the front resulting in the volume fraction profile shown in Figure 4.18 which attains its maximum directly behind the front.

The linear nature of the volume fraction profile shown in Figure 4.18 is in contrast to the flat case [19] in which the volume fraction was highest in the snout and decayed in a non-linear fashion in the upstream direction. Furthermore, the physical mechanisms that determine the observed volume fraction profiles in the flat and sloping cases are different. In the flat case, the peak in the volume fraction profile was due to the nature of the height and velocity profiles: the volume fraction was highest in the snout of the flow where the height was small and entrainment was strongest due to the high velocity of the flow there. The velocity in the snout was highest for short post-release times and decreased with time as the effect of drag

began to balance the effect of gravity slowing the flow. As such, particle entrainment was highest for short post-release times and decreased with time. As the entrained particles settled out of suspension through the mechanism of deposition the volume fraction of sediment decreased until an equilibrium between the rates of entrainment and deposition was reached. These effects resulted in a high volume fraction for short post-release times that decreased with time. In the sloping case, for sufficiently large slopes, the peak in the volume fraction is primarily due to advection coupled with the nearly horizontal velocity profile, and the peak increases for all post-release times [5].

4.3   Varying bed topography

4.3.1   Passage through the critical Froude number

In this section we present a brief review of some of the results of [31] which pertain to surface waves excited by small amplitude bed disturbances when the Froude number of the flow is close to unity. We do so in order to motivate an essential conclusion of their analysis: when the Froude number of a flow with a slowly varying bottom topography passes through unity, surface disturbances are excited by the bottom topography and amplify to form an N-wave of slowly increasing wavelength.

For an arbitrary isolated bottom disturbance of order $\epsilon \ll 1$ that moves upstream with dimensionless speed F (the Froude number), [31] extend [53] to obtain Boussinesq equations for shallow-water flows that incorporate high order terms related to small disturbances in the height and bed profiles. These equations are given by

$$\frac{\partial}{\partial t}h + \frac{\partial}{\partial x}(uh) = O(\nu^4), \quad \text{and} \tag{4.15a}$$

$$\frac{\partial}{\partial t}u + u\frac{\partial}{\partial x}u + \frac{\partial}{\partial x}(h + \epsilon b) = -\frac{1}{3}\delta^2 h_{xtt} - \frac{1}{2}\delta^2 \epsilon b_{xtt} + O(\nu^3) \tag{4.15b}$$

where δ is the aspect ratio of the flow and ν is the (small) amplitude of free surface waves. For a slowly varying Froude number $F = F(\epsilon t)$ and bottom disturbance of the form

$$b(x,t) = B(x + t^+) \quad \text{where} \quad t^+ = \int_0^t F(\epsilon\tau)\, d\tau, \tag{4.16}$$

equation (4.15b) becomes

$$
\frac{\partial}{\partial t}u + u\frac{\partial}{\partial x}u + \frac{\partial}{\partial x}(h + \epsilon B)
$$
$$
= \epsilon F_t - \frac{1}{3}\delta^2\left(F^2 h_{xxx} + 2F h_{xxt} + h_{xtt}\right) - \delta^2\left(\frac{1}{2}F^2 B_{xxx} + \frac{1}{3}F_t h_{xx}\right) + O(\nu^3)
$$
(4.17)

in a coordinate system fixed to the moving bed (that is, the actual depth-averaged horizontal velocity of the flow is given by $u(x,t) - F(\epsilon t)$). Although [31] explore various scenarios arising from different forms of the Froude number function $F(\epsilon t)$, we will focus our attention here on the case where the Froude number is constant and close to unity. As in [31], the system (4.15) is re-scaled according to

$$
F - 1 = \epsilon^{1/2}F^*, \quad \nu = \epsilon^{1/2}, \quad \delta = \epsilon^{1/4}\kappa^*, \quad \text{and} \quad t^* = \epsilon^{1/2}t \tag{4.18}
$$

where κ^* measures the relative importance of dispersive and nonlinear effects (when $\kappa^* = 0$, nonlinear effects predominate); and multiple-scale expansions for u and h of the form

$$
u = 1 + \epsilon^{1/2}\left(F^* + u_1^*(x,t,t^*;F^*,\kappa^*)\right) + O(\epsilon) \tag{4.19a}
$$

$$
h = 1 + \epsilon^{1/2}\left(h_1^*(x,t,t^*;F^*,\kappa^*)\right) + O(\epsilon) \tag{4.19b}
$$

are employed. Substituting the expansions (4.19) into (4.15a) and (4.17), [31] find that u and h are given by

$$
u(x,t;\epsilon,F,\kappa) = 1 + \epsilon^{1/2}\left(F^* - \frac{1}{2}g(x,t^*;F^*,\kappa^*)\right) + O(\epsilon), \tag{4.20a}
$$

$$
h(x,t;\epsilon,F,\kappa) = 1 + \frac{1}{2}\epsilon^{1/2}g(x,t^*;F^*,\kappa^*) + O(\epsilon) \tag{4.20b}
$$

where g satisfies the evolution equation

$$
\frac{\partial}{\partial t}g + \left(F^* - \frac{3}{4}g\right)\frac{\partial}{\partial x}g - \frac{1}{6}\kappa^{*2}\frac{\partial^3}{\partial x^3}g = B_x. \tag{4.21}
$$

This is a forced Korteweg-de Vries (KdV) equation which has been explored, analytically and numerically, by several authors ([31, 12, 24]) and compared to experiment by [33]. In Figure 4.19 we have plotted the numerical solution to (4.21) which shows: (i) a region just downstream of the bump in which the height and velocity profiles are slightly depressed (the magenta region); (ii) the formation of small amplitude waves just downstream of this region (the green–magenta waves); and (iii) the periodic creation of slightly larger amplitude solitary waves that travel

54
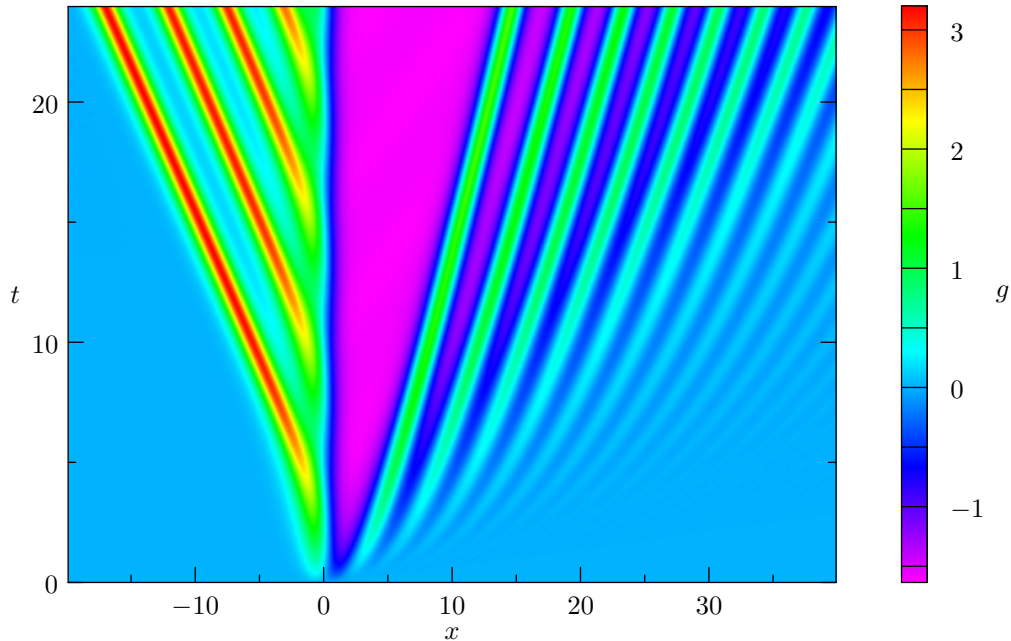
Figure 4.19: Solution $g(x, t)$ of the forced KdV equation (4.21). Parameter values used are $F^* = 0$ (ie, $F = 1$), $\kappa^* = 1.0$, $B(x) = \epsilon e^{-x^2/2}$, and $\epsilon = 0.01$. The solution was obtained using a simple finite-difference scheme as in [31] (see Appendix B).

upstream (the red–cyan waves).

[31] go on to demonstrate that the upstream travelling waves in Figure 4.19 decelerate as the Froude number increases through unity and eventually reverse direction to interact with the bottom disturbance. As the Froude number increases beyond unity this interaction gives rise to an N-wave with a slowly increasing wavelength above the bottom disturbance.

We have observed the formation of surface N-waves in the current study for certain combinations of parameters that result in both: (i) the formation of small bed disturbances through erosion, and (ii) flows in which the Froude number is close to unity. We believe the N-waves that we have observed are due to small bed disturbances and evolve in the manner described by, in particular, [31] because: (i) we do not witness them when erosion and deposition are suppressed (but all other parameters are the same), (ii) only witness them when the Froude number of the flow is unity, and (iii) the resulting bed disturbances travel slowly upstream as required in (4.16). In other words, the setting under which we observe N-waves in our simulations is exactly the same as in [31]. These flows will be explored in more detail in Section 4.3.6.

4.3.2 Predicting the Froude number of a dam-break flow prior to release

In the preceding section we demonstrated that surface N-waves may be formed above bottom disturbances when the Froude number of the flow passes through unity. In this section we demonstrate that, in certain parameter regimes, the Froude number of a dam-break flow can be predicted prior to release, and therefore we can predict when surface N-waves will be formed.

If the initial bed profile is given by

$$b(x,0) = s\,x\,\Theta(x) + O(\epsilon) \tag{4.22}$$

where Θ is the Heaviside step function and s is the gross bed slope, then the momentum source due to bottom topography in the absence of particles becomes roughly $\rho_f\,s\,g\,h$ for $x > 0$. When this balances the momentum source due to basal drag, which is $\rho_f\,C_D u^2$ in magnitude, we obtain $C_D u^2 \sim sgh$. Therefore, since the Froude number of a shallow-water flow is given by $F = u/\sqrt{gh}$, we obtain

$$F = \frac{u}{\sqrt{gh}} = \sqrt{\frac{s}{C_D}}. \tag{4.23}$$

In Figure 4.20 we have plotted the Froude number $F = u/\sqrt{h}$ for several particle-free dam-break flows with various different values of the drag (C_D) and slope (s) parameters in order to demonstrate that the Froude number of the flow does in fact attain its predicted value. We note that for steeper slopes, the Froude number attains its predicted value throughout a significant portion of the flow downstream of the initial location of the dam. For shallower slopes, although the the Froude number does not follow its predicted value as closely as for steeper slopes, it does remain close. Ultimately the regimes in which the Froude number can be predicted according to (4.23) are determined by the balance of the momentum source terms: if the slope is too shallow the flow will primarily be driven by the balance between the hydrostatic pressure gradient and drag instead of by the balance between the gross bed slope and drag.

When the bed topography is allowed to change with time through the mechanisms of deposition and erosion small deformations of the bed may be formed. If the Froude number of the flow is close to unity then these deformations may excite surface N-waves as was demonstrated in Section 4.3.1. As such, if we choose
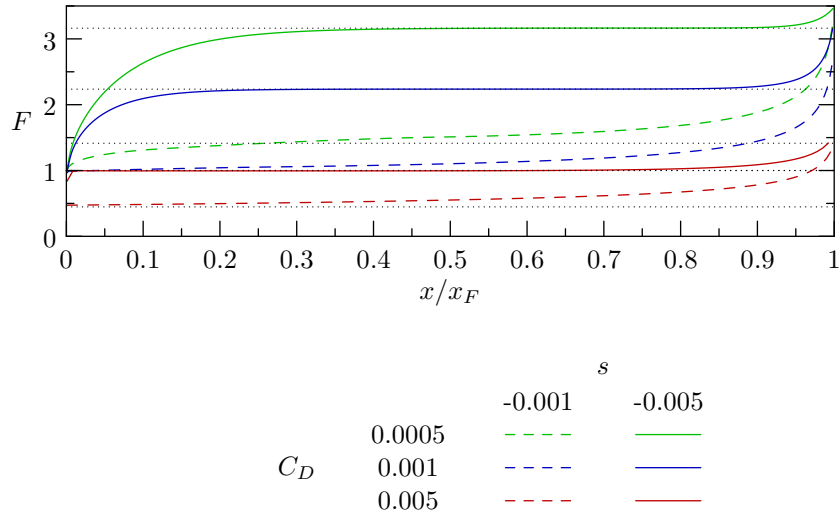
Figure 4.20: Froude number F $(= u/\sqrt{h})$ at $t = 3000.0$ for particle-free dam-break flows with various values of the drag (C_D) and bed slope (s) parameters. The x coordinate has been normalised by x_F, which is the first x coordinate at which the Froude number attains its maximum or 3.5. That is, $x_F = \min\{x \,|\, F(x) = \min(3.5, \max F)\}$. The dotted horizontal lines are the predicted Froude numbers (ie, $F = \sqrt{-s/C_D}$) for each flow. Other parameter values used are $\beta = 1$.

parameter values such that the predicted Froude number given by (4.23) equals unity, then surface N-waves are likely to be observed.

4.3.3 Flat bed

In Figure 4.21 we have plotted the height $h(x,t)$ and bed elevation $b(x,t)$ for an initially flat bed. These plots show the development of a scour pit at the original position of the dam. We note that the pit is deepest slightly downstream from the dam and that most of the sediment from the pit has been deposited downstream of the pit. We also note a slight thickening of the height profile above the pit as faster flowing fluid moving down and into the pit flows into slower moving fluid flowing up and out of the pit (as is the case for a hydraulic jump).

The height profile of the flow in Figure 4.21 resembles the height profile of a particle-free dam-break flow over a flat bed with drag ([26, 19]) except for the thickening of the fluid depth above the scour pit. That is, the tail position recedes into the reservoir at the speed $\sqrt{gh_0}$ and the height profile decreases quadratically from the tail position before thickening into a blunt snout and falling abruptly to zero at the front. As we have observed in the previous sections, the presence of dilute sediment in suspension does not have a significant affect on the flow
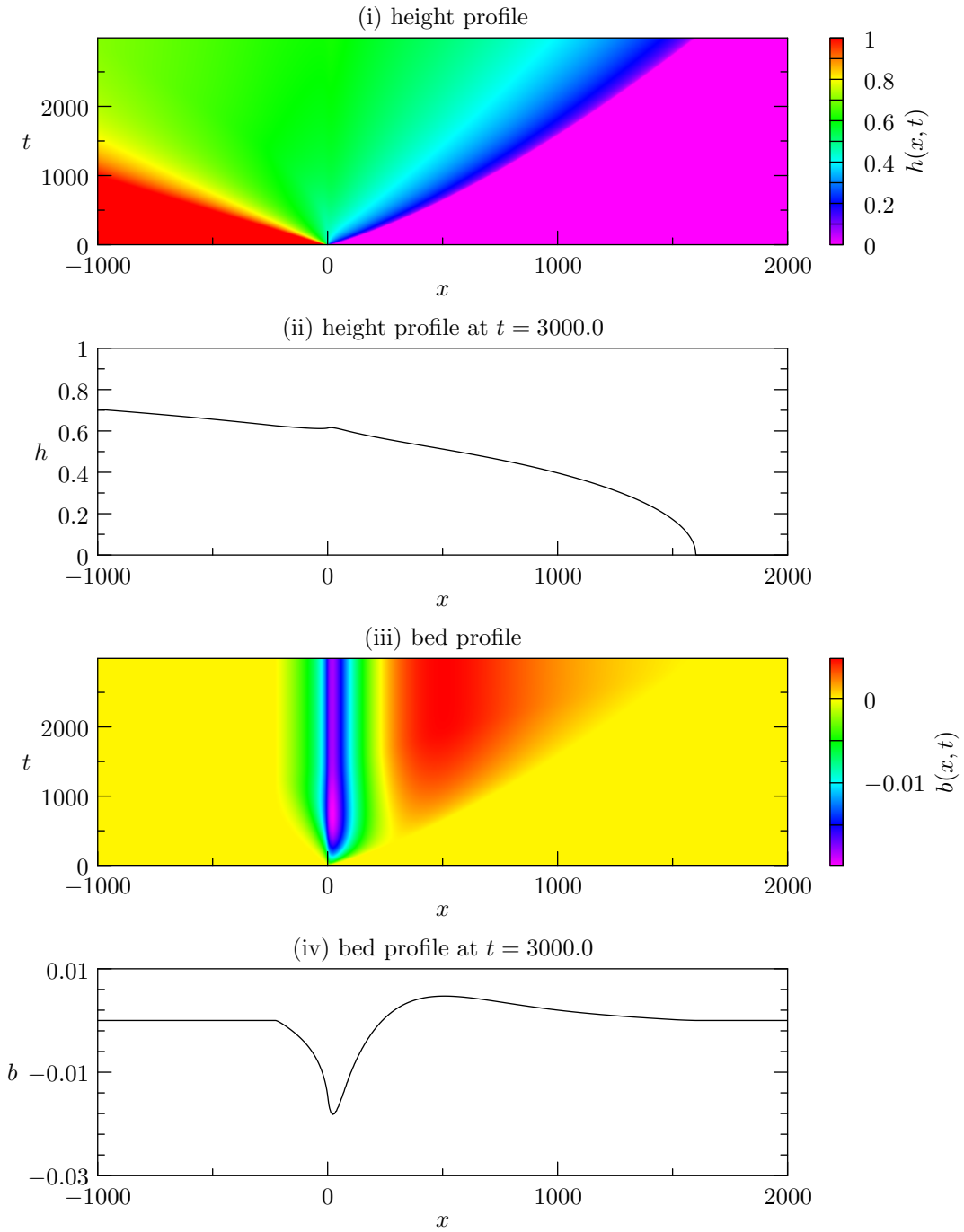
Figure 4.21: Height and bed elevation for an initially flat bed. Parameter values used were $C_D = 0.001$, $\phi_0 = 0.01$, $\gamma = 2.5$, $u_d = 0.005$, $u_e = 0.003$, $n = 1.0$, $u_c = 0.4$, $s = 0.0$, and $\beta = 1.0$.

dynamics: only a few percent at most. However, the effects of deposition and erosion do have a dramatic effect on the bed.

4.3.4 Sloping bed

In Figure 4.22 we have plotted the height $h(x, t)$ and bed elevation $b(x, t)$ for an initially sloping bed. These plots show the development of a scour pit at the original position of the dam as was the case in the previous section for a flat bed. However, no sediment has been deposited downstream of the pit (it remains in suspension) since the fluid is accelerated by the sloping bed augmenting the effect of erosion there. We also note that the height profile drops abruptly at the original position of the dam and that the height profile is constant downstream of the dam until it falls to zero at the front. This resembles the height profile of a particle-free dam-break flow over a linearly sloping bed with drag ([20]). That is, the flow upstream of the dam does not feel the effect of the sloping bed but the height profile drops abruptly at the dam and the fluid downstream of the dam is drawn out so that it has an almost constant depth until falling to zero at the front.

4.3.5 Momentum source balance

In Section 4.3.2 we demonstrated that the Froude number of a dam-break flow can be predicted prior to release in certain parameter regimes. In this subsection we will further analyse the magnitude of the various source terms in the momentum equation (2.31b) in order to gain further insight into which physical phenomena ultimately determine the evolution of a dam-break flow. Recall that the source terms of the momentum equation are: (i) pressure gradient $(-\frac{\partial}{\partial x}\Gamma(\phi)gh^2/2)$, (ii) drag $(-C_D u^2)$, (iii) bed topography $(-h\Gamma(\phi)\frac{\partial}{\partial x}b)$, and (iv) particle momentum exchange $(-\phi_0(\gamma + 1)u(q_e - q_d))$.

In Figure 4.23 we have plotted various source terms in the horizontal momentum equation for an initially flat bed and an initially sloping bed. For the initially flat bed, we note that in the tail of the fluid the flow is driven primarily by the pressure gradient (the height profile is roughly quadratic there) and slightly prohibited by drag. Behind the front the pressure is balanced by drag and the net momentum source is zero. For the initially sloping bed, directly behind the bed the pressure and bed topography balance the drag and the net momentum source is also zero. In the bulk of the flow between the front and the original position of the dam, the momentum source due to pressure is zero and the constant slope of the bed
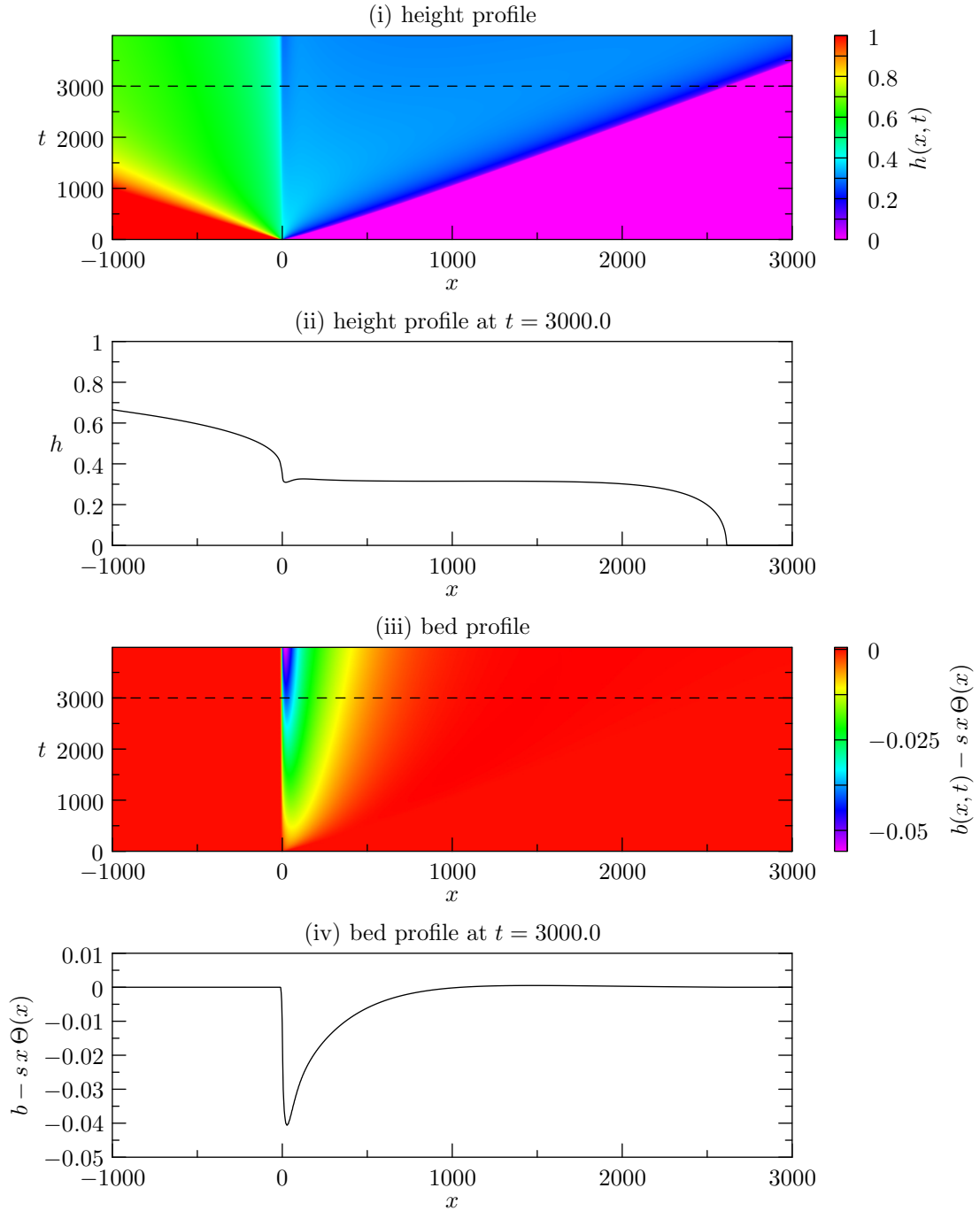
Figure 4.22: Height and relative bed elevation for an initially sloping bed. Parameter values used were $C_D = 0.0005$, $\phi_0 = 0.01$, $\gamma = 2.5$, $u_d = 0.005$, $u_e = 0.003$, $n = 1.3$, $u_c = 0.6$, $s = -0.001$, and $\beta = 1.0$.

balances the drag. For very shallow slopes the evolution of the flow downstream of the original position of the dam is governed by the balance between pressure and drag. For modest slopes the evolution of the flow downstream of the original position of the dam is governed by the balance between the bed slope and drag.

For both the initially flat and sloping beds a scour pit develops underneath the original position of the dam and the resulting source balances are more complex as compared to downstream of the dam. For the initially flat bed a hydraulic jump is formed above the scour pit resulting in a positive pressure gradient and a negative momentum source. For the initially sloping bed, although a scour pit develops underneath the original position of the dam, the right side of the pit is missing since the bed has a downward slope. As such, the height profile drops abruptly above the dam instead of forming a hydraulic jump. This results in a negative pressure gradient and a positive momentum source.

Finally, we note that for both the initially flat and sloping beds the momentum gained or lost due to the exchange of sediment between the flow and the bed is very small. This is consistent with how the particle momentum exchange term entered the momentum equation (ie, through the Boussinesq approximation), and demonstrates that the momentum exchanged between the bed and the fluid through deposition and erosion does not play a significant role in the dynamics of the flow or the sediment.

4.3.6   Critical Froude number

In this section we present results for the case where the predicted Froude number is unity so that surface N-waves are produced as in Section 4.3.1.

In Figure 4.24 we have plotted the height and bed profiles for an initially sloping bed with a small Gaussian bump centred at $x = 600$. The drag and slope parameters have been chosen so that the predicted Froude number is equal to unity and hence surface N-waves are generated as outlined previously. A hydraulic jump is formed immediately upstream of the bump shortly after the fluid overtakes the bump. However, the bump is slowly eroded and eventually disappears leaving only a slight depression in the bed which travels slowly upstream. While the bump is being eroded it spreads spatially and also moves slowly upstream. Downstream of the bump surface N-waves are generated by small bed disturbances created by erosion. The N-waves and bed ripples are seen to travel slowly upstream.
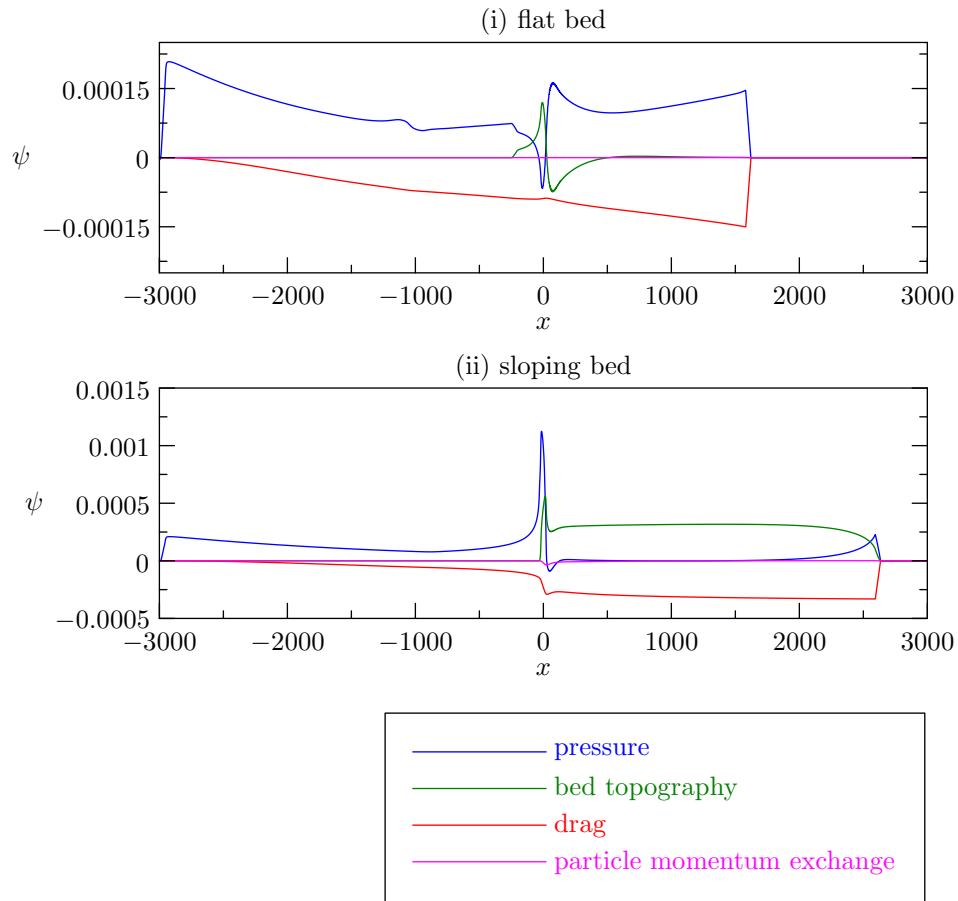
Figure 4.23: (i) Momentum source terms for an initially flat bed at $t = 3000$. Parameter values used are $C_D = 0.001$, $\phi_0 = 0.01$, $\gamma = 2.5$, $u_d = 0.005$, $u_e = 0.003$, $n = 1.0$, $u_c = 0.4$, and $\beta = 1.0$. (ii) Momentum source terms for an initially sloping bed at $t = 3000$. Paramter values used are $C_D = 0.0005$, $\phi_0 = 0.01$, $\gamma = 2.5$, $u_d = 0.005$, $u_e = 0.003$, $n = 1.3$, $u_c = 0.6$, $s = -0.001$, and $\beta = 1.0$.
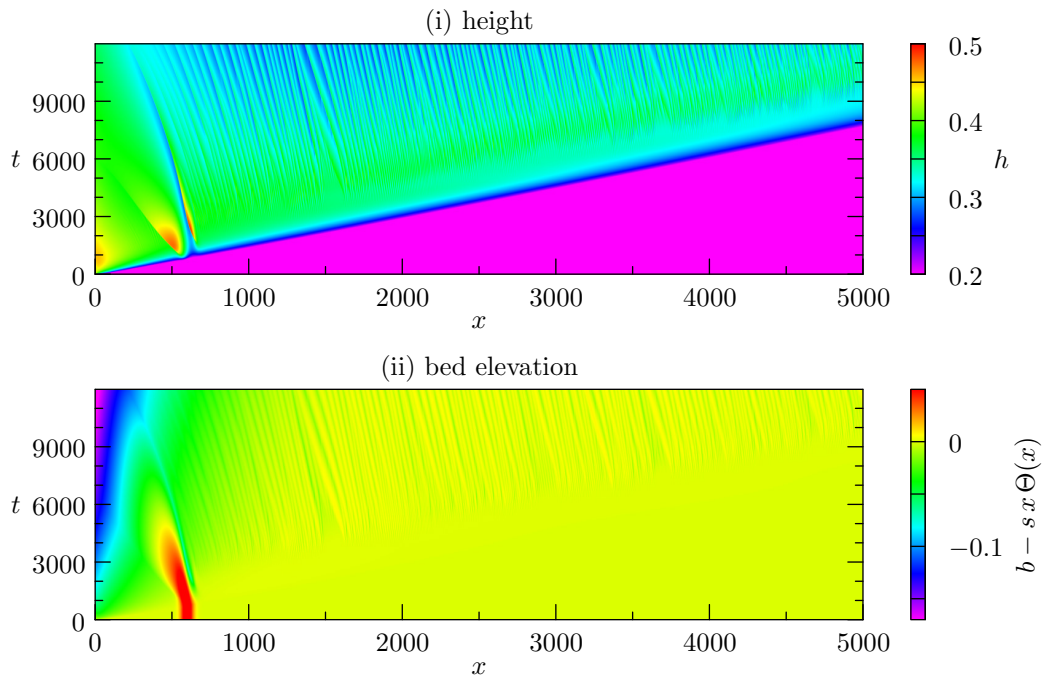
Figure 4.24: (i) Height profile and (ii) relative bed elevation for an initially sloping bed with a small Gaussian bump at $x = 600$. Parameter values used were $C_D = 0.001$, $\phi_0 = 0.01$, $\gamma = 2.5$, $u_d = 0.005$, $u_e = 0.003$, $n = 1.0$, $u_c = 0.3$, $s = -0.001$, and $\beta = 1.0$.

In Figure 4.25 we have plotted height, bed, and velocity profiles for the same flow as in Figure 4.24 at $t = 12000$. The surface N-waves are clearly shown in the height profile. Aside from the N-wave structures the flow behaves roughly as it would if deposition and erosion had been suppressed (ie, the front position and 'average' height, velocity, and volume fraction profiles are unaffected aside from the N-wave structures). Focusing on the structure of the N-waves, we note that each N-wave consists of relatively slow deep water transitioning into relatively fast shallow water. As such, the myriad of N-waves could be considered as many small hydraulic jumps. Furthermore, each N-wave has a corresponding bed ripple which is deepest where the fluid transitions abruptly from faster to slower velocities. This is consistent with the erosion model (2.26) in which the rate of erosion increases with velocity. In other words, in the trough of each N-wave the velocity is highest and hence the effect of erosion is strongest there so that the bed is eroded. Crossing the jump into the peak of the next N-Wave, the velocity is lowest and hence the effect of erosion of weakest there.

The N-waves observed in Figures 4.24 and 4.25 were also observed for initially smooth sloping beds (ie, without bumps). As the bed is eroded small perturbations in the bed excite the forced KdV waves as outlined in Section 4.3.1 since the Froude number of the flow is critical. These KdV waves grow in amplitude until they form slowly upstream-travelling N-waves, and the structure of velocity profiles in these N-waves results in an erosion pattern that is reminiscent of bed ripples. These ripples are coupled to the overlying N-waves so that they too travel slowly upstream. The structure and coupling of the N-waves and bed ripples is sustained for very long times.

4.3.7 Stepping

In this section we present results for the case where the predicted Froude number is unity so that surface waves are likely to be produced as in Section 4.3.1, except we have chosen parameters which result in slightly different flow and bed dynamics.

In Figure 4.26 we have plotted the bed elevation for an initially sloping bed. The drag and slope parameters where chosen so that the predicted Froude number was unity, but the critical bed velocity u_c was chosen so that once surface waves were produced, the velocity of the flow oscillated about the critical bed velocity. That is, when producing Figure 4.25 we noticed that, roughly speaking, in each N-wave the velocity oscillated between the non-dimensional values of 0.5 and 0.6, and hence to produce Figure 4.26 the critical bed velocity u_c was chosen to be
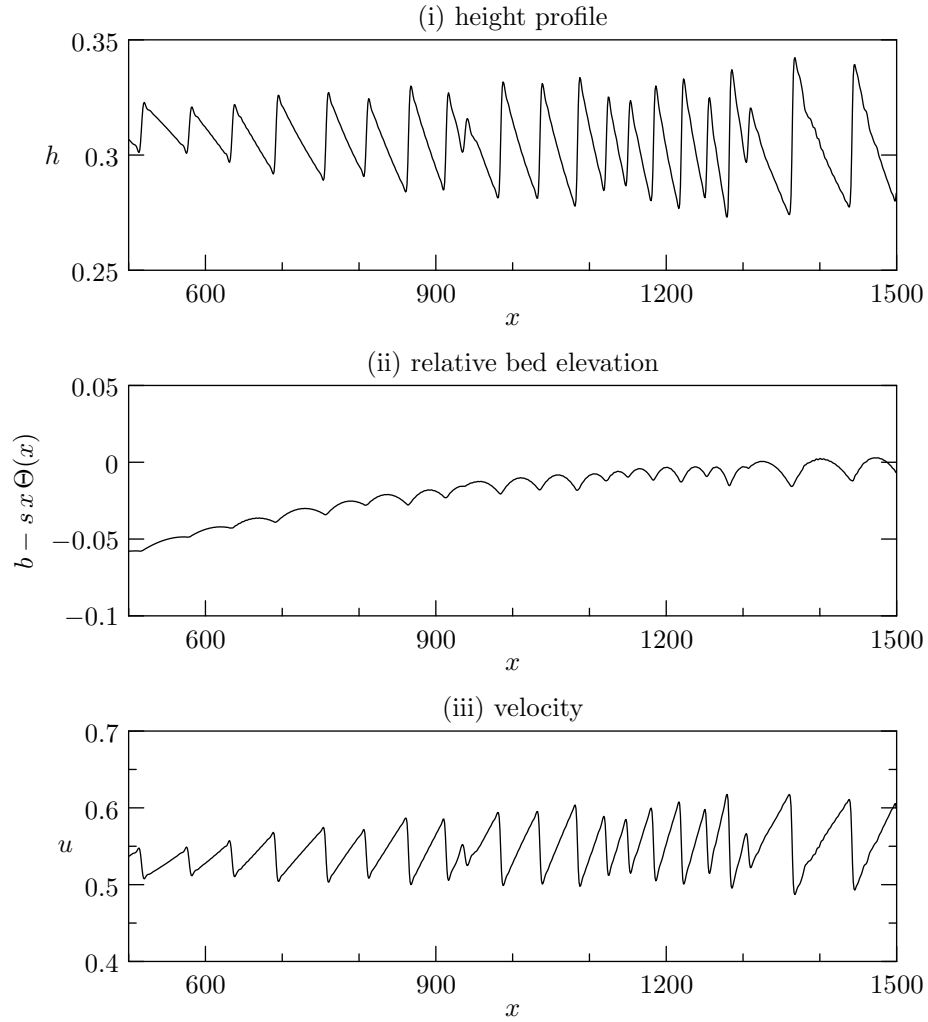
Figure 4.25: (i) Height profile, (ii) relative bed elevation, and (iii) velocity profile for an initially sloping bed with a small Gaussian bump at $x = 600$ at $t = 12000$. Parameter values used were $C_D = 0.001$, $\phi_0 = 0.01$, $\gamma = 2.5$, $u_d = 0.005$, $u_e = 0.003$, $n = 1.0$, $u_c = 0.3$, $s = -0.001$, and $\beta = 1.0$.
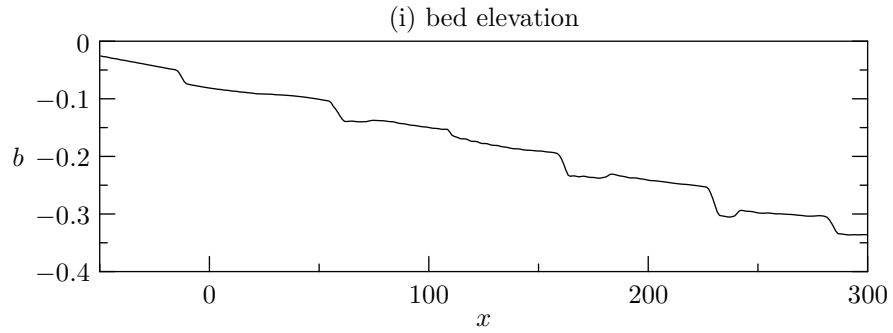
(i) bed elevation

Figure 4.26: Bed elevation for an initally sloping bed at $t = 12000$. Parameter values used were $C_D = 0.001$, $\phi_0 = 0.01$, $\gamma = 2.5$, $u_d = 0.005$, $u_e = 0.008$, $n = 0.5$, $u_c = 0.55$, $s = -0.001$, and $\beta = 1.0$.

0.55. The resulting bed topography exhibits step-like behaviour as compared to the ripple-like behaviour seen previously. These steps are reminiscent of the cyclic steps that developed in the bed of the laboratory flume of [32] in which water flowed over fine gravel.

Chapter 5

Numerical method

The numerical method used to solve the model equations (2.19) throughout this work is a finite-volume scheme in which the flux and source terms are computed based on Weighted Essentially Non-Oscillatory (WENO) reconstructions. The scheme can be applied to systems of balance laws of the form

$$\frac{\partial}{\partial t}\boldsymbol{q} + \frac{\partial}{\partial x}\big(\boldsymbol{f}(\boldsymbol{q}, x, t)\big) = \boldsymbol{\psi}(\boldsymbol{q}, x, t) \tag{5.1}$$

where $\boldsymbol{q} = \boldsymbol{q}(x, t)$ is a vector of unknowns.

All of the codes used to generate the data and figures in this work are available online at:

$$\texttt{http://www.math.ualberta.ca/\~memmett/dambreak/}$$

The codes are made available to others in the spirit of collaboration, openness, and reproducibility. Further information on how to run the codes can be found on the website listed above.

5.1   WENO reconstructions

For the sake of simplicity we will focus our attention on one-dimensional hyperbolic balance laws of the form

$$q_t + \big(f(q)\big)_x = 0. \tag{5.2}$$

Finite-volume schemes do not solve (5.2) directly; they solve its integrated version instead. Integrating (5.2) over the interval $[a, b]$ we obtain

$$\frac{\mathrm{d}}{\mathrm{d}t}\bar{q}(t) + \frac{1}{b - a}\Big(f\big(q(b, t)\big) - f\big(q(a, t)\big)\Big) = 0$$

where

$$\bar{q}(t) \equiv \frac{1}{b - a} \int_a^b q(\xi, t)\, d\xi$$

is the average value of q over $[a, b]$. This leads us to one of the central problems in implementing a numerical scheme to solve (5.2): obtaining the values of q at the boundaries a and b based on the averages $\bar{q}$ of q. This is the *reconstruction* problem.

Before proceeding we will need to define notation regarding the spatial grid (discretisation).

5.2 Grid

We consider a grid over the interval $[a, b]$ with N cells. We denote the $N + 1$ cell boundaries by

$$x_{i-1/2} \quad \text{for} \quad i = 1, \ldots, N + 1 \tag{5.3}$$

so that

$$a = x_{1/2} < x_{3/2} < \cdots < x_{N-1/2} < x_{N+1/2} = b. \tag{5.4}$$

Subsequently, we denote the N cells by

$$C_i = [x_{i-1/2}, x_{i+1/2}] \quad \text{for} \quad i = 1, \ldots, N; \tag{5.5}$$

the N cell centres by

$$x_i = \frac{x_{i-1/2} + x_{i+1/2}}{2} \quad \text{for} \quad i = 1, \ldots, N; \tag{5.6}$$

the N cell sizes by

$$\Delta x_i = x_{i+1/2} - x_{i-1/2} \quad \text{for} \quad i = 1, \ldots, N; \tag{5.7}$$

and the maximum cell size by

$$\Delta x = \max_{i=1,\ldots,N} \Delta x_i. \tag{5.8}$$

We denote the contiguous stencil around the cell C_i, containing k cells shifted to the left by r cells, by

$$S_i^{r,k} = C_{i-r} \cup \cdots \cup C_{i-r+k-1}. \tag{5.9}$$

Note that $S_i^{r,k}$ spans k cells and contains $k+1$ cell boundaries.

5.3 One dimensional reconstruction for smooth functions

Given the cell averages $\bar{q}_j$ of a function f where

$$\bar{q}_j = \frac{1}{\Delta x_j} \int_{x_{j-1/2}}^{x_{j+1/2}} q(\xi)\, d\xi \tag{5.10}$$

we wish to find approximations to the function q at various points within each cell. In particular, we might be interested in approximating the function at the left cell boundary $x_{i-1/2}$, the right cell boundary $x_{i+1/2}$, or at any point ξ within the cell C_i. If the approximations are computed using k cell averages, they should be k-order accurate. The remainder of this section will be devoted to finding these approximations and showing that they are k-order accurate. As it turns out, we will show that there are constants c_j (hereafter called *reconstruction coefficients*) such that the reconstructed values are given by

$$q(\xi) \approx \sum_{j=0}^{k-1} c_j\, \bar{q}_{i-r+j}. \tag{5.11}$$

That is, given a stencil $S_i^{r,k}$ that spans the k cells $C_{i-r}, \ldots, C_{i-r+k-1}$, the reconstructed value of the original function at some point ξ in C_i can be obtained using a simple linear combination of the averages $\bar{q}_j$ over the cells C_j in the stencil $S_i^{r,k}$. In general, the reconstruction coefficients c_j depend on the reconstruction point ξ, order k, left shift r, and cell C_i, but *not* on the function q.

In order to obtain the reconstruction coefficients c_j and prove accuracy, we will find polynomials p_i^r of degree at most $k-1$ such that each p_i^r is a k-order accurate approximation to f inside C_i. That is, given the cell averages $\bar{q}_j$, we will find polynomials p_i^r such that

$$p_i^r(x) = q(x) + O(\Delta x^k) \quad \text{for} \quad x \in C_i.$$

69

In order to find these polynomials, we consider the primitive function

$$V(x) = \int_a^x q(\zeta) \, d\zeta. \tag{5.12}$$

Using the cell averages $\bar{q}_j$ we can compute V at the cell boundaries $x_{i+1/2}$ through

$$\begin{aligned}
V(x_{i+1/2}) &= \int_a^{x_{i+1/2}} q(\xi) \, d\xi \\
&= \sum_{j=1}^i \int_{x_{j-1/2}}^{x_{j+1/2}} q(\xi) \, d\xi \\
&= \sum_{j=1}^i \bar{q}_j \Delta x_j. \tag{5.13}
\end{aligned}$$

Focusing on a particular cell C_i and stencil $S_i^{r,k}$, the unique polynomial P_i^r of order k which interpolates V at the $k+1$ points

$$x_{i-r-1/2}, \; \ldots, \; x_{i-r+k-1/2}$$

is given by

$$P_i^r(x) = \sum_{l=0}^k \left(V(x_{i-r+l-1/2}) \prod_{m=0,m\neq l}^k \frac{(x - x_{i-r+m-1/2})}{(x_{i-r+l-1/2} - x_{i-r+m-1/2})} \right). \tag{5.14}$$

This is the interpolating polynomial of V in Lagrange form. It can be shown that

$$P_i^r(x) = V(x) + O(\Delta x^{k+1}) \quad \text{for} \quad x \in S_i^{r,k}.$$

Therefore, the derivative p_i^r of P_i^r satisfies

$$p_i^r(x) = \frac{\mathrm{d}}{\mathrm{d}x} P_i^r(x) = q(x) + O(\Delta x^k) \quad \text{for} \quad x \in S_i^{r,k}$$

and p_i^r is of order $k - 1$.

Furthermore, the cell averages of p_i^r over the cells C_j that comprise the stencil $S_i^{r,k}$
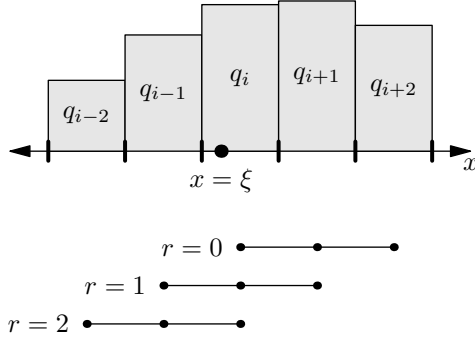
Figure 5.1: Possible stencils for $k = 3$ corresponding to left-shifts of $r = 0, 1$, and 2. Each stencil can be used to build reconstructions at $x = \xi$ in the cell C_i using the cell averages within the stencil.

satisfy

$$
\begin{aligned}
\frac{1}{\Delta x_j} \int_{x_{j-1/2}}^{x_{j+1/2}} p_i^r(\xi) \, d\xi &= \frac{1}{\Delta x_j} \int_{x_{j-1/2}}^{x_{j+1/2}} P_i'(\xi) \, d\xi \\
&= \frac{1}{\Delta x_j} \left(P_i^r(x_{j+1/2}) - P_i^r(x_{j-1/2}) \right) \\
&= \frac{1}{\Delta x_j} \left(V(x_{j+1/2}) - V(x_{j-1/2}) \right) \\
&= \frac{1}{\Delta x_j} \left(\int_a^{x_{j+1/2}} q(\xi) \, d\xi - \int_a^{x_{j-1/2}} q(\xi) \, d\xi \right) \\
&= \frac{1}{\Delta x_j} \left(\int_{x_{j-1/2}}^{x_{j+1/2}} q(\xi) \, d\xi \right) \\
&= \bar{q}_j \quad \text{for} \quad j = i - r, \ldots, i - r + k - 1.
\end{aligned}
$$

That is, the cell averages of the approximating polynomials p_i^r match the cell averages the original function in each of the cells C_j which comprise the stencil $S_i^{r,k}$.

So far we have constructed polynomials p_i^r that approximate the original function q on the stencils $S_i^{r,k}$ to k-order using only the cell averages $\bar{q}_j$ for $j = i - r, \ldots, i - r + k - 1$. The possible left-shifts r are illustrated for $k = 3$ in Figure 5.1.

Now we consider the practical problem of finding the constants c_j. Subtracting $V(x_{i-r-1/2})$ from $P_i^r(x)$ and using

$$
\sum_{l=0}^k \prod_{m=0, m \neq l}^k \frac{(x - x_{i-r+m-1/2})}{(x_{i-r+l-1/2} - x_{i-r+m-1/2})} = 1
$$

71

and
$$V(x_{i-r+l-1/2}) - V(x_{i-r-1/2}) \equiv 0 \text{ for } l = 0$$

we obtain

$$P_i^r(x) - V(x_{i-r-1/2}) =$$
$$\sum_{l=1}^{k} \left(\left(V(x_{i-r+l-1/2}) - V(x_{i-r-1/2}) \right) \prod_{m=0,m \neq l}^{k} \frac{(x - x_{i-r+m-1/2})}{(x_{i-r+l-1/2} - x_{i-r+m-1/2})} \right).$$

Taking the derivative of the above, we obtain

$$p_i^r(x) = \sum_{l=1}^{k} \Bigg(\left(V(x_{i-r+l-1/2}) - V(x_{i-r-1/2}) \right) \qquad\qquad (5.15)$$
$$\cdot \frac{\sum_{m=0,m \neq l}^{k} \prod_{n=0,n \neq l,m}^{k}(x - x_{i-r+n-1/2})}{\prod_{m=0,m \neq l}^{k}(x_{i-r+l-1/2} - x_{i-r+m-1/2})} \Bigg).$$

Employing (5.13), we obtain

$$p_i^r(x) = \sum_{l=1}^{k} \Bigg(\left(\sum_{j=0}^{l-1} \bar{q}_{i-r+j} \Delta x_{i-r+j} \right) \qquad\qquad (5.16)$$
$$\cdot \frac{\sum_{m=0,m \neq l}^{k} \prod_{n=0,n \neq l,m}^{k}(x - x_{i-r+n-1/2})}{\prod_{m=0,m \neq l}^{k}(x_{i-r+l-1/2} - x_{i-r+m-1/2})} \Bigg).$$

Rearranging, we obtain

$$p_i^r(x_{i+1/2}) = \sum_{j=0}^{k-1} \sum_{l=j+1}^{k} \frac{\sum_{m=0,m \neq l}^{k} \prod_{n=0,n \neq l,m}^{k}(x - x_{i-r+n-1/2})}{\prod_{m=0,m \neq l}^{k}(x_{i-r+l-1/2} - x_{i-r+m-1/2})} \Delta x_{i-r+j} \bar{q}_{i-r+j}.$$

Therefore, the reconstruction coefficients c_j used to reconstruct the function f at the point ξ are given by

$$c_j = \sum_{l=j+1}^{k} \frac{\sum_{m=0,m \neq l}^{k} \prod_{n=0,n \neq l,m}^{k}(\xi - x_{i-r+n-1/2})}{\prod_{m=0,m \neq l}^{k}(x_{i-r+l-1/2} - x_{i-r+m-1/2})} \Delta x_{i-r+j}. \qquad (5.17)$$

Note that the the reconstruction coefficients c_j depend on ξ, i, r, and k.

5.4 One dimensional reconstruction for piece-wise smooth functions

The solutions of hyperbolic balance laws may contain discontinuities, and therefore we are interested in reconstructing piecewise smooth functions. A piecewise smooth function q is smooth except at finitely many isolated points. At these points, q and its derivatives (at least up to the order of the scheme) are assumed to have finite left and right limits.

For such piecewise smooth functions, the order of accuracy herein referred to is formal. That is, it is defined as the accuracy determined by the local error in the smooth regions of the function.

The basic idea of WENO is to use a convex combination of several stencils to form the reconstruction of q, and, if a stencil contains a discontinuity, its weight should be close to zero. In smooth regions, using several stencils will also serve to increase the order of accuracy.

Consider the k stencils

$$S_i^{r,k} \quad \text{for} \quad r = 0, \ldots, k-1$$

that can be used to reconstruct the value of q at some point ξ in the cell C_i. These stencils span $2k-1$ cells. We denote the k different reconstructions by

$$q(\xi) \approx q^r = \sum_{j=0}^{k-1} c_j^r \bar{q}_{i-r+j} \quad \text{for} \quad r = 0, \ldots, k-1 \tag{5.18}$$

where we have added the superscript r to the function f and the reconstruction coefficients c_j to make their dependance on the left shift r explicit.

A WENO reconstruction takes a convex combination of all q^r defined in (5.18) as a new approximation according to

$$q(\xi) \approx \sum_{r=0}^{k-1} \omega_i^r q^r \tag{5.19}$$

where we require

$$\omega_i^r \geq 0 \quad \text{and} \quad \sum_{r=0}^{k-1} \omega_i^r = 1. \tag{5.20}$$

In smooth regions where all k stencils that can be used to reconstruct $q(\xi)$ in (5.18) do not contain discontinuities, we could reconstruct $q(\xi)$ to order $2k-1$ using the stencil $S_i^{k-1,2k-1}$ to obtain

$$q(\xi) = \sum_{j=0}^{2k-2} c_j^* \, \bar{q}_{i-(k-1)+j} \tag{5.21}$$

where we have added the superscript $*$ to the reconstruction coefficients c_j to highlight that they are optimal (ie, higher order). Combining (5.18), (5.19), and (5.21), we obtain

$$\sum_{j=0}^{2k-2} c_j^* \, \bar{q}_{i-(k-1)+j} = \sum_{r=0}^{k-1} \omega_i^r \left(\sum_{l=0}^{k-1} c_l^r \, \bar{q}_{i-r+l} \right). \tag{5.22}$$

Rearranging, we obtain

$$\sum_{j=0}^{2k-2} c_j^* \, \bar{q}_{i-(k-1)+j} = \sum_{j=0}^{2k-2} \left(\sum_{l=\max(0,j-k+1)}^{\min(k-1,j)} \omega_i^{k-(j+1)+l} c_l^{k-(j+1)+l} \right) \bar{q}_{i-(k-1)+j}.$$

Therefore, we have $2k-1$ equations

$$\sum_{l=\max(0,j-k+1)}^{\min(k-1,j)} \omega_i^{k-(j+1)+l} c_l^{k-(j+1)+l} = c_j^* \quad \text{for} \quad j = 0, \ldots, 2k-2 \tag{5.23}$$

at each i (and ξ) for the weights ω_i^r. For non-uniform grids the systems (5.23) are over-determined, and therefore we must use some kind of optimisation algorithm in order to find the weights ω_i^r. For uniform grids the systems (5.23) are no longer over-determined, and the weights ω_i^r can be found explicity (and are independent of i).

The weights ω_i^r defined by (5.22) and determined by (5.23) are called *optimal weights* since they can be used to reconstruct a function to order $2k-1$ in regions where the function is smooth. We will henceforth denote the optimal weights by ϖ_i^r.

We now consider the practical problem of choosing the weights ω_i^r. If we choose the weights ω_i^r sufficiently close to the optimal weights ϖ_i^r in regions where the function is smooth, then we can achieve $2k-1$ order accuracy. In order to determine how close to the optimal weights ϖ_i^r the weights ω_i^r must be choosen we consider the

reconstruction

$$f(\xi) \approx \sum_{r=0}^{k-1} \omega_i^r q^r = \sum_{r=0}^{k-1} \varpi_i^r q^r + \sum_{r=0}^{k-1} (\omega_i^r - \varpi_i^r) q^r. \tag{5.24}$$

If we choose

$$\omega_i^r = \varpi_i^r + O(\Delta x^{k-1}) \tag{5.25}$$

then each term in the last summation of (5.25) becomes $O(\Delta x^{2k-1})$ and therefore $2k - 1$ order accuracy is preserved by the reconstruction.

If we define

$$\omega_i^r = \frac{\alpha_i^r}{\alpha_i^0 + \cdots + \alpha_i^{k-1}} \tag{5.26}$$

where

$$\alpha_i^r = \frac{\varpi_i^r}{(\epsilon + \sigma_i^r)^p} \quad \text{for} \quad r = 0, \ldots, k-1; \tag{5.27}$$

and ϵ is a positive real number used to avoid dividing by zero (usually $\epsilon = 10^{-6}$), p is some power (usually 2), and σ_i^r is a measure of the smoothness of the function v in the stencil $S_i^{r,k}$; with the smoothnesses σ_i^r chosen appropriately, then (5.25) is satisfied.

Typically, the smoothness measurement presented by Jiang and Shu [29] is used. They define the smoothness according to

$$\sigma_i^r = \sum_{l=1}^{k-1} \int_{x_{j-1/2}}^{x_{j+1/2}} (\Delta x_j)^{2l-1} \left(\frac{d^l}{dx^l} p_i^r(x) \right)^2 dx \tag{5.28}$$

which is the sum of the L^2 norms of the derivatives of the approximating polynomial.

5.5   Locating the wet/dry interface of dam-break flows with drag

In this section we present the algorithm that is employed by our dam-break solver in order to locate the wet/dry interface of dam-break flows directly. Throughout the remainder of this section we will: call the cell which contains the wet/dry interface the *front cell*, denote the index of the front cell by i_f, and denote the position of the wet/dry interface by x_f.

The wet/dry interface of a dam-break flow is a contact discontinuity since the

characteristic speeds of the system are equal when $h = 0$ and no information from the bulk of the fluid may be transported beyond the front. As such, the basic idea of our method was suggested by Harten in [25]. The algorithm that we use to locate the wet/dry interface is comprised of three main concepts:

1. *Stretching*: The front cell is adapted by contracting or stretching it. That is, the front cell's right boundary is moved to the front position x_f. We allow the front cell to be contracted arbitrarily, but do not allow it to be stretched beyond a preset threshold (usually taken to be 140% of its original width). As such, the wet/dry interface always occurs at a cell boundary so that no cells are partially filled by the fluid. In other words, the contact discontinuity always occurs at a cell boundary so that we can build reconstructions at the front that are not polluted by it.

2. *Re-averaging*: The quantities in the front cell are re-averaged whenever the front cell is adapted to reflect its new width.

3. *Searching*: A bi-section search is used to locate the point at which the height field vanishes based on purely upstream reconstructions using the adapted cell boundaries and re-averaged quantities as above. That is, the front position is moved and the height is subsequently reconstructed there. If the reconstructed height is equal to zero, the search is terminated.

Throughout each of these steps it is often necessary to reconstruct one or more of the unknowns at the front position x_f. This is accomplished by computing the reconstruction coefficients in (5.17) with $\xi = x_f$ and subsequently performing an upwind reconstruction according to (5.11) with $r = k - 1$.

We now present our algorithm for locating the wet/dry interface of a dam-break flow with drag. Initially, we locate the front position and front cell by searching through the initial condition for the first cell with zero height. During subsequent time-steps we locate the wet/dry interface by performing a bi-section search to find the point at which the height vanishes. During each iteration of the bi-section search the front position is moved and the height is reconstructed there. The search is terminated when the reconstructed height is zero. In pseudo-code, the algorithm is essentially:

1. high $\leftarrow x_{i_f - 1/2}$

2. low $\leftarrow x_{i_f + 1/2}$

76

3. **while** $|\text{high} - \text{low}| < \text{tolerance}$ **do**

4. $x_f \leftarrow (\text{high} + \text{low})/2$

5.   adapt the front cell: $x_{i_f+1/2} \leftarrow x_f$

6.   re-average quantities in the front cell

7.   compute new reconstruction coefficients

8. $h \leftarrow$ reconstructed height at x_f

9.   **if** $h > 0$ **then**

10. $\text{high} \leftarrow x_f$

11.   **else**

12. $\text{low} \leftarrow x_f$

13.   **end if**

14. **end while**

Finally, the index i_f of the front cell is advanced and all of the unknowns are re-averaged if the front cell has been stretched too much. The algorithm presented above is illustrated in Figure 5.2.

5.6 Numerical scheme

Integrating the balance law (5.1) over the grid cells, we obtain a set of evolution equations for each of the cell averages given by

$$
\begin{aligned}
\frac{\mathrm{d}}{\mathrm{d}t} \boldsymbol{q}_i = {} & \frac{1}{\Delta x_i} \Big(\boldsymbol{f}\big(\boldsymbol{q}(x_{i-1/2}, t)\big) - \boldsymbol{f}\big(\boldsymbol{q}(x_{i+1/2}, t)\big) \Big) \\
& + \frac{1}{\Delta x_i} \int_{x_{i-1/2}}^{x_{i+1/2}} \boldsymbol{\psi}(\boldsymbol{q}(x, t)) \; dx.
\end{aligned}
\tag{5.29}
$$

In order to evaluate the right-hand-side, we need to reconstruct $\boldsymbol{q}$ at: (i) the left edge of each cell, (ii) the right edge of each cell, and (iii) various quadrature points within each cell. However, note that the right edge of the cell C_i coincides with the left edge of cell C_{i+1}. As such, there are two different reconstructions for each boundary, and the fluxes in (5.29) should in fact be computed with a Riemann solver. That is, let $q_{i-1/2}^-$ be the reconstruction at the right edge of cell C_{i-1} (ie,
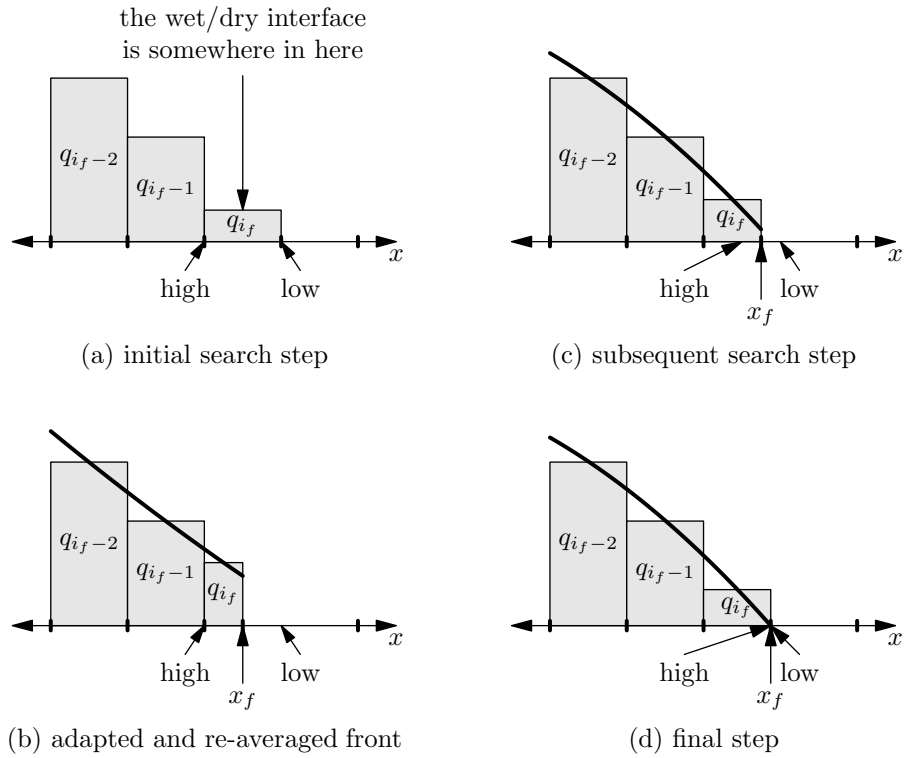
Figure 5.2: A few illustrative steps of the search algorithm. In each frame, the thick curve is the reconstruction polynomial $p_i^r(x)$ for the height profile. (a) The high and low markers are set to the front cell's boundaries. (b) The front position is set and the front cell is adapted. Note that the reconstructed height at the front is too high. (c) The high marker is adjusted, the front position is set, the front cell is adapted, and the height profile is reconstructed. Again, note that the reconstructed height at the front is too high. (d) Eventually, the high and low markers squeeze the front position. Finally, note that the reconstructed height profile at the front is equal to zero, which is the desired result.

the reconstruction at $x_{i-1/2}$ from below), and $q_{i-1/2}^+$ be the reconstruction at the left edge of cell C_i (ie, the reconstruction at $x_{i-1/2}$ from above). In general, $q_{i-1/2}^-$ and $q_{i-1/2}^+$ are not equal, and so we use the simple Lax-Friedrichs numerical flux given by

$$F(q^-, q^+) = \frac{1}{2}\left(f(q^+) + f(q^-) - \alpha(q^+ - q^-)\right) \qquad (5.30)$$

where α is the maximum wave speed of the system to compute the fluxes in (5.29).

The numerical scheme used through this work is as follows:

1. Given an initial condition $q(x, 0)$ and a set of grid cells C_i, compute the average value of $q(x, 0)$ in each cell and store as q_i.

2. Compute the smoothness indicators σ_i^r based on the cell averages q_i.

3. Reconstruct the unknown q at the following points withing each cell: (i) the left edge, (ii) the right edge, and (iii) quadrature points. For each reconstruction point:

   (a) Compute the weights ω_i^r based on the smoothness indicators σ_i^r and the optimal weights ϖ_i^r.

   (b) Compute the low-order reconstructions q_i^r based on the cell averages q_i.

   (c) Compute the higher-order reconstructions based on the reconstructions q_i^r and weights ω_i^r.

4. Compute the numerical flux at each cell boundary using the Lax-Friedrichs flux (5.30).

5. Compute the quadrature of the source terms.

6. Sum the flux and source terms to obtain updates to each cell.

7. Evolve the cell averages q_i using a time-stepping scheme (such as a Runge-Kutta scheme) based on the updates in Step 6.

8. Repeat until final time reached.

Again, at the front the reconstructions are based on purely upwind reconstructions (ie, not WENO reconstructions).

Chapter 6

Discussion

In Chapter 2 we developed a model to describe the transport of dilute sediment under dam-break flows with basal drag and varying bottom topography. The model developed includes a velocity dependent basal drag force, incorporates the effects of a spatially dependent bed topography that changes with time, and allows the variable concentration of suspended particles, through the mechanisms of deposition and erosion, to influence the flow dynamics. The model is unique from existing models which do not couple the flow and sediment dynamics and do not include basal drag [42] or bed topography. The numerical results show that this coupling is especially important for the sediment dynamics and for critical Froude number flows.

We considered the two-dimensional flow resulting from the sudden release of either pure water or dilute suspensions initially held at rest behind a plane vertical barrier of height h_0. The bed was taken to be horizontal and it was assumed that there was no water below the dam initially. The aspect ratio was assumed to be small in accord with experimental results and therefore vertical accelerations were neglected and a hydrostatic pressure distribution was adopted [16, 48, 45, 26, 54, 49]. A basal drag term was added to the horizontal momentum equation to account for the blunting and retarding of the flow front as seen in experiments [16, 48, 53, 15, 26]. The effect of suspended particles entered the flow dynamics through the buoyancy terms and both erosion and deposition of particles were accounted for in the model so that the buoyancy effects varied in both space and time. The suspended particles were assumed to be vertically well-mixed so that the volume fraction of particles depended only on the stream-wise coordinate and time [7, 6, 8, 42, 26, 44]. The particles were assumed to have negligible inertia [40] and particle diffusion in the stream-wise direction was assumed to be dominated by advection [44]. Four

conservation equations were derived for the fluid mass, horizontal momentum, particle mass, and bed material mass. Again, the flow and sediment dynamics were coupled through the horizontal momentum, and the mechanisms of sediment deposition and entrainment through bed erosion appeared as source terms in the conservation of particle mass equation. The bed topography was allowed to change with time through the mechanisms of deposition and erosion. However, the model does not account for particle-particle interactions, and only couples the flow and sediment dynamics through the momentum equation by changing the density upon which gravity acts. As such, the model is limited to small volume fractions of sediment so that particle-particle interactions are unlikely. This limits our choice of input parameters to ones which result in flows that remain sufficiently dilute.

In Section 4.1.1 we considered a simple particle free dam-break flow without basal drag. The numerical scheme produced results which were in excellent agreement with the well known Ritter solution [45]. The height profiles demonstrated the simple wave structure of the Ritter solution, which connects the constant states of $h = 1$ and $h = 0$ with a rarefaction wave that is a function of the similarity variable $\xi = x/t$.

In Section 4.1.2 we considered a particle free dam-break flow with basal drag. Adding hydraulic resistance through the mechanism of basal drag [15, 53, 54, 26] destroyed the simple wave structure present in the Ritter solution as the conservation of momentum law became non-homogenous. We did not impose any dynamic conditions at the front. The effects of basal drag were most prominent in the vicinity of the tip where the unimpeded flow had a depth that fell to zero in a continuous fashion. The shape of the tip was significantly altered compared to the Ritter solution such that rather than decreasing smoothly to zero with a parabolic profile the depth of the flow decreased abruptly to form a blunt snout at the leading edge. The addition of the Chézy drag term brought the solution into closer accord with the experimental results of Dressler [15], and to a lesser extent the more recent experimental results of Stansby, Chegini, and Barnes [48]. The front speed of the solution with basal drag was non-constant and decreased with time until the effect of drag balances the fluid's inertia. The maximum horizontal velocity occurred at the front, and the velocity was nearly uniform within the snout. In conclusion, basal friction impedes the flow by differing amounts according to the values taken for the Chézy drag coefficient. These changes are observed in experiments and were reflected in the subsequent rate of erosion in a nonlinear fashion, and furthermore, these influences were not included in the model for sediment transport under dam-break flow presented by Pritchard and Hogg [42].

In Section 4.1.3 we considered various particle laden dam-break flows with basal drag whose particle volume fraction was dynamic and changed through the mechanisms of particle advection, deposition, and entrainment through bed erosion. We demonstrated the role played by the critical bed velocity u_c in the long term competition between erosion and deposition and displayed the strong effect of basal drag on the ultimate outcome of this competition. Again, inclusion of a frictional term in models for suspended sediment transport via dam-break flows appears to be a new addition to the literature [42] and the effect of its inclusion is often dominant over other mechanisms in determining the efficacy of this mode for sediment transport. We noted that the presence of a dilute suspension did not have a significant effect on the height or velocity profiles of the flows and the overall shape of these profiles for flows with particles where essentially the same as the analogous particle free profiles. Generally, flows with particles were slightly faster compared to analogous particle free flows, but only by a few percent at most.

The maximum rate of sediment entrainment occurred at the front and was nearly uniform within the snout. Peaks in the volume fraction of particle profiles were observed directly behind the front where the height of the fluid decreased sharply to zero. These peaks in the volume fraction of particles where highest for short post-release times since the velocity was also highest for short post-release times, and decreased with time. As time increased the front speed decreased due to basal drag and hence the rate of entrainment also decreased, resulting in a decreasing volume fraction of sediment in the snout as particles settled out of suspension. By increasing the critical bed velocity u_c above which the bed erodes and particles are entrained into the fluid a higher bed shear, and hence velocity, was needed in order to erode the bed and entrain particles. If the Chézy drag coefficient C_D was large enough so that the flow was kept from reaching this critical bed velocity no particles were entrained by the flow. We explored this complex interplay between the basal drag and the critical bed velocity and showed that the volume fraction of particles may approach a steady state in the bulk of the flow or fall to zero depending on the values of the drag coefficient C_D and the critical bed velocity u_c. Furthermore, for small values of the drag coefficient the numerical results confirmed our asymptotic deductions regarding the long term behaviour of the volume fraction of particles. Namely, that when $u_c < 2/3$ the bed continued to be eroded for all post-release times and the volume fraction of particles approached a non-zero steady state after the mechanisms of deposition and erosion reached an equilibrium.

The interplay between basal drag and the critical bed velocity was further demon-

strated by examining the particle flux at a fixed station. Flows with high basal drag did not continue to erode the bed and entrain particles once the front had passed a given station. This was due to the fact that the drag slowed the flow appreciably so that the velocity in the bulk of the fluid was less than the critical bed velocity and the particle flux was henceforth dominated by deposition regardless of the value of the critical bed velocity. Flows with a critical bed velocity above 2/3 were also dominated by deposition because the long term Ritter velocity is less than 2/3 regardless of the presence of basal drag. Flows with low drag and a critical bed velocity below 2/3 continued to erode the bed and advect entrained particles downstream. As time progressed, the horizontal velocity at the station approached its Ritter solution and the particle flux due to erosion approached a steady value while the particle flux due to deposition increased with increasing volume fraction until an equilibrium between erosion and deposition was reached. We conclude that the presence and intensity of basal drag and its interplay with the critical bed velocity determines the long term behaviour of sediment transport. Flows can either sustain erosion for all post-release times and obtain a non-zero steady load of sediment, or cease erosion at some post-release time and deposit their sediment load.

We noted that the dimensionless exponent n differentiated the flow between two types, where the volume fraction in the bulk is relatively high and the volume fraction profiles do not have a peak at the front; and where the volume fraction in the snout is relatively high and the volume fraction profiles do have a peak at the front.

In Section 4.2.1 we considered particle free flows over flat, frictionless beds for which there was shear in the vertical profiles of the velocity so that the shape factor $\beta > 1$. Following Hogg and Pritchard [26] we showed that for modified dam-break flows without basal drag it is no longer possible to locate the front of the flow unless $\beta \to 1$ at the front. We illustrated this, and presented implicit plots, for the case where β was constant. In the case where β is constant and not equal to unity we observed that the most significant departures from the Ritter solutions occurred in regions where h was small and u was greater than unity.

In Section 3.2 we considered particle free dam-break flows over a linear slope in order to isolate the effects of the source term relating to the bottom slope. By considering linearly sloping beds with small slopes we were able to perform an asymptotic analysis and obtained first order corrections to the Ritter solution. The asymptotic height correction showed an abrupt decrease in the height profile at $x = 0$ where the bed began to slope downward, and a slight bulking up of

the fluid in the body of the flow closer to the front. The height correction was parabolic with its maximum occurring over the sloping bed and behind the front. The height correction fell to zero at $x = 2t$ so that, to first order, the sloping bed did not affect the front position. The asymptotic velocity correction showed that the fluid moved faster everywhere over the sloping region of the bed, and it attained its maximum at the front.

In Section 4.2.2 we considered modified particle free dam-break flows over linear slopes in the presence of drag in order to isolate the effects of the source terms relating to the bottom slope and basal drag. The resulting height and velocity profiles differed significantly from previous results and foreshadowed subsequent results pertaining to sediment dynamics. Both the height and velocity profiles were nearly horizontal in the bulk of the flow over the linearly sloping bed. Furthermore, in the presence of a sloping bottom the blunt snout in the height profile was more abrupt and fell steeply to zero at the front. The effect of drag was to retard the front and create a blunt snout, while the effect of a sloping bottom is to draw out the fluid, reducing its height in the bulk of the flow over the sloping bed, and slightly increasing its height directly behind the front. Again, the introduction of vertical shear altered the height profile so that the surface of the flow no longer intersected the bed at an oblique angle.

In Section 4.2.3 we considered dam-break flows over linearly sloping erodible beds in the presence of drag, exploring the complex interactions between particles and flow when basal drag, bottom topography, erosion, and sedimentation are taken into account. We observed that, as in the previous case with flat beds, the inclusion of particles did not have a significant effect on the height or velocity profiles of the flows. Since the velocity over the sloping region was nearly horizontal and particles are advected downstream with the same velocity as the flow, particles entrained into the flow maintained their relative position within the flow resulting in nearly linear volume fraction profiles that increased in the downstream direction, and whose maximum continued to increase for all post-release times in contrast to the flat bed case. The peak in the volume fraction occurred directly behind the front, and is primarily due to advection coupled with the nearly horizontal velocity profile over the sloping bed.

In Section 4.3.1 we reviewed some of the analysis done by [31] which pertained to the generated of surface N-waves in shallow-water flows with small bed disturbances. When the Froude number of the flow is close to unity, small perturbations in the height and momentum fields caused by bed disturbances travel through the flow with a characteristic velocity that is the same as the physical fluid velocity, al-

lowing the perturbations to grow according to a forced KdV equation. Eventually, these perturbations interact with bed disturbance and turn into surface N-waves.

In Section 4.3.2 we developed a heuristic with which we could predict the Froude number of the flow prior to releasing the dam. With this heuristic, we could chose parameter values so that surface N-waves would likely be observed. We also demonstrated that the Froude number heuristic developed performs well for sufficiently steep gross bed slopes.

In Sections 4.3.3 and 4.3.4 we considered two relatively simple cases: flow over a flat bed and flow over an initially sloping bed. In each case, a sour pit developed under the original position of the dam. In the flat bed case, most of the sediment removed from the scour pit was deposited just downstream of the pit resulting in a net increase in the bed elevation there. In the sloping bed case, deposition was not strong enough to overcome erosion just downstream of the scour pit, and a net increase in the bed elevation was not seen. The dynamics of the height and momentum fields for these two cases are not significantly altered by the presence of sediment or changing bed topography as in our previous studies ([19, 20]).

In Section 4.3.5 we considered the relative strengths of the momentum sources for the flat and sloping beds considered previously. For the flat bed, the flow is primarily governed by the balance between the pressure gradient and drag. For the sloping bed, the flow is primarily governed by the balance between the momentum source due to the bed slope and drag. In each case, the momentum gained or lost through the exchange of particles with the bed did not have a significant effect on the flow.

In Section 4.3.6 we considered flows for which the predicted Froude number was unity and surface N-waves were produced. Small bed perturbations due to erosion excited surface N-waves which in turn resulted in the formation of bed ripples. The N-waves and bed ripples were coupled, travelled slowly upstream, and were sustained for very long times.

In Section 4.3.7 we briefly demonstrated that other bed patterns, like stepping, can be formed by manipulating various parameters. In the absence of viscous terms in the momentum equation (which are responsible for generating Roll waves as in [3]), it seems that the only mechanism present in our model to generate wave structured is the "critical Froude number" mechanism. Therefore, complex bed formations such as those seen in Section 4.3.7 can only be formed by choosing the drag and slope parameters so that the predicted Froude number is unity and subsequently manipulating the remaining parameters.

In conclusion, the coupling of flow and sediment dynamics and the inclusion of drag and bottom topography, not present in other studies and in contrast to Pritchard and Hogg [42], had significant effects on the dynamics of both the fluid and the dilute sediment. We have demonstrated that a complex interplay between the intensity of the basal drag, the bed topography, and the cohesiveness of the bed is present and ultimately determines the long term behaviour of the fluid and sediment dynamics. For flows over initially flat beds, a flow can either be dominated by deposition in which case the volume fraction of sediment eventually reaches zero as all particles settle out of suspension, or continue to erode the bed in which case the volume fraction of sediment eventually reaches a non-zero steady state after the effects of erosion and deposition reach an equilibrium. For flows over initially sloping beds, if the drag, bed cohesion, and slope parameters allow the flow to begin eroding the bed, then the flow will continue to erode the bed for all post-release times with the volume fraction of sediment growing linearly in the downstream direction and attaining its maximum directly behind the snout for all post-release times. Finally, if the Froude number of flow, which can be predicted prior to release, is close to unity then surface N-waves may be excited by small bed disturbances created by erosion. These surface N-waves interact with the bed to form ripples and other more complicated bed formations.

Bibliography

[1] A. Aliseda, A. Cartellier, F. Hainaux, and J.C. Lasheras. Effect of preferential concentration on the settling velocity of heavy particles in homogeneous isotropic turbulence. *J. Fluid Mech.*, 468:77–105, 2002.

[2] R.A. Bagnold. Auto-Suspension of Transported Sediment; Turbidity Currents. *Proc. R. Soc. London, Ser. A*, 265(1322):315–319, 1962.

[3] N.J. Balmforth and S. Mandre. Dynamics of roll waves. *J. Fluid Mech.*, 514:1–33, 2004.

[4] T.B. Benjamin. Gravity currents and related phenomena. *J. Fluid Mech.*, 31(02):209–248, 1968.

[5] F. Blanchette, M. Strauss, E. Meiburg, B. Kneller, and M.E. Glinsky. High-resolution numerical simulations of resuspending gravity currents: Conditions for self-sustainment. *J. Geophys. Res.*, 110:C12022, 2005.

[6] R.T. Bonnecaze, M.A. Hallworth, H.E. Huppert, and J.R. Lister. Axisymmetric particle-driven gravity currents. *J. Fluid Mech.*, 294:93–121, 1995.

[7] R.T. Bonnecaze, H.E. Huppert, and J.R. Lister. Particle-driven gravity currents. *J. Fluid Mech.*, 250:339–369, 1993.

[8] R.T. Bonnecaze, H.E. Huppert, and J.R. Lister. Patterns of sedimentation from polydispersed turbidity currents. *Proc. R. Soc. London, Ser. A*, 452:2247–2261, 1996.

[9] M.I. Cantero, S. Balachandar, and M.H. García. An Eulerian–Eulerian model for gravity currents driven by inertial particles. *Int. J. Multiphase Flow*, 34:484–501, 2008.

[10] H. Capart and D.L. Young. Formation of a jump by the dam-break wave over a granular bed. *J. Fluid Mech.*, 372:165–187, 1998.

[11] G.K.C. Clarke, A.B.G. Bush, and J.W.M. Bush. Freshwater discharge, sediment transport, and modeled climate impacts of the final drainage of glacial Lake Agassiz. *J. Climate*, 22(8):2161–2180, 2009.

[12] SL Cole. Transient waves produced by flow past a bump. *Wave Motion*, 7(6):579–587, 1985.

[13] W.B. Dade and H.E. Huppert. A box model for non-entraining, suspension-driven gravity surges on horizontal surfaces. *Sedimentology*, 42(3):453–470, 1995.

[14] F. De Rooij and S.B. Dalziel. Time-and space-resolved measurements of deposition under turbidity currents. *Spec. Publs. int. Ass. Sediment*, 31:207–215, 2001.

[15] R.F. Dressler. Hydraulic resistance effect upon the dam-break functions. *J. Res. Nat. Bur. Stand.*, 49:217–225, 1952.

[16] R.F. Dressler. Comparison of theories and experiments for the hydraulic dam-break wave. In *Proceedings of the Commission des Eaux de Surface at the Assemble Gnrale de Rome 1954*, volume 38, pages 319–328. International Association of Hydrological Sciences, September 1954.

[17] K.R. Dyer and R.L. Soulsby. Sand Transport on the Continental Shelf. *Ann. Rev. Fluid Mech.*, 20(1):295–324, 1988.

[18] I. Eames. Settling of particles beneath water waves. *J. of Phys. Oceanography*, 38(12):2846–2853, 2008.

[19] M. Emmett and T.B. Moodie. Dam-break flows with resistance as agents of sediment transport. *Phys. Fluids*, 20(8):086603, 2008.

[20] M. Emmett and T.B. Moodie. Sediment transport via dam-break flows over sloping erodible beds. *Stud. Appl. Math.*, 123(3):257–290, 2009.

[21] L. Fraccarollo and H. Capart. Riemann wave description of erosional dam-break flows. *J. Fluid Mech.*, 461:183–228, 2002.

[22] M.H. García and G. Parker. Entrainment of Bed Sediment Into Suspension. *J. Hydr. Eng.*, 117(4):414–435, 1991.

[23] C. Gladstone, J.C. Phillips, and R.S.J. Sparks. Experiments on bidisperse, constant volume gravity currents: Propagation and sediment deposition. *Sedimentology*, 45:833–843, 1998.

[24] R.H.J. Grimshaw and N. Smyth. Resonant flow of a stratified fluid over topography. *J. Fluid Mech.*, 169:429–464, 1986.

[25] A. Harten. Eno schemes with subcell resolution. *J. Comput. Phys.*, 83(1):148–184, 1989.

[26] A.J. Hogg and D. Pritchard. The effects of hydraulic resistance on dam-break and other shallow inertial flows. *J. Fluid Mech.*, 501:179–212, 2004.

[27] A.J. Hogg, M. Ungarish, and H.E. Huppert. Particle-driven gravity currents: asymptotic and box model solutions. *Euro. J. Mech. B Fluids*, 19(1):139–156, 2000.

[28] Xin Huang and M.H. García. A Herschel–Bulkley model for mud flow down a slope. *J. Fluid Mech.*, 374:305–333, 1998.

[29] G.S. Jiang and C.W. Shu. Efficient implementation of weighted ENO schemes. *J. Comput. Phys.*, 126(1):202–228, 1996.

[30] R. R. Kerswell. Dam break with Coulomb friction: a model for granular slumping? *Phys. Fluids*, 17(5):057101, 16, 2005.

[31] J. Kevorkian and J. Yu. Passage through the critical Froude number for shallow-water waves over a variable bottom. *J. Fluid Mech.*, 204:31–56, 1989.

[32] T. Koyama and H. Ikeda. Effect of riverbed gradient on bedrock channel configuration: a flume experiment. *Proceedings of the Environmental Research Center*, pages 25–34, 1998.

[33] S.J. Lee, G.T. Yates, and T.Y. Wu. Experiments and analyses of upstream-advancing solitary waves generated by moving disturbances. *J. Fluid Mech.*, 199:569–593, 1989.

[34] D. Martin and R. Nokes. Crystal settling in a convecting magma chamber. *Nature*, 332:534–536, 1988.

[35] T. B. Moodie. Gravity currents. *J. Comput. Appl. Math.*, 144(1-2):49–83, 2002.

[36] T.B. Moodie and J.P. Pascal. Axisymmetric particle-bearing gravity flows on sloping bottoms. *Can. Appl. Math. Q.*, 7:17–47, 1999.

[37] T.B. Moodie and J.P. Pascal. Non-hydraulic effects in particle-driven gravity currents in deep surroundings. *Stud. Appl. Math.*, 107:217–251, 2001.

[38] T.B. Moodie, J.P. Pascal, and J.C. Bowman. Modeling sediment deposition patterns arising from suddenly released fixed-volume turbulent suspensions. *Stud. Appl. Math.*, 105:333–359, 2000.

[39] T.B. Moodie, J.P. Pascal, and G.E. Swaters. Sediment transport and deposition from a two-layer fluid model of gravity currents on sloping bottoms. *Stud. Appl. Math.*, 100:215–244, 1998.

[40] F. Necker, C. Härtel, L. Kleiser, and E. Meiburg. High-resolution simulations of particle-driven gravity currents. *Int. J. Multiphase Flow*, 28(2):C12022, 2002.

[41] J.P. Pascal, T.B. Moodie, N. Antar, and S.J.D. D'Alessio. Solutions for initial-boundary-value problems representing gravity currents arising from variable inflow. *Stud. Appl. Math.*, 119:127–171, 2007.

[42] D. Pritchard and A.J. Hogg. On sediment transport under dam-break flow. *J. Fluid Mech.*, 473:265–274, 2002.

[43] D. Pritchard and AJ Hogg. Cross-shore sediment transport and the equilibrium morphology of mudflats under tidal currents. *J. Geophys. Res*, 108:3313–3328, 2003.

[44] D. Pritchard and A.J. Hogg. Suspended sediment transport under seiches in circular and elliptical basins. *Coastal Eng.*, 49(1-2):43–70, 2003.

[45] A. Ritter. Die fortpflanzung der wasserwellen. *Z. Verein. Deutsch. Ing.*, 36:947–954, 1892.

[46] J.W. Rottman and J.E. Simpson. Gravity currents produced by instantaneous releases of a heavy fluid in a rectangular channel. *J. Fluid Mech.*, 135:95–110, 1983.

[47] J.E. Simpson. *Gravity Currents in the Environment and the Laboratory.* Cambridge University Press, Cambridge England, 1997.

[48] P.K. Stansby, A. Chegini, and T.C.D. Barnes. The initial stages of dam-break flow. *J. Fluid Mech.*, 374:407–424, 1998.

[49] J.J. Stoker. *Water Waves.* Interscience, New York, 1957.

[50] C. Teisson, M. Ockenden, P. Le Hir, C. Kranenburg, and L. Hamm. Cohesive sediment transport processes. *Coastal Eng.*, 21:129–162, 1993.

[51] M. Ungarish. *Hydrodynamics of suspensions: fundamentals of centrifugal and gravity separation.* Springer Verlag, 1993.

[52] M. Ungarish. On the modeling and investigation of polydispersed rotating suspensions. *Int. J. Multiphase Flow*, 21(2):267–284, 1995.

[53] G.B. Whitham. The effects of hydraulic resistance in the dambreak problem. *Proc. R. Soc. London, Ser. A*, 227:399–407, 1955.

[54] G.B. Whitham. *Linear and Nonlinear Waves.* Wiley, New York, 1974.

Appendix A

First order correction for small drag

The following Python source was used to compute the first order correction in C_D for $0 < C_D \ll 1$ to the Ritter solution (see Section 3.1).

```
"""Integrate the inner height and velocity fields for dam-break flows
   with drag.

   The governing equations for the inner height and volicity fields
   are given by (4.20) and (4.21) of 'The effects of hydraulic
   resistance on dam-break and other shallow inertial flows',
   A.J. Hogg and D. Pritchard, JFM v501 pp179-212, 2004.

   Throughout, q[0] is the height and q[1] is the velocity.

"""

import numpy
import sympy
import sympy.solvers
import scipy.integrate
import scipy.optimize
import struct
import matplotlib.pylab as plt


# have we found the governing equations yet?
equations = True

if not equations:

    ##
    ## symbolic
    ##

    U, H, Up, Hp, eta, eta1 = sympy.var('U H Up Hp eta eta1')

    eq420 = H/2 - eta*Hp + Hp - U*Hp - Up*H
    eq421 = U/4 - eta*Up + Up - U*Up - Hp + 81/64/eta1**3/H

    # solve 4.20 for H' and substitute into 4.21
    iHp = sympy.solvers.solve(eq420, Hp)[0]

    # now, isolate U'
    iUp = sympy.solvers.solve(eq421.subs(Hp, iHp), Up)[0]

    # and subs back into iHp
    iHp = iHp.subs(Up, iUp)

    print 'DE'
    print sympy.simplify(iHp)
    print sympy.simplify(iUp)

    alpha = H + 2*(U+eta) - (U+eta)**2 - 1
    myHp = ( H*(1-eta-U/2)/2 + 1/eta1**3 ) / alpha
```

```
        myUp = ( ( 1/eta1**3 + H*U/4 ) * ( 1 - U - eta ) + H**2/2 ) / H / alpha

        print sympy.simplify(iHp - myHp)
        print sympy.simplify(iUp - myUp)

else:

    ##
    ## numeric
    ##

    # derivative
    def f(q, eta, eta1):
        H = q[0]
        U = q[1]

        alpha = H - (U+eta-1.0)**2

        Hp = ( 0.5*H*(1.0-eta-0.5*U) + 1.0/eta1**3 ) / alpha
        Up = ( (1.0/eta1**3 + 0.25*H*U) * (1.0-U-eta) + 0.5*H**2 ) / H / alpha

        return numpy.array([Hp, Up])

    # backward euler
    def backward_euler(q, q0, eta, eta1, h):
        qp = f(q, eta, eta1)

        return q - q0 - h*qp

    ## left half (from -infinity)
    def left(eta1):
        eta0 = -500.0
        q0 = [1.0/16.0*(eta0 - 1.0)**2, 1.0/2.0*(1 - eta0)]

        eta = numpy.hstack((numpy.array([eta0]), numpy.linspace(-20.0, -0.05, 1001)))

        q, info = scipy.integrate.odeint(f, q0, eta, args=(eta1,),
                                         printmessg=False, full_output=True)

        # find the last time at which odeint was successful
        last = 0
        for i, n in enumerate(info['nfe']):
            if n > 500:
                last = i
                break

        eta_stop = (info['tcur'])[last]

        return (eta_stop, eta, q)

    ## right half (from 0)
    def right(eta1):
        eta = numpy.linspace(0.0, -2.0, 20001)

        q = numpy.zeros((eta.size, 2))
        q[0,:] = numpy.array([0.0, 1.0])

        q0 = numpy.array([0.00001, 1.0])
        eta_stop = 0.0
        for n, t in enumerate(eta[1:]):

            h = eta[n+1] - eta[n]

            # first try solving backward euler
            q[n+1,:], info, flag, mesg = scipy.optimize.fsolve(backward_euler, q0,
                                                 args=(q[n,:], t, eta1, h),
                                                 warning=False, full_output=True)

            if not (flag == 1):
                eta_stop = t
                break

            q0 = q[n+1,:]

        return (eta_stop, eta, q)

    ## bi-section search to find eta1

    tol_bisect = 0.0000001
    high = -2.771101
    low  = -2.771100

    left_eta_stop = 0.0
    right_eta_stop = 0.0

    while (abs(high - low) > tol_bisect):

        eta1 = 0.5*(high + low)

        (left_eta_stop, left_eta, left_q) = left(eta1)
```

```
        (right_eta_stop, right_eta, right_q) = right(eta1)

        if (left_eta_stop > right_eta_stop):
            high = eta1
        else:
            low = eta1

print "eta1 = ", eta1

# plot!

# left side
i = (numpy.nonzero(-20.0 <= left_eta))[0]
eta_l = left_eta[i]
h_l = left_q[i,0]
u_l = left_q[i,1]

i = (numpy.nonzero(eta_l < left_eta_stop))[0]
eta_l = eta_l[i]
h_l = h_l[i]
u_l = u_l[i]

# right side
i = (numpy.nonzero(right_eta_stop < right_eta))[0]
eta_r = right_eta[i]
h_r = right_q[i,0]
u_r = right_q[i,1]

# dump
eta = numpy.hstack((eta_l, eta_r[::-1]))
h   = numpy.hstack((h_l, h_r[::-1]))
u   = numpy.hstack((u_l, u_r[::-1]))

f = open('hogg.dat', 'wb')
f.write(struct.pack("i", eta.size))
eta.tofile(f)
h.tofile(f)
u.tofile(f)
f.close()

# plot solutions
plt.plot(eta, h, '-k')
plt.plot(eta, u, '-r')

# outter solutions
eta = numpy.linspace(-2.0, 0.0, 201)
h = 1.0/16.0*(eta - 1.0) **2
u = 1.0/2.0*(1.0 - eta)

plt.plot(eta, h, '--k')
plt.plot(eta, u, '--r')

plt.show()
```

Appendix B

Forced KdV solver

The following Python source was used to compute the solution to the forced KdV
equation (see Section 4.3.1).

```
"""Solve the forced KdV equation (for F=1) in Kevorkian & Yu.
"""

import math
import numpy as np

import scipy.io as sio

dx = 0.1
x  = np.arange(-20.0, 80.0, dx)
N  = x.size

dt = dx**3
t  = np.arange(0.0, 24.0, dt)
M  = t.size

g = np.zeros((M, N))

def bed(x):
    """Bed: d/dx e^{-x^2}"""
    return -2.0*x*math.exp(-x**2)

ubed = np.frompyfunc(bed, 1, 1)
b = ubed(x)


for n in xrange(M-1):
    for i in xrange(3, N-4):
        g[n+1,i] = ( g[n,i]
                    + 3.0/4.0 * dt * g[n,i] * (g[n,i+1] - g[n+1,i-1]) / (2.0*dx)
                    + 1.0/6.0 * dt * (g[n,i+3] - 3.0*g[n,i+1] + 3.0*g[n+1,i-1] - g[n+1,i-3]) / (2.0*dx)**3
                    + dt * b[i] )

sio.savemat('kdv.mat', {'x': x, 't': t, 'g': g})
```